UNIVERSITY OF LONDON

Imperial College of Science, Technology and Medicine
Department of Physics
Blackett Laboratory
Optics Section

ULTRASHORT PULSE GENERATION WITH A DISTRIBUTED FEEDBACK DYE LASER

by

Wing Chung PANG

Thesis submitted for the degree of
Doctor of Philosophy of the University of London
and for the Diploma of Imperial College

February 1989

To my family and friends

ABSTRACT

This work describes the generation of intense ultrashort UV pulses with an excimer laser pumped distributed feedback dye laser (DFDL) system.

Emphasis is placed on the ability of the gain-coupled distributed feedback technique of producing ultrashort pulses. Experimental studies of an excimer pumped DFDL are described and a numerical analysis based on the rate equation model is used to further the understanding of the laser action, especially in gaining physical insight into the pulse-forming dynamics. Some possibilities of generating pulses of shorter duration are also discussed.

An excimer laser pumped DFDL system producing transform-limited single pulses of 100 ps duration with good transverse beam quality is described. The propagation of the DFDL output beam is compared with that of the zeroth-order Gaussian beam.

There are detailed descriptions of the construction of a master oscillator-amplifier system which is used to produce 0.5 MW, 100 ps pulses of UV radiation at 308 nm. The main points include the operation of the DFDL oscillator at 616 nm, amplification of the high quality output pulse in a two-stage dye amplifier, and frequency-doubling of the resulting 3-4 MW pulse to produce the required UV pulse. Methods of monitoring and optimising the performance of the system at each stage are discussed. The final output pulse could be used in an injection locked XeCl gain module producing very intense pulses for use in nonlinear optics experiments.

ACKNOWLEDGEMENTS

I should like to thank my supervisor, Dr. Henry Hutchinson, for his advice, support and encouragement during the course of this work. Special thanks are due to Dr. Fergus O'Neill, who collaborated on some parts of the work, for his guidance and assistance.

I gratefully acknowledge the help and advice of all the members of the Laser Group, in particular: Dr. Roy Taylor for his assistance in streak-camera measurements as well as other expert advice, Drs. Mike Damzen and Mike Osborne for many fruitful discussions, Dr. John Vukusik for his good jokes and encouragement and Mr. Dimitris Xenakis for his assistance in the laboratory towards the end of this project.

I wish to thank Mr. Roy Morrison and his colleagues John, Bob, Charlie and Ted for the technical support. I should also like to thank Dr. Ernest Tsui for the hours spent reading the manuscript and Mrs. Helen Hodgson for her accurate typing of this thesis.

I am indebted to the Science and Engineering Research Council for their financial support.

I should like to express my gratitude to my colleagues and friends Drs. Jeremy Chang, Ernest Tsui and Jian-Ying Zhou for their support and friendship throughout these years. Many other friends have also given me much encouragement. Some of them are hundreds or thousands of miles away from the U.K.; their support is gratefully acknowledged.

I wholeheartedly thank my parents and grandmother for their continual support and encouragement throughout the many years of school and university, my brother and sisters for carrying my share of the financial burden of the family over the past few years.

Finally, I wish to thank my wife Yuet Sim for her support,patience and encouragement, and for taking care of our young son Tsoek Fung round the clock so that I can get some sleep at night and get on with my thesis during the day.

CONTENTS

		Page
ABSTRACT		3
ACKNOWLEDGEMENTS		4
CONTENTS		5
LIST OF FIGURES		7
LIST OF TABLES		12
CHAPTER 1:	INTRODUCTION	13
CHAPTER 2:	COUPLED-WAVE THEORY OF DISTRIBUTED FEEDBACK LASERS	20
2.1	Introduction	20
2.2	Coupled-Wave Model	25
	2.2.1 The coupled-wave model	25
	2.2.2 Solution of the coupled-wave equations	29
2.3	Results and Discussions	32
	2.3.1 High-gain and low-gain approximations	32
	2.3.2 Stop bands and dispersion	35
	2.3.3 Mode pattern	39
2.4	Conclusion	39
CHAPTER 3:	RATE EQUATION MODEL OF DISTRIBUTED FEEDBACK DYE LASERS	42
3.1	Introduction	42
3.2	Rate Equations	43
3.3	Computer Solutions	48
3.4	Generation of Shorter DFDL Pulses	52
3.5	Comments on the Equivalent Cavity Decay Time	65
3.6	Conclusion	73
CHAPTER 4:	RATE EQUATION MODEL OF UNDERCOUPLED DISTRIBUTED DYE FEEDBACK LASERS	74
4.1	Introduction	74
4.2	The Undercoupled DFDL Model	75
4.3	Comparisons with Other Theoretical Models	82
4.4	Characteristics of DFDL Pulses	107
4.5	Conclusion	126

CHAPTER 5: EXCIMER LASER PUMPED DISTRIBUTED FEEDBACK DYE LASER 127
5.1 Introduction 127
5.2 XeCl Excimer Laser Pumped DFDL 129
5.2.1 Introduction 129
5.2.2 Pumping arrangement for the DFDL 131
5.2.3 Experimental studies of the DFDL 134
5.3 General Characteristics of the DFDL 141
5.3.1 Single-pulse operation 141
5.3.2 Optical beam quality 143
5.3.3 Temporal characteristics 147
5.3.4 Spectral properties and the time-bandwidth product 151
5.3.5 Other characteristics 155
5.3.6 Comparisons of experimental and theoretical results 159
5.4 Conclusion 163

CHAPTER 6: PICOSECOND UV PULSE GENERATION 164
6.1 Introduction 164
6.2 Amplification of DFDL Pulses 166
6.3 Generation of Ultrashort UV Pulses 174
6.3.1 The principles of second-harmonic generation 174
6.3.2 Generation of ultrashort UV pulses with ADP crystals 181
6.4 Conclusion 185

CHAPTER 7: CONCLUSION 186

REFERENCES 188

List of Figures

Figure	Title	Page
2.1a	Illustration of laser oscillation in a periodic structure.	21
2.1b	Two counter-propagating waves in a distributed feedback structure.	21
2.2	A simplified model of a DFB structure.	23
2.3	A typical example of modulation in a DFB structure.	23
2.4	X-ray diffraction.	24
2.5	The Bragg condition in a DFB structure.	24
2.6a	The mode spectrum and required threshold gain for a gain periodicity.	34
2.6b	The mode spectrum and required threshold gain for an index periodicity.	34
2.7a	Dispersion diagram for index modulation with no loss or gain.	36
2.7b	Dispersion diagram for index modulation for various gain to coupling parameter ratios.	36
2.8a	Dispersion diagram for gain modulation with no loss or gain.	38
2.8b	Dispersion diagram for gain modulation for various gain to coupling parameter ratios.	38
2.9	Spatial intensity distribution for the fundamental mode at various coupling strengths for index-coupled DFL and gain-coupled DFL.	40
2.10	Spatial intensity distribution for the first three modes of an overcoupled DFL.	40
3.1	A four-level laser model.	45
3.2	Computer solutions of the coupled rate equations.	50
3.3	Dependence of pulse duration on pumping rate.	54
3.4	Output power of a DFDL with moderate pumping rate.	54
3.5	Temporal and energy characteristics of a DFDL.	55
3.6	Output power of a DFDL with high pumping rate.	56
3.7	The formation of an ultrashort pulse in a DFDL.	58
3.8	Temporal structure of a DFDL with external feedback.	60
3.9	DFDL output with external feedback - high pumping rate.	61

Figure	Title	Page
3.10	Temporal structure of a DFDL with a constant pumping rate.	63
3.11	DFDL output with external feedback - constant pumping rate.	64
3.12	Variation of pulse-width with pulse number.	64
3.13	Steady-state spatial intensity distribution.	71
4.1a	Steady-state spatial intensity distribution (under-coupled DFDL model).	77
4.1b	Final intensity distribution for steady-state pumping (semi-classical model).	77
4.2	Coupled waves and spatial intensity distribution.	78
4.3	Computer solutions of the rate equations (under-coupled DFDL model).	80
4.4a	First-pulse duration versus pumping rate (under-coupled DFDL model).	83
4.4b	First-pulse duration versus pumping rate (over-coupled DFDL model).	83
4.5a	First-pulse energy versus pumping rate (under-coupled DFDL model).	84
4.5b	First-pulse energy versus pumping rate (over-coupled DFDL model).	84
4.6	Dependence of pulse energy on pumping rate.	85
4.7a	First-pulse duration versus pumping rate (short device length: undercoupled DFDL model).	87
4.7b	First-pulse duration versus pumping rate (short device length: overcoupled DFDL model).	87
4.8a	First-pulse energy versus pumping rate (short device length: undercoupled DFDL model).	88
4.8b	First-pulse energy versus pumping rate (short device length: overcoupled DFDL model).	88
4.9	Pulse duration versus device length.	89
4.10	Theoretical dependence of pulse duration on device length.	91
4.11	First-pulse duration versus cavity lifetime.	92
4.12a	Generation of single DFDL pulse with a short pump pulse (device length: 1 mm).	93

Figure	Title	Page
4.12b	Generation of single DFDL pulse with a short pump pulse (device length: 4 mm).	94
4.13	First-pulse duration versus pumping rate (short pump pulse).	95
4.14	First-pulse energy versus pumping rate (short pump pulse).	95
4.15	Pulse duration versus device length (short pump pulse).	97
4.16a	A computer-generated multiple-pulse profile from the undercoupled DFDL model (short pump pulse).	98
4.16b	A computer-generated temporal profile from the undercoupled DFDL model (short pump pulse).	98
4.17	First-pulse duration versus pump-pulse duration undercoupled DFDL model).	99
4.18a	First-pulse duration versus pumping rate (long pump pulse: undercoupled DFDL model).	101
4.18b	First-pulse duration versus pumping rate (long pump pulse: overcoupled DFDL model).	101
4.19a	First-pulse energy versus pumping rate (long pump pulse: undercoupled DFDL model).	102
4.19b	First-pulse energy versus pumping rate (long pump pulse: overcoupled DFDL model).	102
4.20a	Effect of upper-state lifetime on pulse duration (undercoupled DFDL model).	103
4.20b	Effect of upper-state lifetime on pulse duration over-coupled DFDL model).	103
4.21a	Effect of solvent refractive index on pulse duration (undercoupled DFDL model).	104
4.21b	Effect of solvent refractive index on pulse duration (overcoupled DFDL model).	104
4.22a	Effects of initial noise-photon number (undercoupled DFDL model).	105
4.22b	Effects of initial noise-photon number (overcoupled DFDL model).	105
4.23	The formation of an ultrashort pulse in a DFDL (overcoupled DFDL model).	108

Figure	Title	Page
4.24	The formation of an ultrashort pulse in a DFDL (undercoupled DFDL model).	108
4.25	Comparison of computed DFDL pulse and Gaussian pulse profiles.	111
4.26	Microdensitometer plot of a DFDL pulse profile obtained with a streak camera.	112
4.27	Comparison of Gaussian and DFDL pulse profiles.	112
4.28	Temporal characteristics of a DFDL.	115
4.29	Theoretical relationship between peak power and pulse duration (undercoupled DFDL model).	118
4.30	Experimental results: relationship between peak power and pulse duration.	118
4.31	Theoretical relationship between peak power and pulse duration (overcoupled DFDL model).	120
4.32	Theoretical relationship between peak power and pulse duration (data points extracted from reference [10] - overcoupled DFDL model).	120
4.33	Theoretical relationship between pulse energy and pulse duration (undercoupled DFDL model).	121
4.34	Theoretical relationship between pulse energy and pulse duration (overcoupled DFDL model).	121
4.35	Theoretical relationship between pulse duration and excess pump power (undercoupled DFDL model).	124
4.36	Theoretical relationship between pulse duration and excess pump power (overcoupled DFDL model - data points extracted from reference [10]).	125
5.1	Typical pulse shape of the Lambda Physik EMG 101 XeCl laser output.	130
5.2	Schematic diagram of distributed feedback dye laser.	132
5.3	Variation of the XeCl pulse shape with main discharge voltage.	135
5.4	XeCl pulse shape for an old gas-fill.	136
5.5	Generation of DFDL double-pulse with a double-peak pump pulse.	137
5.6	Generation of ultrashort pulses with DFDL.	140
5.7	Pulse shapes of XeCl pump beam.	142
5.8	Diode-array records of DFDL beam profiles.	145

Figure	Title	Page
5.9	Intensity profile of a focused DFDL beam at the focal spot.	146
5.10	Microdensitometer plot of a DFDL pulse profile.	148
5.11	Linear plot of a DFDL pulse profile.	148
5.12	Comparison of DFDL and Gaussian pulse profiles.	149
5.13	Comparison of DFDL and the $sech^2$ pulse profiles.	149
5.14	Typical Fabry-Perot interferometer fringe pattern of DFDL single pulses.	152
5.15	Diode-array record of interferometer fringe pattern of a DFDL single pulse.	152
5.16	Simultaneous measurement of pulse duration and spectral linewidth for a DFDL single pulse.	153
5.17	Dependence of laser wavelength on temperature.	157
5.18	Dependence of first-pulse energy on pumping rate (simulation of XeCl pumped DFDL: undercoupled DFDL model).	160
5.19	Dependence of first-pulse duration on pumping rate (simulation of XeCl pumped DFDL: undercoupled DFDL model).	160
5.20	Dependence of first-pulse energy on pumping rate (simulation of XeCl pumped DFDL: overcoupled DFDL model).	161
5.21	Dependence of first-pulse duration on pumping rate (simulation of XeCl pumped DFDL: overcoupled DFDL model).	161
6.1	Schematic diagram of the laser system for the generation of ultrashort UV pulses.	165
6.2	End view of the "Bethune" prism amplifier dye cell.	169
6.3	Transverse distribution of ASE signal intensity of Bethune amplifier.	171
6.4	Gain saturation characteristics of Bethune amplifier.	173
6.5	Dependence of second-harmonic energy on fundamental energy.	184

List of Tables

Table	Title	Page
4.1	Relationship between peak power and pulse duration.	117
5.1	Laser dyes and solvents used in the distributed feedback dye laser.	139
5.2	Simultaneous measurement of pulse duration and bandwidth.	154
5.3	Comparison of experimental and theoretical results.	162

CHAPTER 1

INTRODUCTION

A conventional laser normally consists of an active medium and two end reflectors. The essential condition of population inversion is obtained with the active medium to provide the optical gain in the system whereas a resonant cavity is formed with the two end reflectors to provide the essential optical feedback.

A distributed feedback laser (DFL) is different from a conventional laser in that no end reflector is needed. Instead, the feedback mechanism is distributed throughout and integrated with the gain medium [1]. The necessary feedback is provided by Bragg scattering from a spatially periodic perturbation of an optical parameter of the active medium. Such a parameter can be the refractive index of the gain medium [2] or the gain itself [3]. In the case of a waveguide laser, this perturbation can be on the cross-section of the waveguide structure [4]. A mixture from these types of modulation may also be used. Spectral selection occurs due to the wavelength sensitivity of the Bragg effect. The grating-like nature of the device provides a filter mechanism which restricts the oscillation to a narrow spectral range. The combination of gain, positive feedback and spectral selectivity therefore fulfils the most important requirements for the operation of a laser.

Usually, the dimension of the distributed feedback laser is of the order of centimetres or less. And since no end mirror is required, the laser is usually mechanically very stable. Tuning may also be possible by changing the average refractive index or the spatial modulation (perturbation) period of the optical parameter of the medium. All these qualities have therefore attracted a lot of interest in this type of laser. The distributed feedback (DFB) approach has wide applications in such lasers as dye lasers [3], semiconductor lasers [4] and thin film lasers [5,6].

There are several ways of creating a distributed feedback structure. In general, a gain modulation is formed by the interference of two beams which have been split from a single laser source. The beams are recombined at the active medium so that the spatial modulation of the pumping intensity leads to a corresponding

period modulation of the gain. In this case, tuning is most easily achieved by changing the refractive index of the medium or by changing the period of modulation by varying the angle of interference. Gain modulation is most conveniently applied to dye lasers. In the other types of modulation, fabrication of the DFB structure is generally required beforehand; the device is then ready for conventional pumping arrangements. Tuning is usually not easy since the modulation period and the refractive index of the medium are fixed. However, in the case of cross-section modulation, variation in the thickness in thin film lasers can be used for tuning.

A spatial modulation of the refractive index of the active medium was used in the first experimental realization of a DFB laser [2]. The periodicity was generated by exposing a thin film of dichromated gelatin to the interference pattern produced by two coherent UV beams from a helium-cadmium laser. The gelatin, developed by methods employed in holography, resulted in a spatial modulation of the refractive index with fringe spacing about 300 nm. The developed gelatin was then soaked in a solution of rhodamine 6G to make the dye penetrate into the porous gelatin layer. The resulting DFB structure was transversely pumped with the UV radiation from a nitrogen laser. At pump densities above 10 MW/cm^2, laser oscillation at a wavelength of about 630 nm was observed. The output linewidth was measured to be less than 0.05 nm.

Distributed feedback action has been obtained from a spatial modulation of the gain induced by pumping a liquid organic dye solution (rhodamine 6G in ethanol) with fringes formed by the interference of two coherent beams from a ruby laser [3]. The laser was tunable over a range of 64 nm either by varying the angle between the interfering pump beams or the refractive index of the dye solution. The laser operated at around 600 nm. Linewidths of less than 0.001 nm were measured.

If the active region of a laser is an optical waveguide, distributed feedback can be realized by periodic corrugation of the waveguide surface [4]. This is the method adopted in semiconductor DFB lasers in which the active region is a planar waveguide. Periodic cross-section modulation has also been applied to thin film lasers and solid-dye waveguide lasers. A waveguide structure consists of three main regions; they are: an active region of

refractive index η_f, a base region which is usually a substrate of refractive index η_s, and a cover of refractive index η_c. If the relation $\eta_f > \eta_c, \eta_s$ is satisfied, then the wave launched at an appropriate angle will be guided along the active region without any loss to the outside. The mechanism can be thought of as the incident ray being successively totally internal reflected at the interfaces. However, for a wave to be guided, phase consideration must be taken into account. It turns out that there is a discrete set of values of ϕ_f, the angle of incidence on an interface, at which a wave to be launched will be guided. These guided modes have different propagation constants and the refractive index of the film appears to be different for different modes. Hence the spectral output of a laser with a waveguide structure is a set of narrow lines of different frequencies. However, the separations between these frequencies are generally small. In the case of a distributed feedback structure, the modes which are amplified are those which simultaneously satisfy the Bragg condition and are allowed modes of the waveguide structure.

One of the earliest experiments involving thin film DFB lasers has been conducted with a polyurethane thin film [5]. The film, doped with rhodamine 6G, was deposited on an isotropic substrate. The superstrate (i.e. the cover material) was taken to be air. Modulation of the refractive index was induced by optically pumping the thin film with fringes formed by the interference of two coherent beams from the second-harmonic radiation of a single-mode giantpulse ruby laser. It has been found that there are multimode structures in the output of the DFL if the waveguide is thick and single-guided mode operation can be achieved with thinner films.

Because of their various optical properties, semiconductors have been found to be very useful as the principal material in integrated optics. The first optically pumped GaAs semiconductor surface DFB laser [4] was obtained by periodically corrugating the air-GaAs interface with a corrugation period of 0.35 μm and groove depth of approximately 50 nm. Optical pumping was provided by a Q-switched ruby laser (λ = 0.6943 μm).

The wavelength of a distributed feedback laser is related to the period of modulation on the device and is approximately given by the formula

$$\lambda_0 = 2\eta\Lambda, \qquad (1.1)$$

where λ_0 is the wavelength of oscillation, Λ is the period of modulation and η is the refractive index of the active medium. This condition is known as first-order Bragg scattering and λ_0 is the first-order Bragg wavelength. There is a major problem in producing oscillation in the visible region with semiconductor distributed feedback lasers. The refractive index of GaAs is 3.6. Therefore, to generate a wavelength of, say, 0.83 μm, a perturbation period of 0.117 μm is required. The lack of convenient ultraviolet (UV) pump source in the early days made it very difficult to produce high visibility modulation of this magnitude.

The alternative was to use higher order Bragg scattering. In this case, the oscillator wavelength is given by

$$m\lambda_0 = 2\eta\Lambda \qquad (1.2)$$

where m is a positive integer. The coupling, however, is usually very weak. Nevertheless, oscillation in the third order (m = 3) has been obtained. In fact, third-order Bragg scattering was used to produce the radiation at 0.83 μm in the example above [4]. The threshold pump power density was 200 kW/cm^2 at 77 K.

A similar experiment has been carried out in the study of a heterostructure formed by epitaxial growth [7]. In this case, the optical losses were due to the presence of a confining GaAlAs solid solution layer; the threshold pump power density decreased by more than one order of magnitude to around 10 kW/cm^2. Subsequent electrically pumped DFB semiconductor lasers are also very successful.

Modulation of the gain is utilized in colour centre DFB lasers. In one of these experiments [8], a spatially modulated distribution of F_A(II) centres was used to produce the distributed feedback structure. The F_A(II) centres were produced from U centres by using the room temperature two-photon coloration process. In order to generate the laser intensity required for the two-photon process, a specially designed interferometric technique was used to write the gratings. The technique permits the piecewise generation of precisely registered gratings of arbitrary size by sequential exposure of small segments of the photosensitive medium. A higher power density can therefore be afforded and hence a shorter exposure

time required to produce a certain concentration of $F_A(II)$ centres. The DFB samples were longitudinally or transversely pumped with 532 nm light, in the form of pulses of 10 ns duration at 77 K. The output spectra were in excellent agreement with the theoretical predicted values and the linewidth in each case found to be narrower than 0.2 nm.

Distributed feedback action in gas is most easily achieved in hollow-core waveguides. In DFB dye lasers and in DFB solid state lasers the emission linewidth is relatively large. Therefore, no problem arises in looking for coincidence between the period of modulation and the emission wavelength. On the other hand, in electrically excited and optically pumped gas lasers the emission linewidth is narrow at low pressure. For this reason matching between emission and periodic structure is critical. In the first distributed feedback gas laser [9], which was a brass waveguide resonator containing CH_3F gas, the problem of matching was overcome by temperature variation between - 30°C and 95°C. The hollow rectangular waveguide had a length of 320 mm and a width of 40 mm. The bottom of the waveguide exhibited rectangular periodic corrugation with a depth of 124 μm and a period of 248 μm corresponding to a quarter and half of the wavelength of the CH_3F emission (496 μm). In order to optimize feedback, the height of the waveguide could be varied between 0 mm and 20 mm. The maximum signal output was produced at about 50°C when it was longitudinally pumped by the 9.55 μm CO_2 laser.

The distributed feedback approach has been demonstrated to be applicable to a wide variety of lasers. In particular, these lasers were found to produce radiation of narrow linewidth. It was discovered recently that the gain-coupled distributed feedback dye laser (DFDL) emitted ultrashort pulses of picosecond durations under certain conditions [10]. Within a specific range of pump power, single pulses could be generated without the need of a pulse selector. The pulse shortening mechanism is generally referred to as 'self Q-switching', which is basically a resonator-transient effect similar to relaxation oscillation. Experimental results of the output characteristics indicated that DFDL pulses were close to be transform-limited. Without the need of sophisticated electronic and optical components, distributed feedback dye lasers provide a very convenient and inexpensive means of picosecond pulse generation. The

main theme of this thesis is the generation of ultrashort pulses with gain-coupled distributed feedback dye lasers.

In Chapter 2, the coupled-wave theory of distributed feedback lasers will be derived. Some important basic characteristics of the DFB structure will be discussed. The remaining chapters will be devoted to the gain-coupled distributed dye laser. In Chapter 3, we shall outline the theoretical model used to simulate the intensity output of the DFDL. This model is based on the photon rate equations which describe the interaction between the population inversion and the number of photons inside the laser cavity. Computer solutions will be presented. The key parameter of this rate equation model is the equivalent cavity decay time, first used by Bor [10]. It is a measure of the average time a typical photon spends inside the laser cavity. We shall be discussing the validity of the use of this particular parameter. In Bor's model, the cavity decay time varies quadratically with the population inversion. Through this dependence, the dumping rate of the cavity photons is accelerated in the vicinity of pulse formation, leading to the so-called self Q-switching effect. In Chapter 4, we shall examine the process of pulse formation with a simplified rate equation model. In particular, we shall attempt to estimate the contribution of the self Q-switching effect towards the pulse-shortening process. With this new approximate rate equation model, we shall derive some simple relationships between some important parameters. These analytic expressions will be compared with the full computational results. They will be shown to be fairly good approximations. Moreover, these expressions are also found to be applicable to Bor's original model. Some experimental results will also be used to compare with these relationships. Physical insights into the pulse-forming mechanism will be found from these comparisons.

Experimental studies of an excimer laser pumped distributed feedback dye laser will be described in Chapter 5. The generation of single pulses of duration of about 100 ps will be described. The spectral and temporal characteristics of the laser will be discussed. The optical beam quality as well as other characteristics will also be examined. Most of these studies are concerned with single-pulse operations. Some comparisons between the output characteristics of the DFDL and the theoretical computer predictions will be presented. In Chapter 6, we shall describe an oscillator-amplifier system used

to amplify the single-laser pulses generated from the distributed feedback dye laser to produce intense coherent pulses with power up to 4 MW. Frequency doubling of the visible pulses was utilized to generate 0.5 MW ultrashort UV pulses.

CHAPTER 2

COUPLED-WAVE THEORY OF DISTRIBUTED FEEDBACK LASERS

2.1 Introduction

The fundamental characteristics of a distributed feedback laser (DFL) is that, in the absence of external cavity mirrors, the necessary feedback is provided by Bragg scattering from spatially periodic perturbations of the optical parameters of the active medium. These perturbations can be either the refractive index or the gain of the laser medium. They correspond to the real and imaginary components of the complex refractive index of the medium respectively. The feedback mechanism produced by these perturbations therefore has the same physical origin and can be described within a single theoretical model.

Figure 2.1a shows the operation of a distributed feedback laser in simplified terms. The arrows represent two waves, one travelling to the left and one to the right. As each wave travels in the periodic structure, it receives light at each point along its path by Bragg scattering from the oppositely travelling wave. This creates a feedback mechanism which is distributed throughout the length of the periodic structure. Since the medium also has gain, it can be seen that with sufficient feedback, there will be a condition for oscillation. These two counter-propagating waves (Figure 2.1b) are said to be coupled by backward Bragg scattering. Using this coupled-wave model, Kogelnik and Shank [1] developed a theory of distributed feedback lasers. The analysis to be described below is a linear gain theory and steady-state solutions at threshold can be obtained. In particular, it is found that for a distributed feedback (DFB) structure with some given parameters, there is a discrete set of modes; each mode has its resonant frequency, its characteristic threshold gain and its characteristic field pattern.

Before considering the rigorous mathematical theory of DFB lasers, a brief qualitative consideration of the fundamental physics would be helpful in understanding the origin of the distributed feedback mechanism. It is well known that light waves are subject to reflection in traversing from one medium to another if the

Figure 2.1a. Illustration of laser oscillation in a periodic structure.

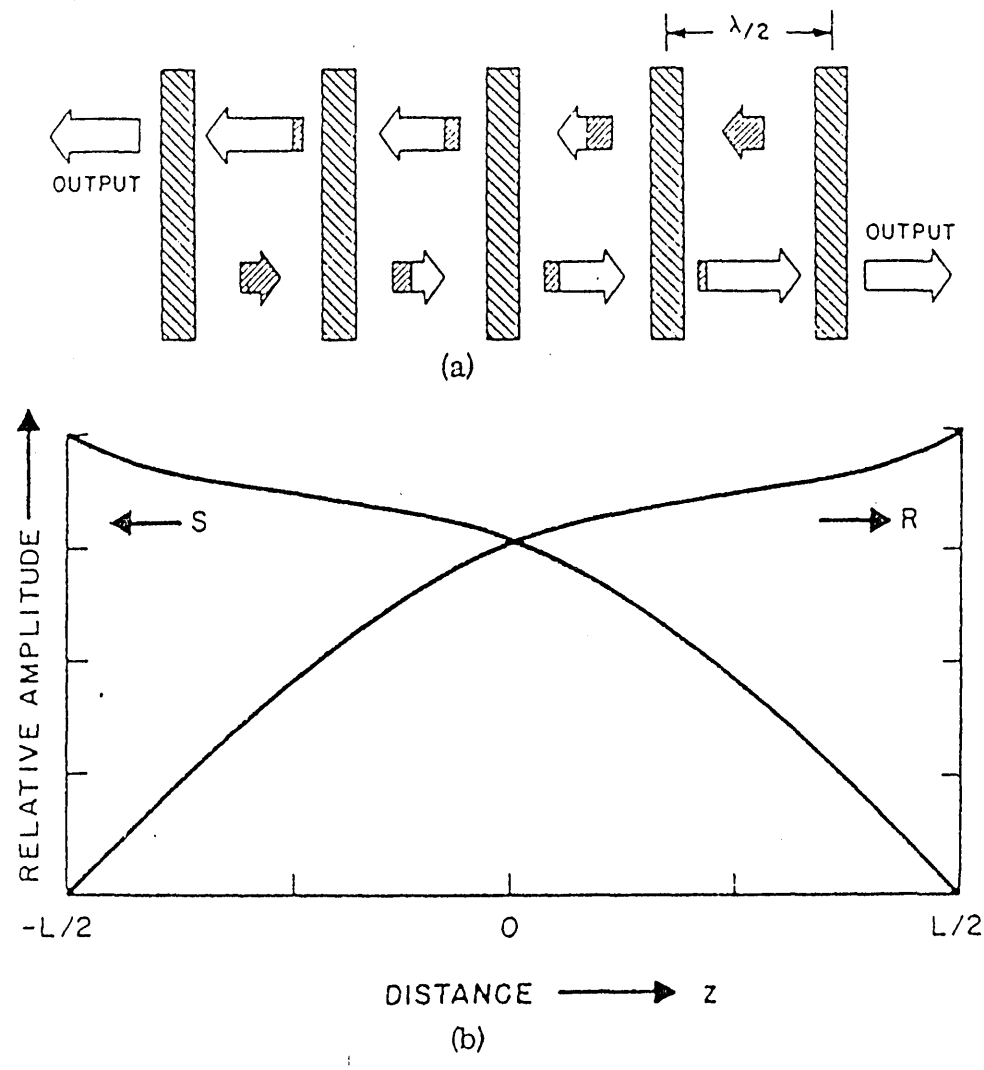


Figure 2.1b. Two counter-propagating waves in a distributed feedback structure.

refractive indices of the media are different. A distributed feedback structure may be represented, in its simplest form, as a stack of thin films having alternating refractive indices as shown in Figure 2.2. Any wave traversing this structure will therefore be subject to reflection every time it crosses a boundary. Similarly, the periodic perturbation of the complex refractive index (Figure 2.3) causes the travelling waves in the DFB structure to experience periodic reflections and part of a forward-going wave will turn into a backward-going wave and vice versa in a continuous and smooth fashion. These periodic perturbations will hence produce similar effects as a stack of partial reflectors. Instead of the two highly reflective end mirrors in a conventional laser device, a DFB structure consists of thousands of these low reflectivity "mirrors" distributed along the whole length of the structure to provide the essential feedback for laser oscillation. The spectral selectivity of the DFB structure may be simply explained in terms of Bragg diffraction which is well known in the field of X-ray diffraction by crystals. As shown in Figure 2.4, constructive interference occurs when the Bragg condition is satisfied, i.e.

$$2\Lambda \cos \theta = m\lambda; \qquad m = 1,2,3... \tag{2.1}$$

where λ is the wavelength of the X-ray, θ is the angle of incidence as shown in the figure, Λ is the spacing between the crystal planes and m is a positive integer. In the special case of $\theta = 0$ and $m = 1$, a forward-going wave will be scattered directly backward if the wavelength λ equals 2Λ. This is basically the situation for a DFB structure operating on first-order scattering (i.e. $m = 1$). Taking the medium index into account, the Bragg condition in a DFB structure is given by

$$\lambda_0 = 2\eta_0\Lambda \tag{2.2}$$

where η_0 is the refractive index of the medium, λ_0 is the oscillation wavelength in free space and Λ is now the period of modulation (see Figure 2.5).

The above consideration, though giving physical insights into the basic feedback mechanism, is not adequate in providing quantitative results relating to the general DFB structure. In

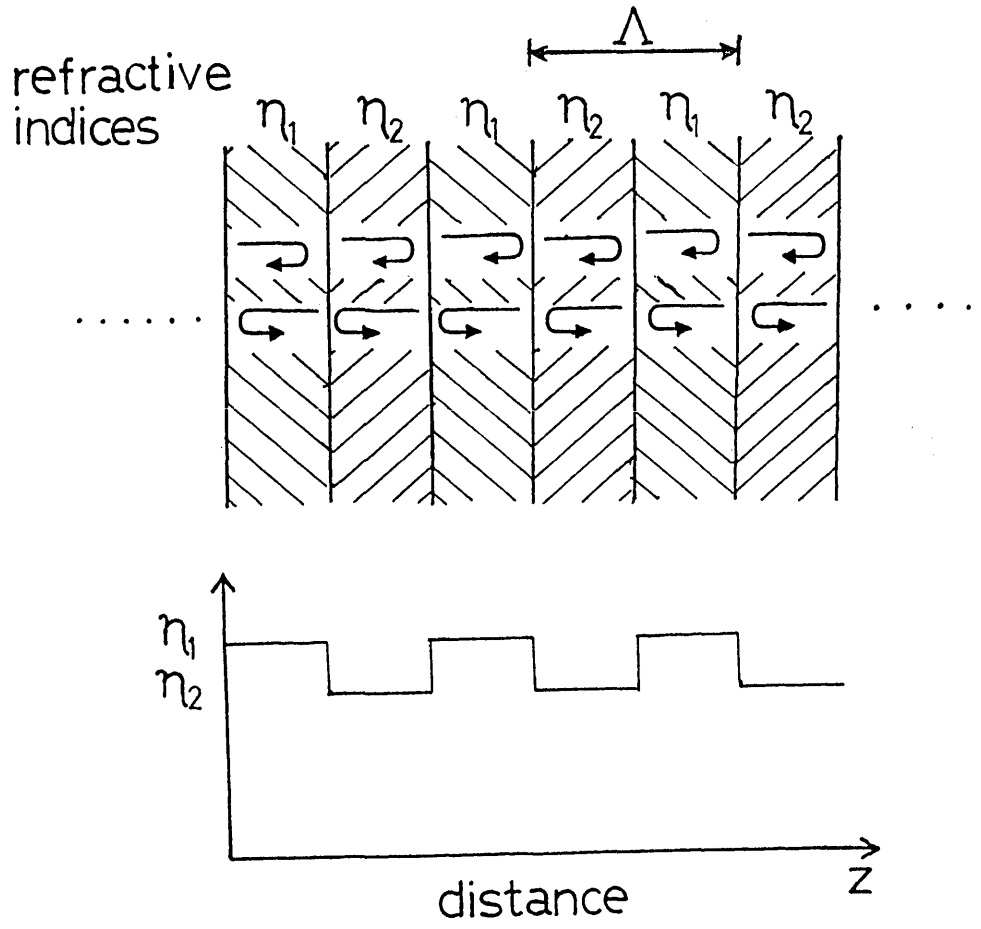


Figure 2.2. A simplified model of a DFB structure.

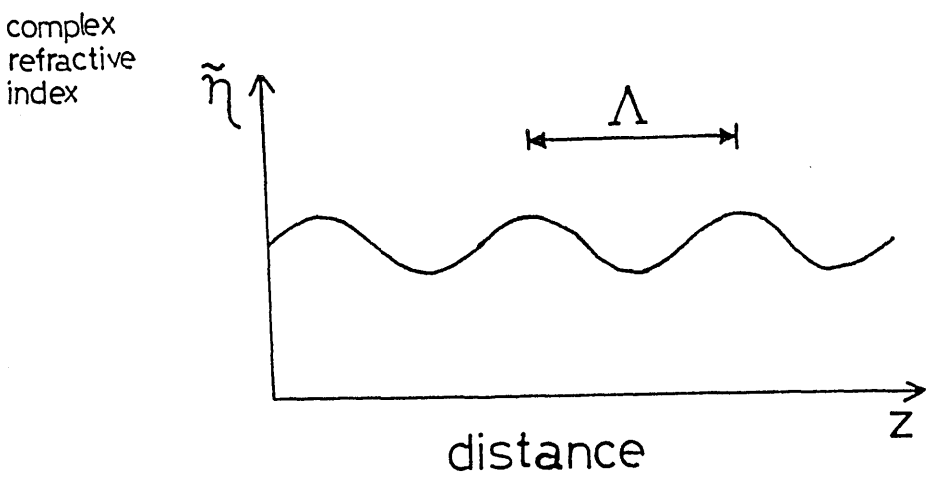


Figure 2.3. A typical example of modulation in a DFB structure.

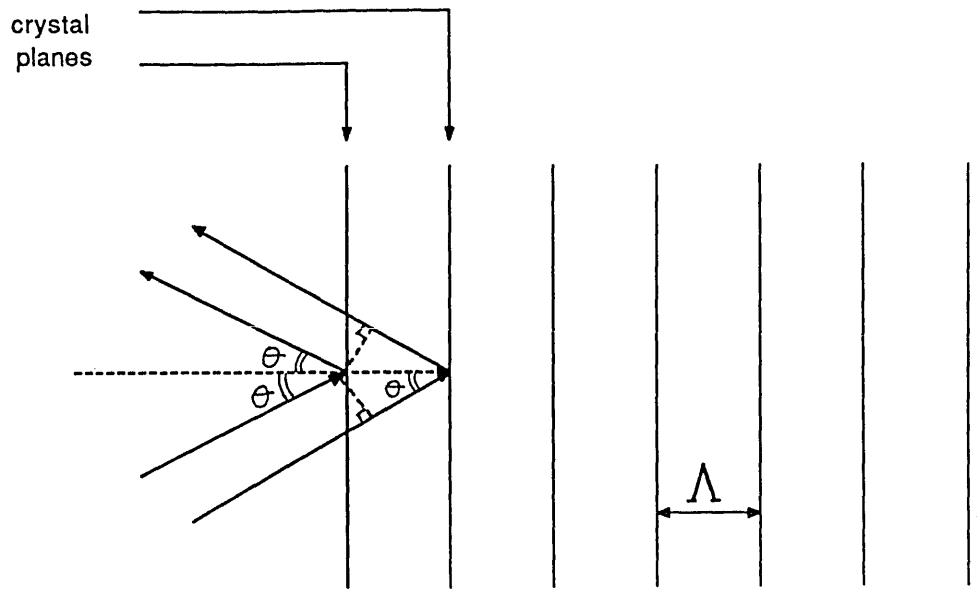


Figure 2.4 X-ray diffraction

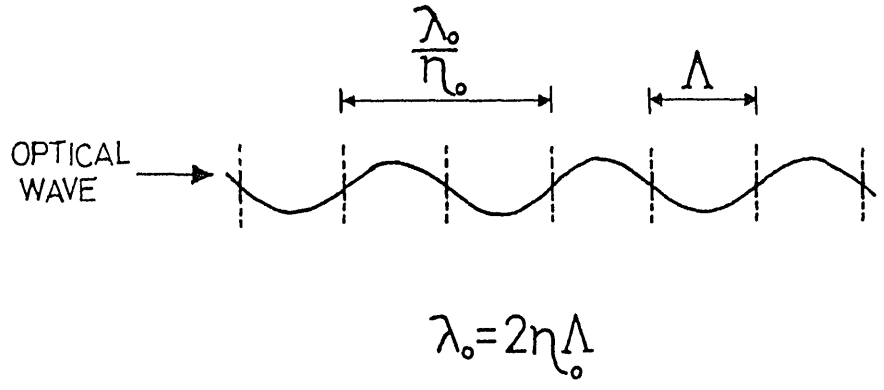


Figure 2.5. The Bragg condition in a DFB structure.

particular, the discussion so far has not taken into account any spatial phase variation of the electric field as a result of the waves traversing the inhomogeneous medium. This important spatially varying phase factor has important implications for the allowed oscillation frequencies that the DFB structure can support. A full analysis starting from the basic electromagnetic theory is required to bring out the important characteristics of distributed feedback lasers.

2.2 Coupled-Wave Model

2.2.1 The coupled-wave equations

The electromagnetic wave equation for the electric field in a linear, homogeneous and isotropic medium can be derived from Maxwell's equations and written as

$$\nabla^2 \underline{E} - \mu\varepsilon \frac{\partial^2 \underline{E}}{\partial t^2} - \mu\sigma \frac{\partial \underline{E}}{\partial t} = \underline{\nabla} \left(\frac{\rho}{\varepsilon} \right), \qquad (2.3)$$

where $\underline{E}$ ($= \underline{E}(x,y,z,t)$) is the complex electric field vector, ε is the electric permittivity of the medium, μ is the magnetic permeability of the medium, ρ is the free charge density and σ is the conductivity.

This equation is simplified when the following assumptions for the DFB medium are made:

i) the medium is uncharged ($\rho = 0$);
ii) the electric field is independent of the x and y coordinates (plane wave approximation);
iii) the electric field amplitude is time-independent (steady-state analysis);
iv) the scalar form of the electric field is considered.

The electric field may then be written as

$$E(z,t) = E(z) \exp(i\omega t), \qquad (2.4)$$

where ω is the angular frequency of the wave. Substitution into equation (2.3) leads to

$$\frac{\partial^2 E}{\partial z^2} + \omega^2 \mu\varepsilon E - i\omega\mu\sigma E = 0, \qquad (2.5)$$

where E is now the complex amplitude of the electric field of angular frequency ω. The angular frequency variation $\exp(i\omega t)$ can now be dropped and $E = E(z)$. This equation may then be written as

$$\frac{\partial^2 E}{\partial z^2} + k^2 E = 0, \qquad (2.6)$$

where

$$k^2 = \omega^2 \mu\varepsilon - i\omega\mu\sigma. \qquad (2.7)$$

From the electromagnetic theory, the absorption coefficient α_a is related to the conductivity by

$$\alpha_a = \frac{\mu c \sigma}{2\sqrt{\varepsilon_r}}, \qquad (2.8)$$

where ε_r is the relative permittivity or the dielectric constant of the medium and c is the speed of light in vacuum. Since the gain is just the negative of absorption, the gain coefficient, α, can be expressed as

$$\alpha = \frac{-\mu c \sigma}{2\eta}, \qquad (2.9)$$

where η is the refractive index of the medium (since $\eta = \sqrt{\varepsilon_r}$). If we further note that $\mu = \mu_0$, $\varepsilon = \varepsilon_0\varepsilon_r$ and $\mu_0\varepsilon_0 = 1/c^2$, where μ_0 and ε_0 are the permeability and the permittivity of free space, respectively, equation (2.7) can then be re-written as

$$k^2 = \frac{\omega^2}{c^2}\eta^2 + i\alpha\frac{\omega\eta}{c}. \qquad (2.10)$$

This 'k constant' equation can now be modified to account for the inhomogeneous nature of the DFB structure and k^2 is allowed to vary spatially according to

$$k^2(z) = \frac{\omega^2}{c^2}\eta^2(z) + i\alpha(z)\frac{\omega}{c}\eta(z), \qquad (2.11)$$

where $\eta(z)$ and $\alpha(z)$ are the spatial periodic varying refractive index and gain respectively. The coupled-wave theory, originally developed by Kogelnik and Shank [1], is based on this 'k constant' equation and the scalar wave equation for the electric field (equation (2.6)).

If the optical properties of the laser medium are independent of the x and y coordinates, but vary periodically as a function of z which points in the direction of wave propagation (see Figure 2.3), then we are essentially considering a one-dimensional model and the plane wave approximation made earlier is justified.

We assume a spatial modulation of the refractive index, $\eta(z)$, and the gain constant, $\alpha(z)$, of the form

$$\begin{aligned} \eta(z) &= \eta_0 + \eta_1 \cos 2\beta_0 z, \\ \alpha(z) &= \alpha_0 + \alpha_1 \cos 2\beta_0 z, \end{aligned} \tag{2.12}$$

where η_0 and α_0 are the average values of the refractive index and the gain of the medium, respectively, and η_1 and α_1 are the corresponding amplitudes of spatial modulation. The Bragg condition (2.2) can then be written as

$$\beta_0 = \frac{\eta_0 \omega_0}{c}, \tag{2.13}$$

where $\beta_0 = \pi/\Lambda$ and $\omega_0/c = 2\pi/\lambda_0$ and ω_0 is the Bragg frequency. Also, another parameter β can be defined as

$$\beta = \frac{\eta_0 \omega}{c}. \tag{2.14}$$

We then make the following assumptions.

i) that the DFB laser oscillates at or near the Bragg frequency ω_0,

ii) that the gain is small over distances of the order of a wavelength, i.e. $\alpha\lambda << 2\pi\eta$,

iii) that the perturbation of the refractive index and gain are small;

hence

$$\begin{aligned} \omega &\simeq \omega_0 \\ \alpha_0 &<< \beta_0 \\ \eta_1 &<< \eta_0 \\ \alpha_1 &<< \alpha_0 \end{aligned} \tag{2.15}$$

Substituting equation (2.12) into (2.11) gives

$$k^2(z) = \frac{\omega^2}{c^2} (\eta_0 + \eta_1 \cos 2\beta_0 z)^2$$

$$+ 2i \frac{\omega}{c} (\alpha_0 + \alpha_1 \cos 2\beta_0 z)(\eta_0 + \eta_1 \cos 2\beta_0 z). \tag{2.16}$$

Applying the assumptions in (2.15) allows us to write the k constant of the wave equation (2.6) in the form

$$k^2 = \beta^2 + 2i\alpha_0\beta + 4\kappa\beta \cos 2\beta_0 z, \tag{2.17}$$

where

$$\kappa = \left[\frac{\pi\eta_1}{\lambda_0} + \frac{1}{2} i\alpha_1 \right]. \tag{2.18}$$

The first two terms on the right-hand side of (2.17) describe the usual behaviour of a plane wave in a homogeneous medium. The last term, which contains the periodic characteristic, is responsible for the Bragg scattering in a distributed feedback structure. The coupling constant κ in equations (2.17) and (2.18) is a central parameter of this model. It measures the strength of the backward Bragg scattering and thus the amount of feedback provided by the structure.

In principle, a periodic perturbation of the medium generates an infinite set of diffraction orders (see equation (2.1)). But in the vicinity of the Bragg frequency, only two orders are in phase synchronism and of significant amplitude. As shown in Figure 2.1, the two significant waves in the DFB structure are the two counter-propagating waves R and S. These waves grow because of the presence of gain and they feed energy into each other due to Bragg scattering.

The waves can therefore be described by complex amplitudes R(z) and S(z) and the electric field can be written as the sum

$$E(z) = R(z)\exp(-i\beta_0 z) + S(z)\exp(i\beta_0 z). \qquad (2.19)$$

Since the gain over distances of the order of a wavelength is assumed to be small, we can treat R(z) and S(z) as slowly varying so that their second derivatives $\frac{\partial^2 R}{\partial z^2}$ and $\frac{\partial^2 S}{\partial z^2}$ can be neglected. Equations (2.17) and (2.19) may then be inserted into the wave equation (2.6). By comparing terms with equal exponentials, we can obtain a pair of coupled-wave equations of the form

$$\begin{aligned} -R' + (\alpha_0 - i\delta)R &= i\kappa S, \\ S' + (\alpha_0 - i\delta)S &= i\kappa R, \end{aligned} \qquad (2.20)$$

where δ is a normalized frequency parameter defined by

$$\delta = \frac{(\beta^2 - \beta_0^2)}{2\beta} \simeq \beta - \beta_0 = \frac{\eta_0(\omega - \omega_0)}{c}, \qquad (2.21)$$

and $'$ represents the differentiation with respect to z. The parameter δ is a measure for the departure of the oscillation frequency ω from the Bragg frequency ω_0 and the Bragg condition may then be expressed as $\delta = 0$.

It can be seen from the coupled-wave equations (2.20) that the growth of the R wave is dependent on the S wave, and vice versa, via the constant κ. In fact the two waves are coupled together by this coupling constant, κ, the magnitude of which depends on the depth of modulation of the optical parameters.

2.2.2 Solution of the coupled-wave equations

To solve the coupled-wave equations, some boundary conditions are required. Since the model is that of a self-oscillating device, there are no incoming waves, and the internal waves start with zero amplitudes at the ends of the device, receiving their initial energy by scattering from the counter-propagating wave (Figure 2.1). If the structure is of length L, extending from $z = -L/2$ to $z = L/2$, then the boundary conditions for the wave amplitudes are

$$R(-L/2) = S(L/2) = 0. \tag{2.22}$$

Also, because of the assumed symmetry of the device, the electric field must either be symmetric or antisymmetric, i.e.

$$E(-z) = E(z) \text{ or } E(-z) = -E(z). \tag{2.23}$$

The general solution of the coupled-wave equations, which are first-order coupled differential equations, may be written as

$$\begin{aligned} R &= r_1 \exp(\gamma z) + r_2 \exp(-\gamma z), \\ S &= s_1 \exp(\gamma z) + s_2 \exp(-\gamma z), \end{aligned} \tag{2.24}$$

where γ is a complex propagation constant. The boundary condition (2.22) implies that the coefficients r_i and s_i are related by

$$r_1/r_2 = s_2/s_1 = -\exp(\gamma L). \tag{2.25}$$

Hence, R and S are given by

$$\begin{aligned} R &= 2r_1 \exp(-\gamma L/2) \sinh \gamma(z + L/2), \\ S &= 2s_2 \exp(-\gamma L/2) \sinh \gamma(z - L/2). \end{aligned} \tag{2.26}$$

The symmetry conditions (2.23) lead to a further set of relations between the coefficients r_i and s_i:

$$\begin{aligned} r_1 &= \pm s_2, \\ r_2 &= \pm s_1. \end{aligned} \tag{2.27}$$

Hence, the field distribution may be written in the compact form

$$\begin{aligned} R &= \sinh \gamma(z + L/2), \\ S &= \pm \sinh \gamma(z - L/2). \end{aligned} \tag{2.28}$$

These solutions of the coupled-wave equations can therefore be used

to describe the longitudinal field distribution of the modes of a DFB structure.

To determine the allowed values of γ, the solutions of equations (2.28) must be inserted back into the coupled-wave equations (2.20). Taking the sum and the difference of the two resulting equations will eventually lead to

$$\begin{aligned} -\gamma \sinh(\gamma L/2) + (\alpha_0 - i\delta)\cosh(\gamma L/2) &= \pm i\kappa \cosh(\gamma L/2) \\ -\gamma \cosh(\gamma L/2) + (\alpha_0 - i\delta)\sinh(\gamma L/2) &= \mp i\kappa \sinh(\gamma L/2). \end{aligned} \tag{2.29}$$

Combining these expressions gives

$$\begin{aligned} \gamma + (\alpha_0 - i\delta) &= \pm i\kappa \exp(\gamma L) \\ \gamma - (\alpha_0 - i\delta) &= \mp i\kappa \exp(-\gamma L). \end{aligned} \tag{2.30}$$

Some mathematical operations on these expressions give several important results. Multiplication gives the dispersion relation

$$\gamma^2 = \kappa^2 + (\alpha_0 - i\delta)^2. \tag{2.31}$$

Adding the two equations yields the complex eigenvalue equations

$$\kappa = \pm i\gamma/\sinh \gamma L. \tag{2.32}$$

Another important equation can be obtained by taking the difference of the equations:

$$\alpha_0 - i\delta = \pm i\kappa \cosh \gamma L. \tag{2.33}$$

By combining equations (2.32) and (2.33), we get

$$\alpha_0 - i\delta = \gamma \coth \gamma L. \tag{2.34}$$

Now, for a DFB structure with a given coupling parameter κ and device length L, the eigenvalue equation (2.32) will give a discrete set of modes characterized by the eigenvalue γ. And for each value of γ, there is a corresponding resonant frequency δ and a threshold gain constant α. These values can be obtained from equations (2.33) or (2.34).

2.3 Results and Discussions

2.3.1 High gain and low-gain approximations

Some important characteristics of the DFB structure are revealed by considering the high-gain approximations.

If $\alpha_0 >> \kappa$, then equation (2.31) can be approximated by

$$\gamma \simeq \alpha_0 - i\delta. \tag{2.35}$$

Inserting this into the first of the expressions in equation (2.30), we get

$$2(\alpha_0 - i\delta) \simeq \pm i\kappa \exp(\alpha_0 - i\delta)L. \tag{2.36}$$

This equation can then be multiplied by its complex conjugate equation to yield

$$4(\alpha_0^2 + \delta^2) = \kappa\kappa^* \exp(2\alpha_0 L). \tag{2.37}$$

This equation gives an idea about the spectral selectivity of the DFB structure. For a frequency deviation from the Bragg frequency of $\delta = \alpha_0$, the power coupling $\kappa\kappa^*$ has to be doubled to keep the threshold gain the same. Also, in the vicinity of the Bragg frequency ($\delta \simeq 0$), equation (2.37) can be written as

$$4\alpha_0^2 \exp(-2\alpha_0 L) \simeq (\pi\eta_1/\lambda)^2 + \alpha_1^2/4. \tag{2.37a}$$

In particular, in the case of pure gain modulation, the threshold condition then becomes

$$\alpha_1/\alpha_0 = 4 \exp(-\alpha_0 L). \tag{2.37b}$$

Hence, for a device with a given length and a gain constant, there is a minimum depth of modulation (α_1/α_0) required to attain oscillation. Another interesting point of view is that for a given medium with gain parameter α_0, more DFB "mirrors" (i.e. larger L) must be used if the "reflectivity" of these mirrors is low (i.e. low α_1/α_0) and vice versa. A similar argument can be applied in the case of pure index

modulation.

In the vicinity of the Bragg condition (i.e. $\delta << \alpha_0$), equation (2.36) is approximately

$$2\alpha_0 \exp(i\delta L) \simeq \pm i\kappa \exp(\alpha_0 L). \tag{2.38}$$

A comparison of the phases in this equation reveals the typical resonance condition for a DFB device. The phase on the left-hand side is simply δL; on the right-hand side, it is given by the sum of $\pm \pi/2$ and the phase of κ. Hence the resonance condition is given by

$$\delta L = (q + 1/2)\pi + \text{phase}(\kappa), \tag{2.39}$$

where q is an integer. Using equation (2.21) and noting that $\omega = 2\pi\nu$, this can be rewritten as

$$\nu - \nu_0 \simeq \left[\frac{c}{2\eta_0 L}\right]\left[q + \frac{1}{2} + \left(\frac{1}{\pi}\right)\text{phase}(\kappa)\right]. \tag{2.40}$$

The resonances are therefore spaced approximately $c/2\eta_0 L$ apart, which is the same as in the usual two-mirror laser cavity of length L. For gain coupling (phase(κ) = $\pi/2$) there is a resonance at exactly the Bragg frequency ν_0 (Figure 2.6a). However, for index coupling (κ real and phase(κ) = 0) there is no resonance at the Bragg frequency (Figure 2.6b). This somewhat unexpected result is difficult to explain without a rigorous theory.

In the low-gain limit, α_0 is very much less than κ (i.e. $\alpha_0 << \kappa$). For gain coupling near $\alpha_0 \simeq 0$, there is a resonance at exactly the Bragg frequency, the same result as found in the high-gain limit. The threshold condition is of the form [1]

$$\alpha_1 \simeq \pi/L. \tag{2.41}$$

For index coupling the first resonances are near

$$\delta \simeq \kappa. \tag{2.42}$$

The threshold condition is in the form of

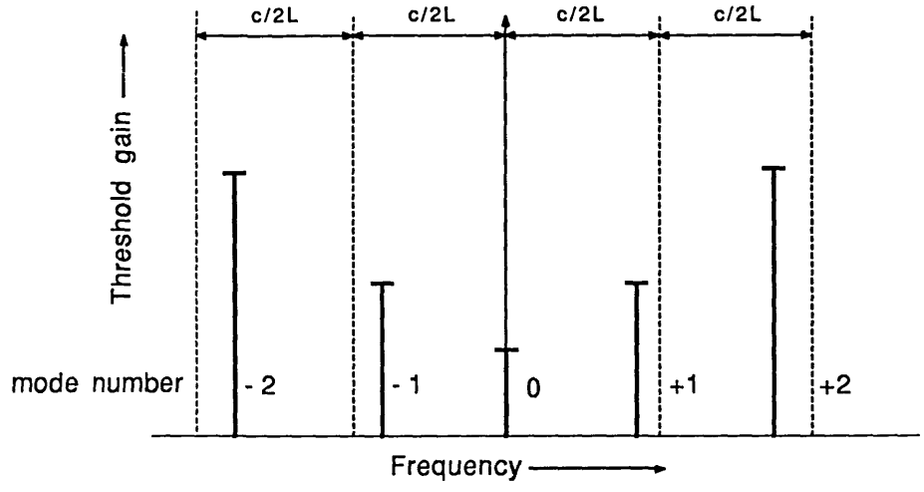


Fig. 2.6a The mode spectrum and required threshold gain for a gain periodicity

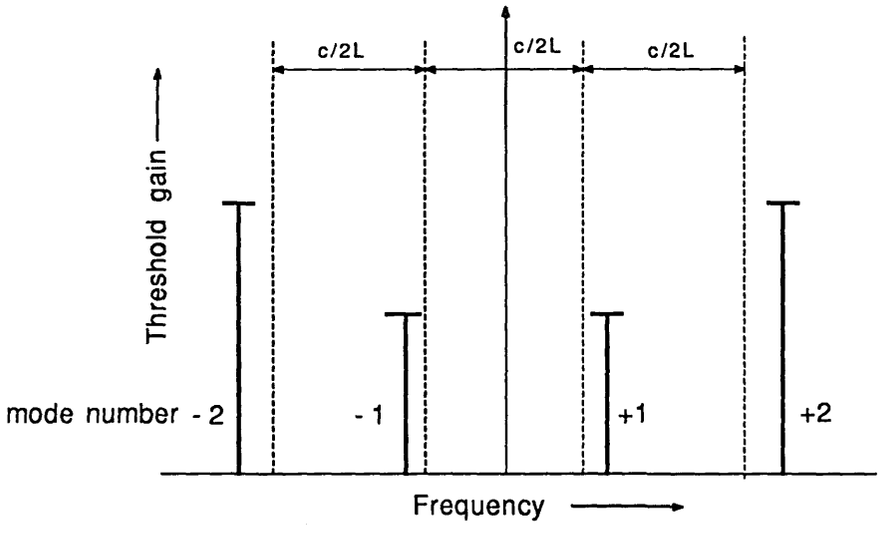


Fig. 2.6b The mode spectrum and required threshold gain for an index periodicity

$$\alpha_0 L \simeq \left[\frac{\lambda}{\eta_1 L} \right]^2. \qquad (2.43)$$

That is, the threshold gain is inversely proportional to the length of the DFB device. These results are found to be good approximations in the appropriate regions according to the numerical calculations by Kogelnik and Shank [1].

2.3.2 Stop bands and dispersion

It is well known that periodic structures are dispersive and that they have stop bands of frequencies in which propagation is forbidden. This has a profound influence on the resonance spectrum of the DFB structure. In earlier sections, we have learnt that four waves exist in the DFB structure and that they propagate as $\exp[\pm(i\beta_0 \pm \gamma)z]$. The complex propagation constant γ is determined by the dispersion relation (2.31).

Let us consider the case of pure index modulation (i.e. κ is real) in a gain-free structure (i.e. $\alpha_0 = 0$). Equation (2.31) becomes

$$\gamma^2 = \kappa^2 - \delta^2. \qquad (2.44)$$

Hence γ is imaginary if $\delta^2 > \kappa^2$ and real if $\delta^2 < \kappa^2$. And the dispersion curve can be obtained by plotting

$$\delta^2 - (\mathrm{im}(\gamma))^2 = \kappa^2, \qquad (2.45)$$

or

$$\left[\frac{\delta}{\kappa} \right]^2 - \left[\frac{\mathrm{im}(\gamma)}{\kappa} \right]^2 = 1, \qquad (2.46)$$

where $\mathrm{im}(\gamma)$ is the imaginary part of γ; it contributes to the total propagation factor in the exponent $i[\beta_0 \pm \mathrm{im}(\gamma)]z$. In Figure 2.7a, where the propagation constants are plotted as a function of ω/c, there is a stop band centred at the Bragg frequency. Inside this band (with the width equal to 2κ) γ is real, indicating evanescent waves. Outside the stop band, the dispersion curve is a hyperbola which approaches asymptotically the line where the propagation constant = ω/c and the reflection of that line through the Bragg

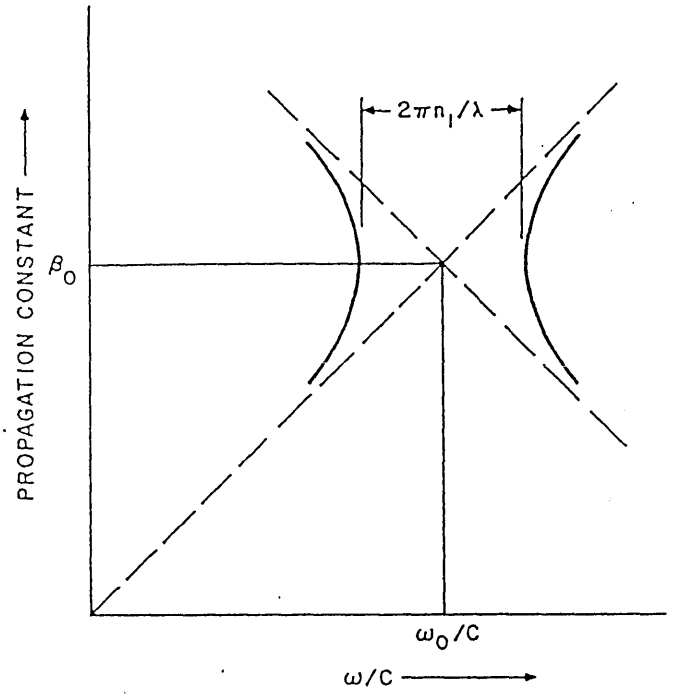


Figure 2.7a. Dispersion diagram for index modulation with no loss or gain.

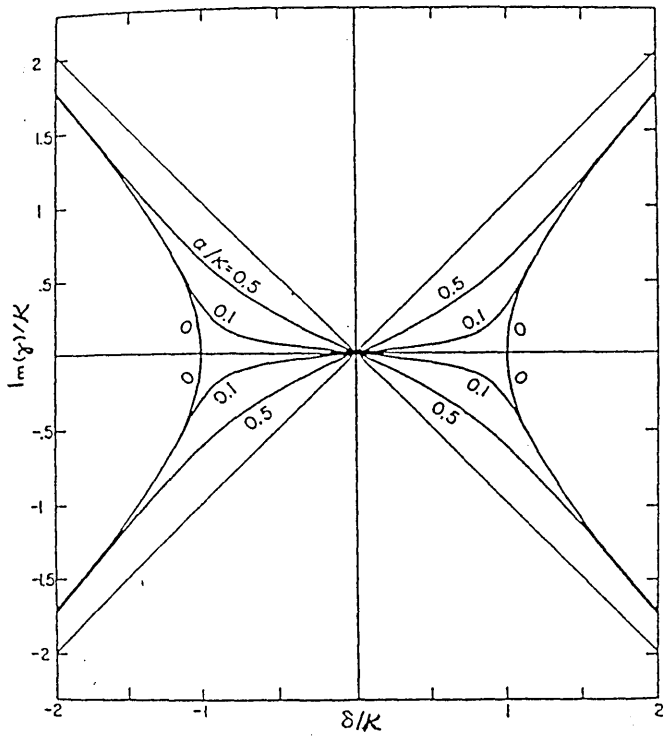


Figure 2.7b. Dispersion diagram for index modulation for various gain to coupling parameter ratios.

frequency. When gain is introduced into the structure ($\alpha_0 > 0$), the dispersion curves are found to change gradually from the H pattern of the gain-free structure to the X pattern of the asymptote as shown in the normalized plot (Figure 2.7b) obtained by using equation (2.46).

Similar dispersion curves can be obtained for the case of pure gain-coupled DFB structure. In a zero average gain ($\alpha_0 = 0$) device, the dispersion curve is also hyperbolic with the same asymptotes as in the case of index coupling except that the curves are rotated through 90° as shown in Figure 2.8a. There is no stop band in frequency. There is, however, a forbidden band of propagation constants, which is of width α_1, again centred at the Bragg condition. Again as α_0 increases, the curves change shape gradually as shown in Figure 2.8b.

As mentioned before, the mode spectra and the required threshold gains can be calculated using equations (2.32) and (2.34). Figures 2.6a and 2.6b are representations of a typical mode spectra for pure gain and pure index modulations, respectively. The dashed lines indicate the basic $c/2\eta_0 L$ frequency spacing which occurs in the high-gain limit. The mode spectra are symmetric with respect to the Bragg frequency ν_0. Of particular interest is the index coupling case in which there is no resonance at ν_0. It has been shown [1] that with increasing coupling κ, the stop band will increase and eventually becomes comparable to $c/2\eta_0 L$ and starts pushing the resonances away from ν_0. A small amount of pushing is shown in Figure 2.6b in which the threshold gain of the modes is also indicated. Note that there are always two modes having the lowest threshold gain value.

A typical mode spectrum for the case of pure gain coupling is illustrated in Figure 2.6a. There is always a resonance exactly at the Bragg condition and there is no frequency stop band. But the dispersion of the period structure produces shifts in the resonances so that the modes spacing is never quite equal to $c/2\eta_0 L$, though the mode with the lowest threshold gain is always at the Bragg frequency. The fact that the threshold increases with the frequency spacing from ν_0 provides the spectral selectivity of the DFB structure.

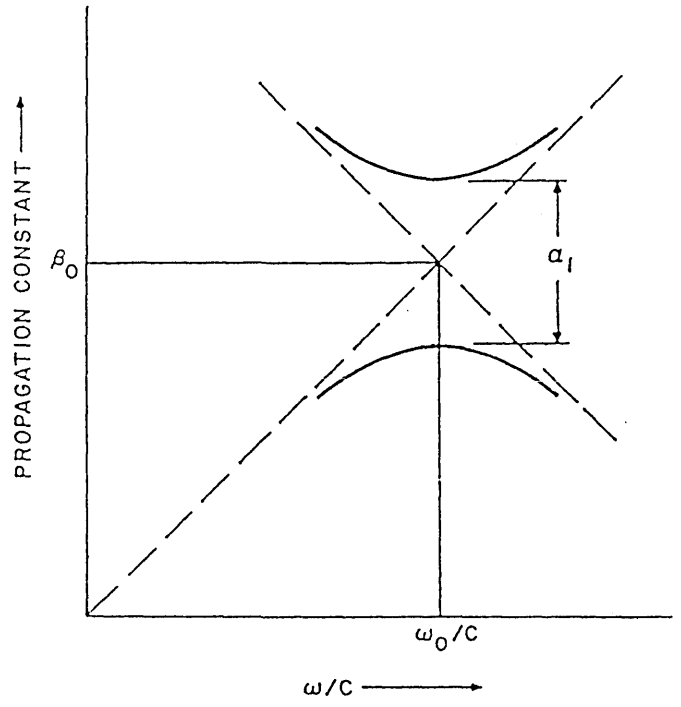


Figure 2.8a. Dispersion diagram for gain modulation with no loss or gain.

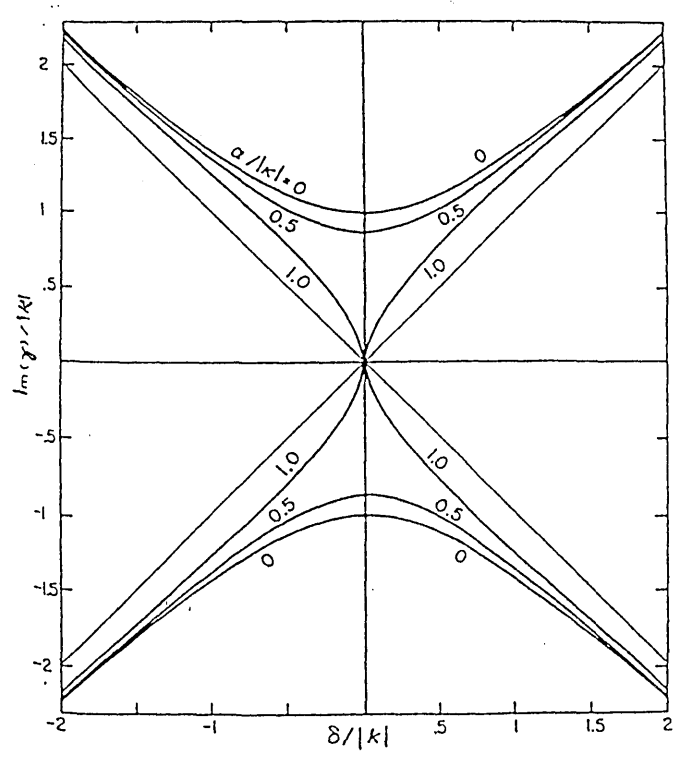


Figure 2.8b. Dispersion diagram for gain modulation for various gain to coupling parameter ratios.

2.3.3 Mode pattern

Equation (2.28), which describes the relative amplitude distribution R(z) and S(z) of the two coupled waves in a DFB structure, can be used to determine the relative intensity distributions $RR^* + SS^*$ for different eigenvalues γ. An intensity distribution represents the intensity envelope (or "mode pattern") of the modal standing-wave pattern.

Of particular interest is the mode pattern for the fundamental mode, that is the mode at or, in the case of index coupling, closest to the Bragg condition. There are basically three different types of patterns which depend on the strength of coupling κ (Figure 2.9). When the coupling is small ($\kappa L << 1$), the intensity pattern hangs through in the middle region of the device and peaks at the ends ("undercoupling"). Conversely, when the coupling is large ($\kappa L >> 1$), then the mode intensity peaks in the centre of the device and decays towards the ends ("overcoupling"). These two limiting types of behaviour are linked by a region of "critical coupling", where $\kappa L \approx 1$ and where the intensity is more or less uniformly distributed throughout the device.

The higher-order modes seem to behave similarly but with one characteristic distinction. In the overcoupled case, these high orders have more than one peak (e.g. Figure 2.10). In particular, the number of peaks depends on the corresponding mode number N.

2.4 Conclusion

This chapter started with an introductory section on the most basic concept of a DFB structure and an attempt was made to explain in simple terms why such structures can support laser oscillation.

We then described a rigorous theory in order to bring out the general characteristics of these devices. The derivation of the coupled-wave theory was outlined and some important features of the DFB structure have been discussed. These include the discrete nature of its resonance modes, the corresponding threshold conditions and the longitudinal mode patterns. We have also discussed the influences of the dispersion in the periodic structure on its resonance frequencies. In particular, the stop bands of

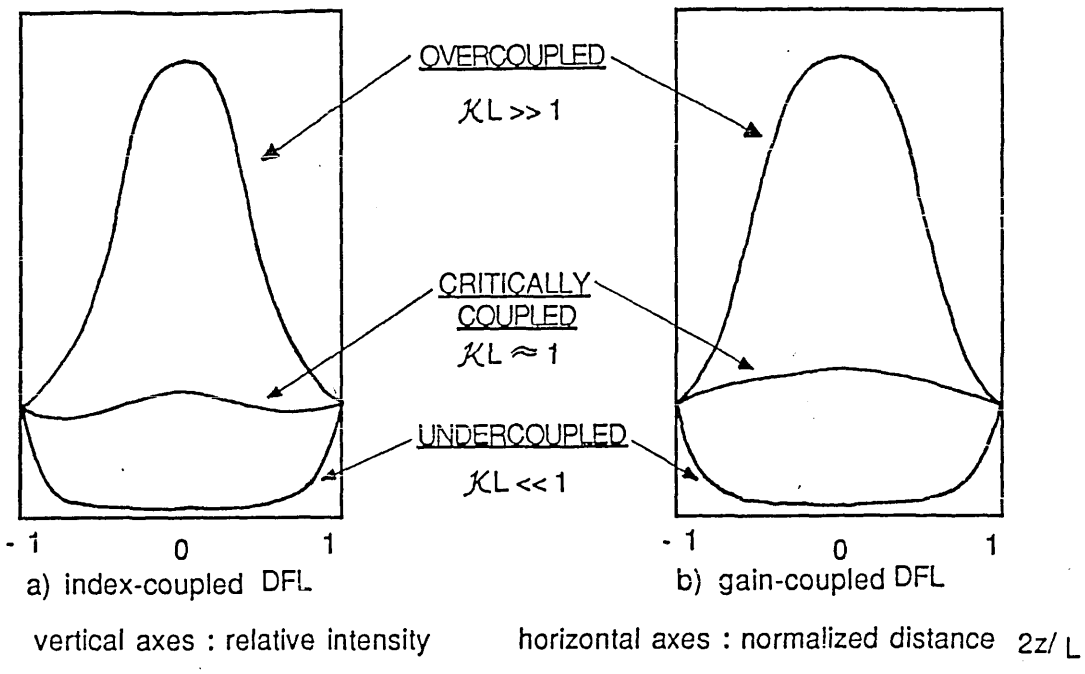


Figure 2.9. Spatial intensity distribution for the fundamental mode at various coupling strengths for a) index-coupled and b) gain-coupled DFL.

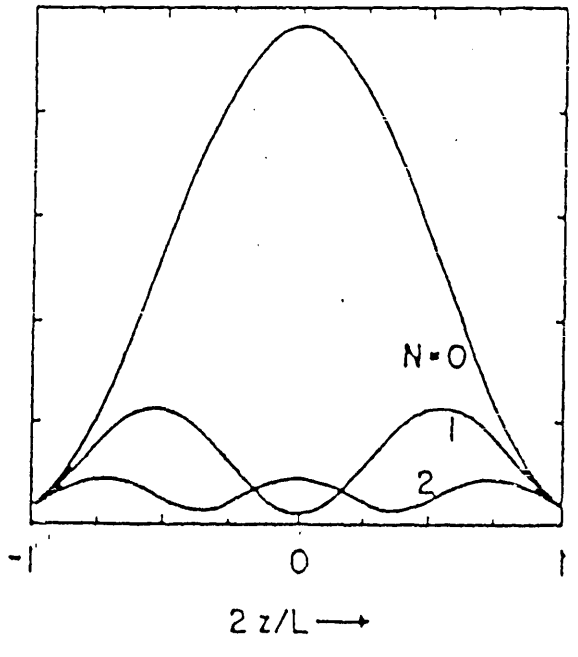


Figure 2.10. Spatial intensity distribution for the first three modes of an overcoupled DFL.

index-coupled structures do not allow oscillations at the Bragg frequency.

In the following chapters, we shall be concentrating on one particular type of distributed feedback lasers, namely, the gain-coupled distributed feedback dye lasers.

CHAPTER 3

RATE EQUATION MODEL OF DISTRIBUTED FEEDBACK DYE LASERS

3.1 Introduction

The coupled-wave theory developed by Kogelnik and Shank [1] successfully describes some fundamental characteristics of distributed feedback lasers. In particular, the experimentally observed spectral properties of the light sources generated by DFB lasers were well explained by the theory in terms of the mode structures and the threshold-gain characteristics.

For the rest of this thesis, we shall be focussing our attention on one particular type of DFB lasers - the gain-coupled distributed feedback dye laser (DFDL). Similar to other types of distributed feedback lasers, the DFDLs have been known to have good spectral properties for a long time [3]. They are particularly interesting because the active medium, dye, has been well known to be quite special; dye lasers are easily tunable over a wide range of frequency from the ultraviolet to the near-infrared. Gain-coupling for the dye laser can be easily arranged by pumping the active medium with two interfering laser beams. In this case, tuning is accomplished by varying the angle of interference so that the period of gain modulation is changed and the wavelength of oscillation is accordingly altered.

The gain-coupled DFDLs have received much interest recently due to their temporal characteristics. It was discovered that under certain conditions, the DFDLs emitted ultrashort pulses of picosecond duration. In fact, there are several advantages in using the DFDLs to generate ultrashort pulses. First of all, unlike a mode-locked dye laser, which generates a train of closely separated pulses, a DFDL can generate single ultrashort pulses directly; hence no pulse selector is required. Secondly, the nitrogen-pumped or excimer-pumped DFDL systems are inexpensive, compact and reliable since they do not contain any sophisticated optical or electronic components. The pulse repetition rate is continuously variable and is determined by the repetition rate of the pumping laser. The distributed feedback technique is applicable to any dye operating at any

wavelength since no saturable absorbers are needed. Tunability without mode-hopping is also straightforward. The time-bandwidth product of a single pulse is close to the transform-limited values of Gaussian-like profiles. Also, it is easy to construct an oscillator-amplifier system, since only a small fraction of the pumping laser power is needed to pump the DFDL.

In later chapters, we shall describe some experimental studies on the gain-coupled DFDLs. Before then, we shall be concentrating on the theoretical background of these lasers. In the next section, we shall outline a theoretical model based on a couple of rate equations which describe the interaction between the population inversion and the number of photons inside the laser cavity. A computer program has been developed at Imperial College during the course of this work to simulate the laser action. Some typical solutions to the rate equations will be presented in section 3.3. The general features will also be briefly described. In section 3.4 we shall examine two specific ways of generating shorter pulses. We shall consider the power output of the DFDL under high pumping power conditions. The possibility of further pulse shortening with external feedback will also be explored. In section 3.5 we shall go through the derivation of the key parameter of this rate equation model — the equivalent cavity decay time. The assumptions made on the derivation will also be closely examined.

3.2 Rate Equations

The generation of ultrashort pulses by a gain-coupled distributed feedback dye laser (DFDL) was first experimentally demonstrated by Bor [10]. The gain modulation was produced temporarily by pumping the active medium with two interfering beams from a nitrogen laser. It was found that, in general, a train of short pulses was emitted when the DFDL was pumped well above threshold. Within a certain range of pumping power, however, the laser was found to emit single pulses of duration shorter than 100 picoseconds. A theoretical model based on the photon rate equations was used by Bor [10,11] to explain these observations. Experimental results show good qualitative agreement with the computer solutions. The following describes this rate equation model.

This model treats the dye laser as a four-level system. The

laser is assumed to be oscillating in a single mode. Only the ground singlet state S_0, the first excited singlet state S_1, and the second excited single state S_2 of the dye molecules are considered to be involved in the lasing process. Triplet-state effects are neglected. It is assumed that the emission and the absorption bands of the dye molecules in solutions are homogeneously broadened and that the decay of the metastable upper level (S_1 state) is purely radiative. In the case of the S_2 singlet level being the upper absorption level, the S_2-S_1 nonradiative relaxation time is assumed to be much shorter than the lifetime of the S_1 state in the presence of stimulated emission. However, the bleaching of the ground state, spontaneous emission and excited state absorption at the lasing wavelength are taken into account.

Figure 3.1 shows the idealized four-level laser system. The nonradiative relaxation rates of 3 → 2 and 1 → 0 are assumed to be large enough so that all the molecules can be treated as to be either in level 2 or level 0 at all times. The behaviour of the DFDL can then be described by the following coupled rate equations [11]:

$$\frac{dn}{dt} = I_p \sigma_p (N - n) - \frac{\sigma_e c}{\eta} nq - \frac{n}{\tau} , \qquad (3.1)$$

$$\frac{dq}{dt} = \frac{(\sigma_e - \sigma_a)c}{\eta} nq - \frac{q}{\tau_c} + \Omega \frac{n}{\tau} . \qquad (3.2)$$

The meanings of the symbols are as follows:

- n: spatially averaged density of molecules in the first excited singlet state S_1,
- q: density of DFDL photons,
- N: density of dye molecules,
- I_p: spatially averaged pump photon flux per unit area,
- σ_p: absorption cross-section from S_0 to higher lying singlet states at the pumping wavelength λ_p,
- σ_a: excited state absorption cross-section from S_1 to S_2 at the lasing wavelength λ_1,
- σ_e: stimulated emission cross-section from S_1 to S_0 at the lasing wavelength,
- τ: fluorescence lifetime,
- τ_c: equivalent cavity decay time,

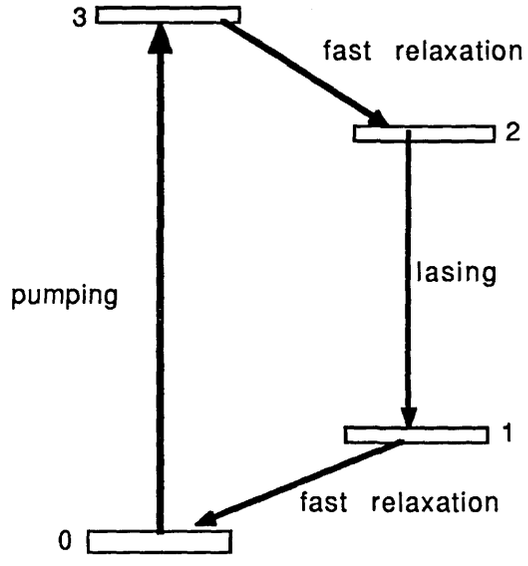


Figure 3.1 A four-level laser model

c: the speed of light,

η: refractive index of the dye solution,

Ω: the fraction of spontaneous emission contributing to the laser output.

Note that n, q and I_p are time-dependent parameters and that they represent the spatially averaged values over the entire length of the laser device.

Equations (3.1) and (3.2) are nonlinear equations describing the rate of change of the population inversion density, n, and the rate of change of cavity photon density, q, respectively. The equations are coupled in the sense that solutions can be found only if both equations are solved simultaneously.

The first term in equations (3.1) is the pumping rate for the laser inversion. It originates from the absorption of the pump photons by the ground state molecules and their subsequent fast relaxation into the metastable S_1 state. The second term describes the depletion of population inversion by stimulated emission. Spontaneous decay of the excited molecules in S_1 gives rise to the third term.

The number of cavity photons can be increased by the stimulated emission process but decreased when excited state absorption occurs. The combined effect is put together to give the first term of equation (3.2). The second term accounts for the output coupling loss with τ_c being the average photon lifetime in the cavity. The third term simulates the effect of spontaneous emission on the temporal behaviour of the laser.

The parameter Ω accounts for the fraction of the spontaneous emission which propagates into the angular and spectral range of the DFDL beam and is calculated as

$$\Omega = \frac{b}{\pi N \sigma_p L^2 S} , \qquad (3.3)$$

where L is the length of the DFDL, $(N\sigma_p)^{-1}$ is the penetration depth of the pumping beam into the dye solution, b is the height of the excited volume and S is the spectral factor determining the fraction of the spontaneous emission which falls into the DFDL bandwidth. The exact value of Ω was found to have insignificant effects on the

computer solutions [11].

The parameter τ_c is the equivalent cavity decay time. It is defined as the ratio of the total photon number in the laser cavity to the rate of loss of photons. It therefore measures the statistical average time spent by a photon inside the laser cavity. For a conventional cavity formed by two end mirrors with reflectivities R_1 and R_2 and no other losses, the cavity decay time (photon lifetime) τ_c is given by [12]

$$\tau_c = \frac{\eta L}{c\left[1 - \sqrt{R_1 R_2}\right]}, \tag{3.4}$$

where $\eta L/c$ is the cavity transit time.

The equivalent cavity decay time for a first-order overcoupled distributed feedback laser was obtained by Chinn [13] and is given by

$$\tau_c = \frac{\eta L}{2c}\left[\frac{|\kappa| L}{\pi}\right]^2, \tag{3.5}$$

where κ is the coupling constant. This expression was calculated primarily for the index-coupled distributed feedback laser. Nevertheless, Bor [10] used the corresponding expression for the gain-coupled DFDL in his rate equation model. Assuming that the effect of any refractive index modulation on the feedback is negligible, the equivalent cavity decay time can then be written as

$$\tau_c = \frac{\eta L^3}{8c\pi^2}\alpha_1^2. \tag{3.6}$$

The amplitude of the gain modulation α_1 is related to the population inversion density n by

$$\alpha_1 = (\sigma_e - \sigma_a)Vn, \tag{3.7}$$

where V is the visibility of the pumping interference fringes. Therefore the expression for the cavity decay time is

$$\tau_c = \frac{\eta L^3}{8c\pi^2}[n(\sigma_e - \sigma_a)V]^2. \tag{3.8}$$

Note that τ_c is not a constant as in the case of the conventional

cavity with two end reflectors (3.4). It is proportional to the square of the inversion density n. During the emission of a pulse, the inversion density drops rapidly and therefore the cavity decay time will in fact fall even more rapidly. This will lead to an additional contribution to the overall pulse shortening effect.

The output power from one end of the DFDL is calculated as

$$P = \frac{1}{2} \frac{hc}{\lambda_0} \frac{qLab}{\tau_c} , \tag{3.9}$$

where h is Planck's constant and

$$a = \frac{1}{N\sigma_p} \tag{3.10}$$

is the penetration depth of the pump beam into the dye solution. The steady-state (threshold) value of the population inversion can be calculated by considering the operation of a cw laser. In this case, the change of the number of cavity photons will be zero and the contributions by spontaneous emission will be negligible. Using equations (3.2) and (3.8) with these assumptions, an expression for the threshold inversion, n_0, can be obtained:

$$n_0 = \frac{2}{(\sigma_e - \sigma_a)L} \left[\frac{\pi}{V} \right]^{2/3} . \tag{3.11}$$

3.3 Computer Solutions

The coupled rate equations with the auxiliary equations described in the previous section were used by Bor [11] to simulate the temporal evolution of the output power of distributed feedback dye lasers. A fourth-order Runge-Kutta numerical scheme was used to solve the equations on a computer using parameters corresponding to their experimental conditions. Numerical instabilities occurring at the beginning of the computations ($t = t_0$) were suppressed by using the following approximate stationary solutions for n(t) and q(t) as the initial values:

$$n(t_0) = I_p(t_0)\sigma_p N\tau, \tag{3.13}$$

$$q(t_0) = \frac{\frac{\Omega n(t_0)}{\tau}}{\frac{8c\pi^2}{\eta L^3}\left[\frac{1}{n(t_0)(\sigma_e-\sigma_a)V}\right]^2 - \frac{(\sigma_e-\sigma_a)c}{\eta}\, n(t_0)} \qquad (3.14)$$

where t_0 is the starting time of the calculations. The pumping pulse represented by $I_p(t)$ was assumed to be a Gaussian and the value of t_0 was chosen such that $I_p(t_0)$ was at least 1000 times less than the peak of $I_p(t)$. Some detailed computer solutions have been presented in two of Bor's publications [10,11]. In general, good qualitative agreement between the computer solutions and the experimental observations was obtained. The rate equation model therefore offers a good qualitative description of the temporal behaviour of the distributed feedback dye laser.

During the course of this work at Imperial College, a computer program based on the rate equation model described above was developed to study the temporal characteristics of the distributed feedback dye laser output pulses.

The mainframe CDC Cyber 855 computer at Imperial College Computer Centre was used and the program was written in FORTRAN. The coupled-rate equations were solved with a numerical scheme based on the fourth-order Runge-Kutta method. Due to the very rapid changes of the parameter q upon pulse formation, a small integration step-width was required to retain accuracy and avoid instability. This, however, does imply that the computing time will be extremely long. This problem was solved by employing an integration step-width control routine to regulate the step-width so that substantial computer time can be saved without losing accuracy. Using this computer program, the results obtained by Bor [11] were repeated and confirmed.

Some typical results obtained by us are shown in Figure 3.2. Parameters for the organic dye rhodamine 6G were used in this set of calculations: $\sigma_p = 2.4 \times 10^{-17}$ cm^2, $\sigma_e = 1.4 \times 10^{-16}$ cm^2, $\sigma_a = 0.7 \times 10^{-16}$ cm^2, $\tau = 4$ ns, $\lambda_0 = 590$ nm, $\lambda_p = 337$ nm, $\eta = 1.44$, $V = 1$, $S = 10^4$, $N = 2.1 \times 10^{18}$ cm^{-3} (i.e. 3.5×10^{-3} M), $\ell = 6$ mm, $b = 0.25$ mm. Pulse duration (full width at half maximum (FWHM)) of the

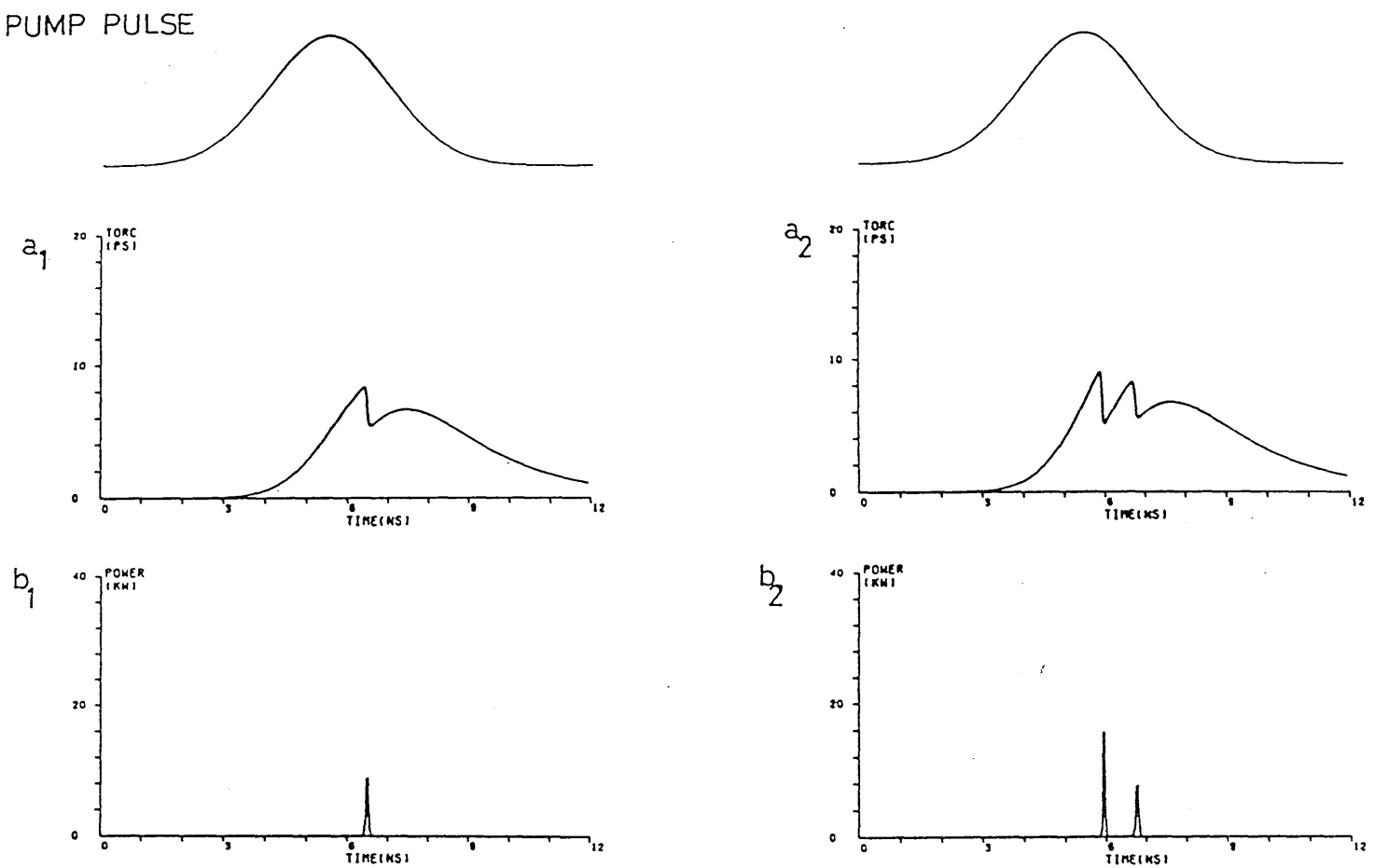


Figure 3.2. (Part 1) Computer solutions of the coupled rate equations.

a_1-a_4: equivalent cavity decay time, b_1-b_4: output power of the DFDL.

The relative pumping rates are 1.25, 1.5, 2.0 and 2.5 respectively.

Normalized unit pumping rate ($I_p \sigma_p N$) is 5.05×10^{25} $cm^{-3}s^{-1}$, corresponding to 4.83 kW.

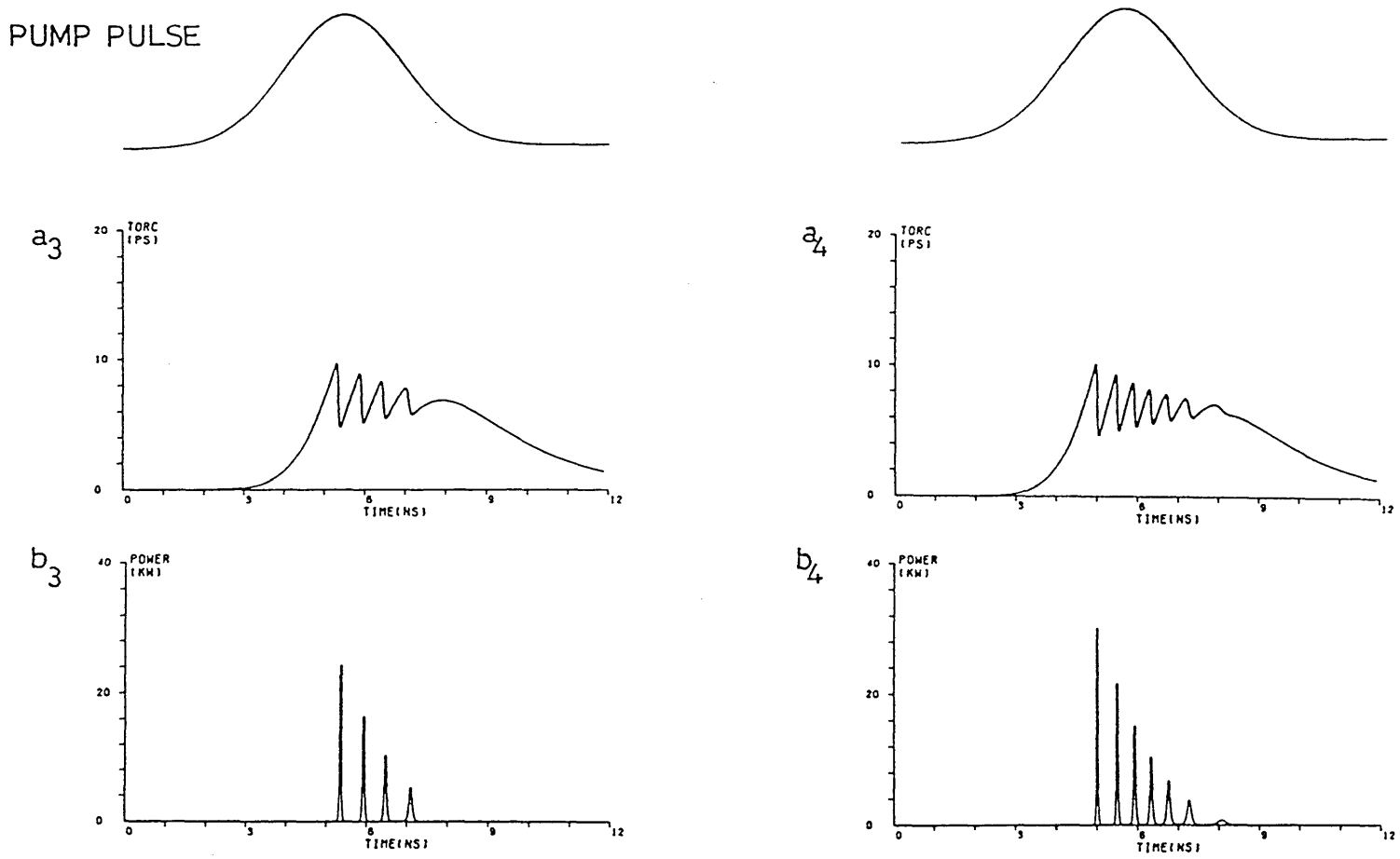


Figure 3.2. (Part 2) Computer solutions of the coupled rate equations.

a_1-a_4: equivalent cavity decay time, b_1-b_2: output power of the DFDL.

The relative pumping rates are 1.25, 1.5, 2.0 and 2.5 respectively.

The normalized unit pumping rate ($I_p \sigma_p N$) is 5.05×10^{25} $cm^{-3}s^{-1}$, corresponding to 4.83 kW.

Gaussian pump pulse was chosen to be 3.5 ns.

The general features of the computer results may be summarized as follows. There is a threshold pumping rate above which lasing occurs. Within a specific range of pumping rate above the threshold, a single pulse is emitted. As the pumping rate is increased, two or more discrete pulses are emitted. The actual number of pulses in the pulse train depends on the pumping rate. The duration and the intensity of the pulses vary within a pulse train. From the first pulse to the last in a pulse train, the power gradually drops and the pulse-width increases; that is, the first pulse has the highest power and the shortest pulse-width. The separation between two consecutive pulses varies without any general trend. The duration of the first pulse always decreases and its power increases with increasing pumping rate.

Single pulse emission occurs for values of pumping rate lying between 1.0 and 1.38 times the threshold value in this particular example. Typically, the duration of the single DFDL pulse can be shorter than the pumping pulse by a factor of 50 to 100. Clearly, the distributed feedback dye laser provides an effective way of generating short pulses from relatively long pump pulses. Some possibilities of generating shorter pulses will be examined in the next section.

Some more general characteristics of the pulses generated with a DFDL laser have been studied theoretically using this model and will be presented in Chapter 4, together with the results from a different model. Important features will then be discussed in detail.

3.4 Generation of Shorter DFDL Pulses

Distributed feedback dye lasers have been well known as tunable narrow linewidth light sources for a long time. However, there has been increasing interest in the transient behaviour of these lasers recently. Until a few years ago, the only reliable way of obtaining ultrashort light pulses was by the mode-locking technique; ultrashort pulse generation by distributed feedback dye lasers now offers an alternative way of obtaining picosecond light pulses. In this section, we shall consider two ways of obtaining shorter DFDL

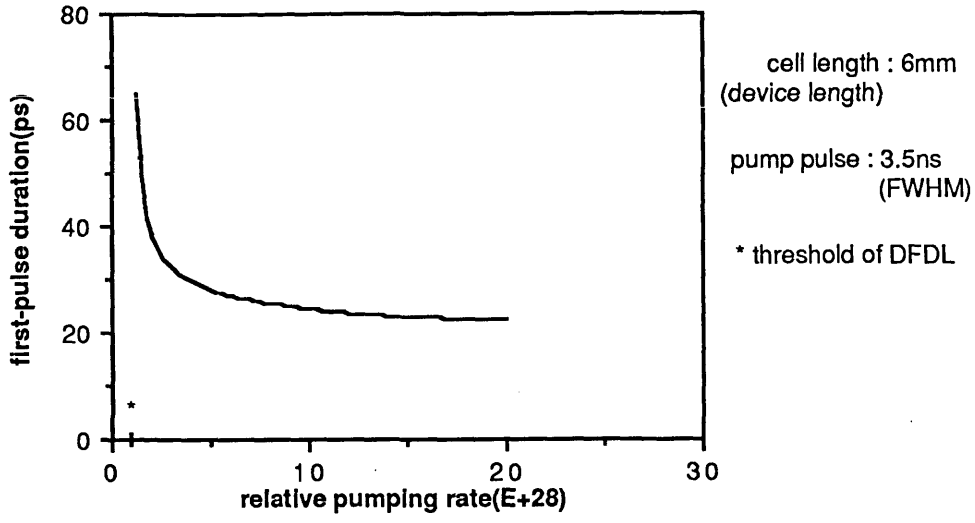
pulses theoretically using the computer program developed at Imperial College. Other possibilities of generating shorter pulses will be discussed in later sections.

The computer solutions of the coupled-rate equations described above has revealed the trend that the duration of the first pulse decreases as the pumping rate is increased. Therefore shorter DFDL pulses may be produced simply by using a higher pumping rate. This possibility has been investigated theoretically by us. A typical computer result is presented in Figure 3.3. As expected, the duration of the first pulse decreases as the pumping power is increased. However, the decrease in the pulse duration slows down considerably when the pumping power is increased to about five times the threshold value. Further increase in pumping power only produces a small amount of further pulse shortening.

Nevertheless, the duration of the first pulse can easily be halved by operating the laser at around three times the threshold value in this particular example. At this pumping power level, the temporal structure of the laser is as shown in Figure 3.4. Since the durations of the individual pulses are different and the separations of the pulses are variable, such a pulse train would not find many applications. It is desirable to have single-pulse operation; this can be achieved if the rest of the pulse train, other than the first pulse, is suppressed. This is exactly what Bor and Schäfer [14] have tried. In their experiment, a properly timed quencher dye laser pulse of adequate energy was injected into the DFDL cavity at a small angle to extract part of the stored energy so that the threshold population inversion was never reached again after the emission of the first pulse. The fast leading edge of this quencher pulse was injected into the laser cavity before the build-up of the second pulse starts. Hence, only the first DFDL pulse was generated and all the later pulses were quenched. This technique has several advantages. Firstly, the DFDL pulse duration can easily be shortened by a factor of two. Secondly, the shot-to-shot stability of the DFDL pulses is excellent. This can be deduced from Figure 3.5. Small variation of the pumping power does not seriously affect the pulse duration or the pulse energy of the first pulse if a high pumping power is used.

However, the technique cannot be taken much further than this because of several limitations. Firstly, as we have pointed out,

Figure 3.3 Dependence of pulse duration on pumping rate



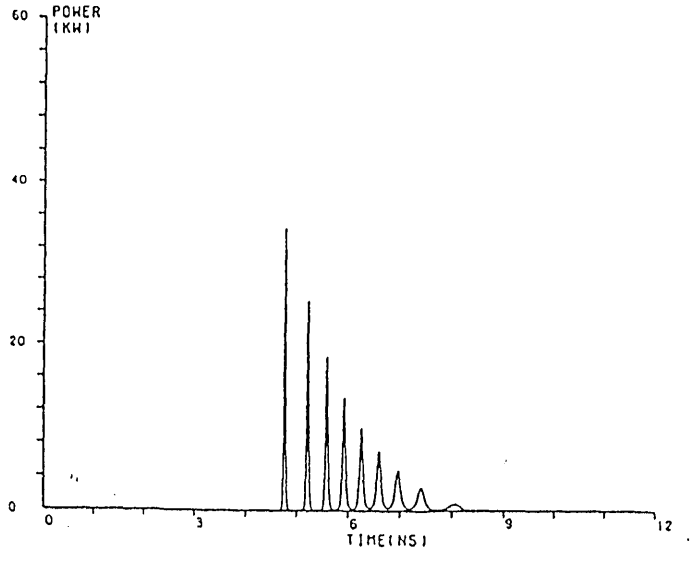
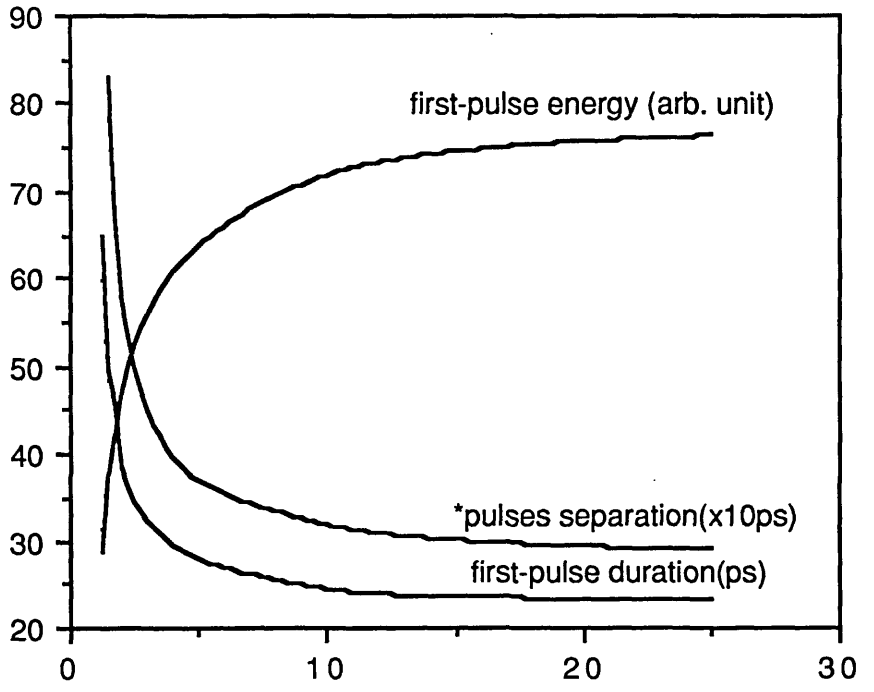


Figure 3.4. Output power of a DFDL with moderate pumping rate.

Figure 3.5 Temporal and energy characteristics of a DFDL



cell length : 6mm

pump pulse : 3.5ns (FWHM)

*pulse separation between first & second pulse at the threshold of the third pulse

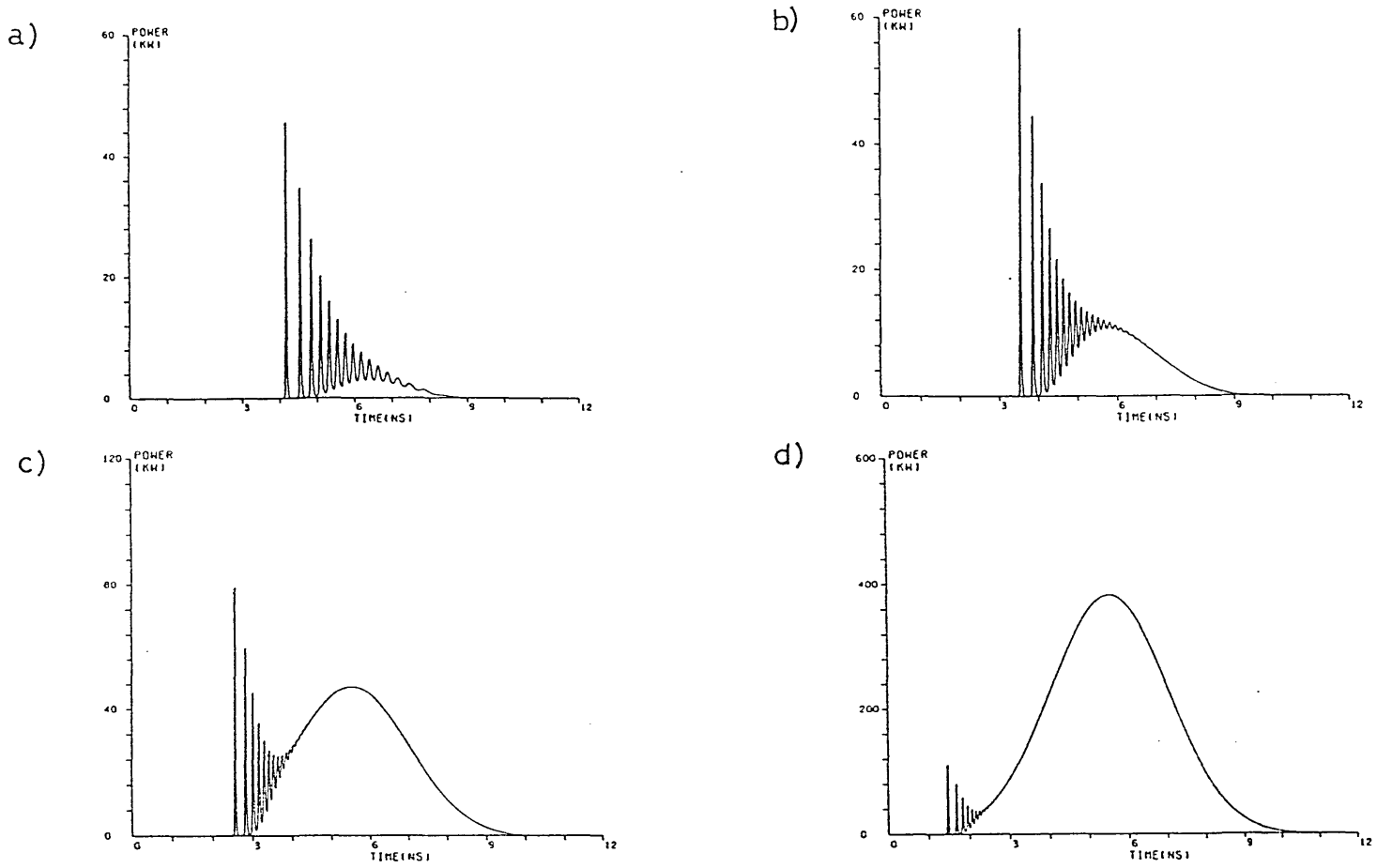


Figure 3.6 Output power of a DFDL with high pumping rate.
Relative pumping rates are a) 5, b) 10, c) 40, d) 320, respectively.
(Threshold pumping rate = 1)

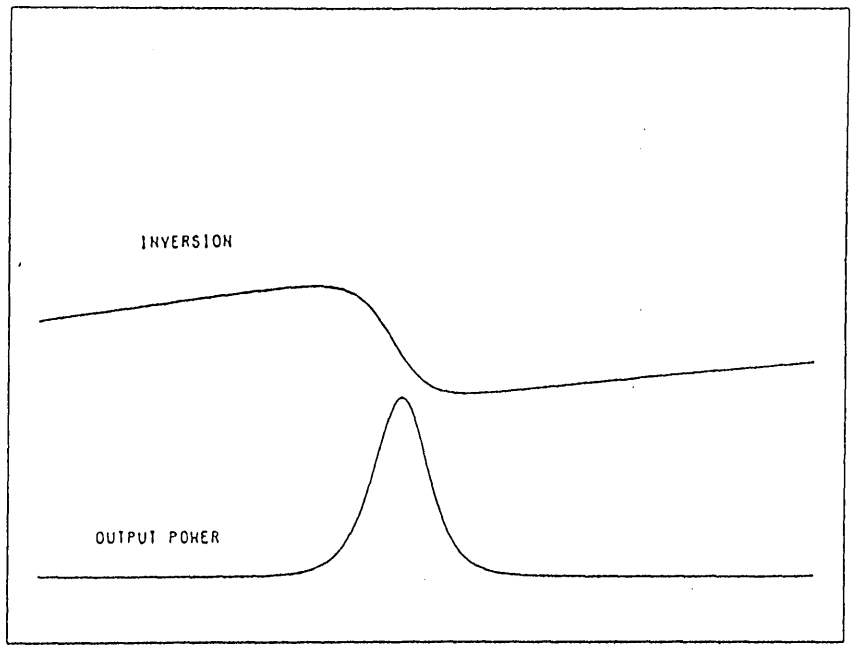
a much larger increase in pumping power is required to produce even a small degree of further pulse-shortening. Secondly, as shown in Figure 3.5, the separation between the first pulse and the second pulse also decreases with increasing pumping power. The practical implications are that the timing of the quenching pulse becomes more critical and that a sharper leading edge of the quencher pulse may be required. Also, at high pump power and in the absence of a quencher pulse, only a small fraction of the pump energy is converted into the first DFDL pulse, a large amount of this excitation energy would end up in the remaining DFDL pulses. Hence, for successful quenching, the energy of the quencher pulse must be increased when the pump power increases. However, a high energy quencher pulse may not be readily available and may considerably complicate the entire experimental arrangement. In addition, the efficiency of the entire system will be lowered significantly since a large amount of energy is wasted in the quenching process.

It is interesting to consider the temporal behaviour of the entire DFDL pulse train under high pumping power. Our computer simulations (Figure 3.6) show that there is a fundamental change in the temporal characteristics. Instead of producing more discrete pulses as the pumping power is increased, a broad "background" now emerges at the end of the pulse train (Figure 3.6a). Higher pumping power produces more pronounced "background" and the pulses at the back of the pulse train can now only be regarded as some ripples on the broad "background" (Figure 3.6b). Further increase in the pumping power reveals that the shape and size of this "background" follows the pumping pulse very closely indeed (Figure 3.6c). This profile in fact becomes the dominant feature in the output of the DFDL under very high pumping power and its peak power eventually exceeds that of the narrow first pulse (Figure 3.6d).

In the remainder of the section we shall discuss the possibility of generating shorter DFDL pulses with external feedback.

The basic physical mechanism of short-pulse formation for the distributed feedback dye laser can be attributed to the interplay between the optical field in the laser cavity and the population inversion. Pulses are formed while the population inversion is oscillating about the threshold value. This is illustrated in Figure 3.7. When a pulse is formed, the population inversion drops from a value above the threshold to a value below. It can also be deduced

Figure 3.7. The formation of an ultrashort pulse in a DFDL.



that the duration of the pulse depends strongly on the total fall of population inversion (see section 4.4). A fast depletion of population inversion clearly will give rise to a short pulse.

Imagine that the population inversion has almost reached its peak and that a pulse is just about to be emitted. If the number of cavity photons suddenly goes up, the population inversion will be forced to drop at a faster rate than it otherwise would; a shorter pulse will be emitted.

This special situation can be arranged by injecting a coherent short pulse into the laser cavity at the right instant. One way of achieving this is by re-injecting the very DFDL pulse back into the cavity just before the expected time for the emission of the next pulse. This may be conveniently arranged by the use of an external "mirror".

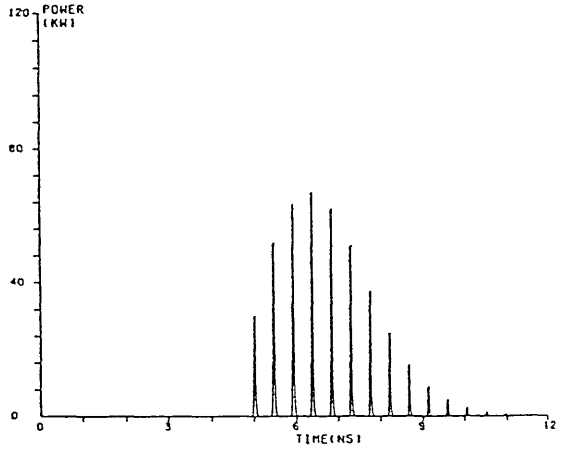
This particular possibility of generating shorter pulses was investigated using a modified version of the computer program based on the rate equation model. A hypothetical external feedback mechanism, which would re-inject the output pulse back into the laser cavity after a specific time-delay, is assumed. The time-delay and the amount of feedback may be varied.

A typical computer result is shown in Figure 3.8. The temporal profile for the normal DFDL (without external feedback) is also inserted for comparison. In this particular example, the reflectivity of the external minor equals 0.5.

In the case of a normal DFDL without external feedback it is convenient to refer to the separation between the first and second pulse as t_{12} and the duration of the first pulse as Δt_1. The time-delay between the emission and the re-injection of a pulse will be referred to as the "external round-trip time". It was found that the temporal structure could be seriously affected by this parameter. The optimum value of this external round-trip time was found to be about "$t_{12} - 1.25\Delta t_1$". If the external round-trip time differed from this optimum value by more than $0.75\Delta t_1$, irregular temporal structure would appear.

As shown in Figure 3.8, the duration of the pulse is gradually shortened after successive re-injections. However, due to the smaller pumping rate at the end of the pulse train, the pulse duration gets broadened towards the end. Somewhere in the middle, there is an intense pulse with minimum duration. The width of this

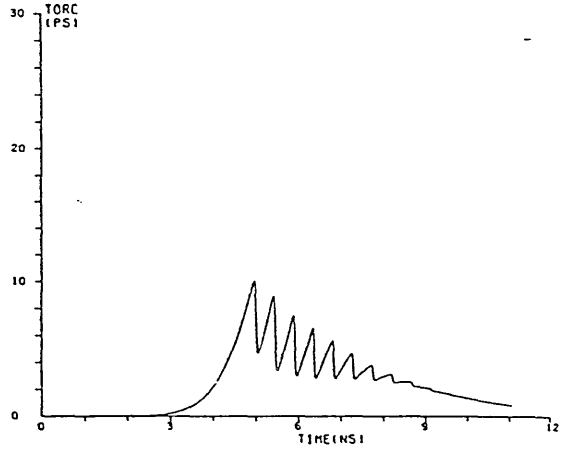
a)



b)

pulse number	TIME(E-08)	PEAK(E+05)	duration (10^{-10}s)
1	0.501	0.302	0.354
2	0.547	0.519	0.335
3	0.592	0.633	0.300
4	0.638	0.668	0.275
5	0.684	0.620	0.262
6	0.730	0.507	0.259
7	0.776	0.370	0.262
8	0.822	0.246	0.269
9	0.868	0.152	0.276
10	0.914	0.088	0.280
11	0.960	0.049	0.284
12	1.006	0.026	0.286
13	1.052	0.014	0.287

c)



d)

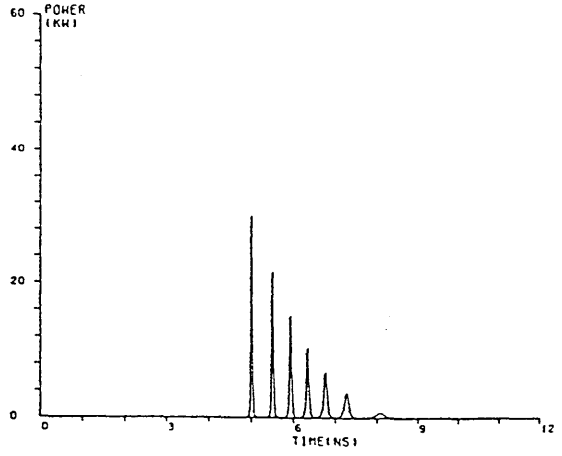
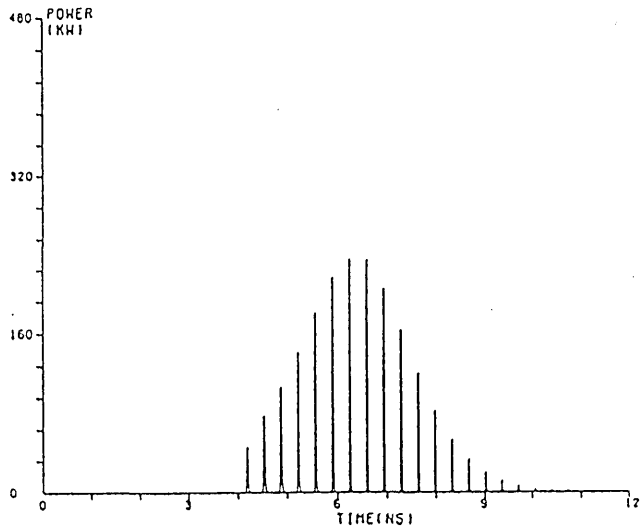


Figure 3.8 Temporal structure of a DFDL with external feedback.
a) Output power with external feedback, b) pulse durations,
c) equivalent cavity decay time profile, d) output power without feedback.

a)



b)

PULSE NUMBER	TIME(E-08)	PEAK(E+05)	DURATION (10^{-10} s)
1	0.419	0.456	0.286
2	0.453	0.773	0.264
3	0.487	1.060	0.230
4	0.522	1.409	0.194
5	0.556	1.807	0.162
6	0.591	2.166	0.139
7	0.625	2.372	0.125
8	0.660	2.334	0.120
9	0.695	2.057	0.121
10	0.729	1.638	0.128
11	0.764	1.200	0.138
12	0.799	0.821	0.152
13	0.833	0.534	0.165
14	0.868	0.332	0.177
15	0.902	0.199	0.188
16	0.937	0.115	0.196
17	0.971	0.065	0.202
18	1.006	0.036	0.207
19	1.040	0.019	0.210
20	1.075	0.010	0.212

Figure 3.9. DFDL output with external feedback - high pumping rate.
a) output power; b) durations of the pulses (the fourth column).

pulse is smallest when the external round-trip time is at its optimum value.

The minimum pulse-width also depends on the reflectivity of the external mirror. With higher reflectivity, the minimum pulse-width achieved will be smaller.

Pulse shortening with an external "mirror" can be more effective if a high power pump pulse is used. An example is given by Figure 3.9. The pumping power is twice as much as before. The minimum pulse-width achieved with this pumping power is shorter than the previous case by a factor of just over two. Also, although the pumping power is fairly high, the pulses emitted are still discrete.

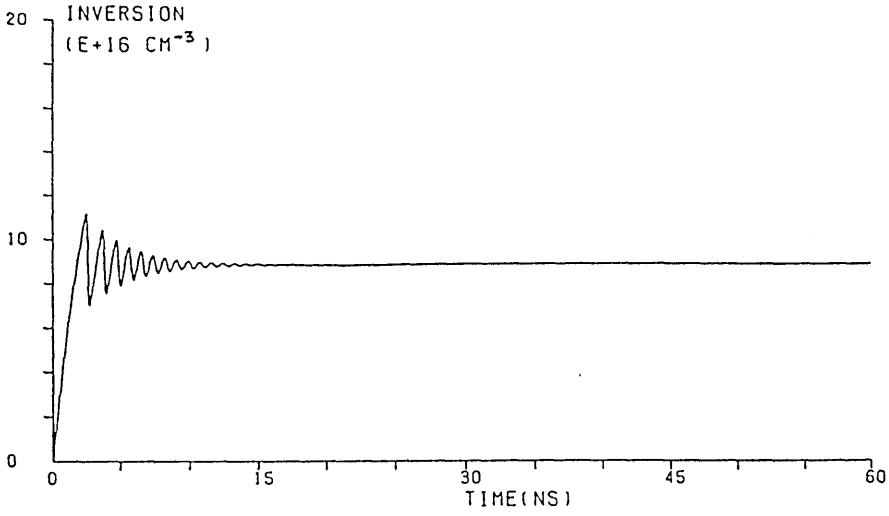
The broadening of the pulses towards the end of the Gaussian pump pulse seemed to be due to the low values of the instantaneous pumping rate. To test this theory, an appropriate constant pumping rate was used in a computer simulation instead of the Gaussian pump pulse. Figure 3.10 is the temporal profile of a normal DFDL (without external feedback) under the constant pumping rate condition. Note that this is equivalent to cw operation. When some external feedback is introduced, the temporal structure changes dramatically (Figure 3.11). The variation of the pulse-width with pulse number is shown on the graph below (Figure 3.12). The pulse number gives the position of the pulse concerned in the pulse train. Clearly, the pulses never get broadened at any stage.

Another feature of the DFDL with an external "mirror" is that the spacing of the pulses is constant. Moreover, this temporal spacing is directly related to the position of the external "mirror" and therefore is more controllable.

Note that in using this computer model, a few factors have been neglected. Firstly, we have ignored the non-zero transit time across the DFB structure; we assumed that the injected photons were uniformly distributed along the cavity immediately upon re-injection. This assumption may be far from perfect since the distributed feedback structure does give rise to some back scattering. Secondly, the external "mirror" or "mirrors" may lead to an additional longitudinal mode structure. An arbitrary position of the "mirror" may not be compatible with the gain grating structure since the phase of the returning optical wave may be of critical importance.

We have considered two specific possibilities of generating shorter pulses. There are also some other methods of producing

a)



b)

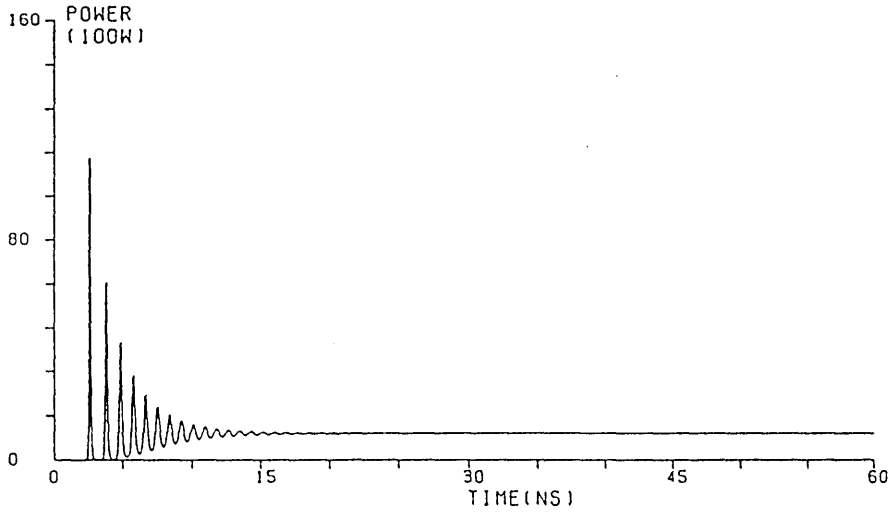


Figure 3.10. Temporal structure of a DFDL with a constant pumping rate:
a) population inversion profile, b) output power.

Figure 3.11. DFDL output with external feedback — constant pumping rate.

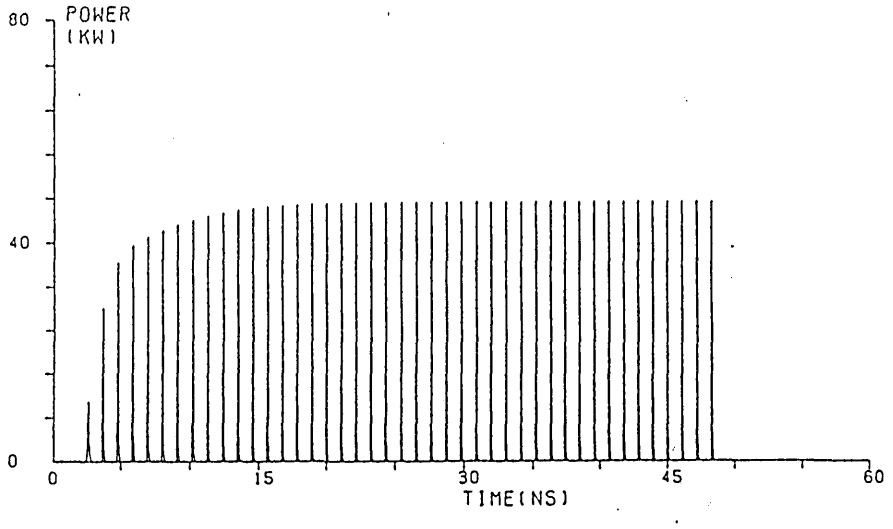
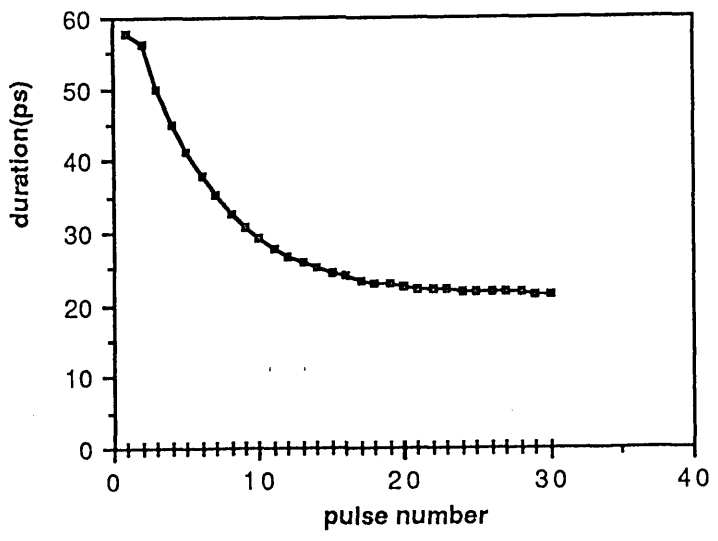


Figure 3.12 Variation of pulse-width with pulse number



shorter DFDL pulses such as using a short-duration pump pulse or a short device length. These will be discussed in the next chapter after the pulse-forming mechanism has been more thoroughly examined.

3.5 Comments on the Equivalent Cavity Decay Time

The rate equation model has been shown to be quite successful in explaining some of the temporal characteristics of the distributed feedback dye laser. The key parameter of the model is the equivalent cavity decay time τ_c. It was shown to be a time-dependent parameter via its relationship to the instantaneous population inversion [10]. Moreover, this time-varying nature was often regarded as the cause of the formation of ultrashort pulses in DFDLs. In this section, we shall examine the validity of the use of this important parameter τ_c. As will be shown, there are a few discrepancies between the physical characteristics of the gain-coupled distributed feedback laser and the features implied by the expression of τ_c as given in equation (3.6).

First of all, we shall describe the derivation of the expression for τ_c. Some important equations used in the derivation of τ_c were first derived by Haus [15] to obtain an approximate analytic expression for the power emitted by the overcoupled distributed feedback laser with refractive-index perturbation. The basic coupled-wave equations (equation (2.20)) used have been modified to

$$-R' + (\alpha_0 - \alpha_L - i\delta)R = i\kappa S, \tag{3.15}$$

$$S' + (\alpha_0 - \alpha_L - i\delta)S = i\kappa^* R. \tag{3.16}$$

Here, α_L is the loss coefficient per unit length and κ^* is the complex conjugate of the coupling constant κ. Differentiating equation (3.15) gives

$$-R'' + (\alpha_0 - \alpha_L - i\delta)R' = i\kappa S'. \tag{3.17}$$

If we eliminate S by substituting equation (3.15) into (3.16), multiply the result by $i\kappa$, and then eliminate S' by substituting the resulting equation into (3.17), the following differential equation

will be obtained:

$$R'' = \left[|\kappa|^2 + (\alpha_0 - \alpha_L - i\delta)^2\right]R, \tag{3.18}$$

where $|\kappa|^2$ is equal to $\kappa\kappa^*$. The solution to equation (3.18) may take the form of

$$R = A \exp(\pm i\xi z), \tag{3.19}$$

where ξ is given by

$$-\xi^2 = |\kappa|^2 + (\alpha_0 - \alpha_L - i\delta)^2. \tag{3.20}$$

Equation (3.20) is equivalent to the dispersion relation derived in Chapter 2 and ξ is related to γ by

$$\xi = \pm i\gamma. \tag{3.21}$$

Haus considered a structure containing a mode of high external quality factor so that the power escaping from the ends per cycle is only a small fraction of the energy stored in the cavity. He argued that the amplitudes of the counter-propagating R and S waves at the ends of the structure will then be small compared with their maximum values inside the structure so that a good approximation for the distribution of R would be given by

$$R = A \cos \xi z, \tag{3.22}$$

with nodes at the ends of the laser device where $z = \pm L/2$. This implies that

$$\xi L = m\pi. \tag{3.23}$$

The field distribution described above is a good approximation for an overcoupled laser (see Figure 2.9). If we consider a structure with no net gain or loss (i.e. $\alpha_0 - \alpha_L = 0$), equation (3.20) may be re-written as

$$\delta L = \pm |\kappa L| \left[1 + \frac{(\xi L)^2}{|\kappa L|^2}\right]^{1/2}. \qquad (3.24)$$

Substitution of equation (3.23) gives

$$\delta L = \pm |\kappa L| \left[1 + \frac{m^2\pi^2}{|\kappa L|^2}\right]^{1/2}. \qquad (3.25)$$

Now equation (3.22) may be substituted into equation (3.15) with the condition $\alpha_0 - \alpha_L = 0$, hence

$$S = \frac{\xi}{i\kappa} A \sin \xi z - \frac{\delta}{\kappa} A \cos \xi z. \qquad (3.26)$$

For an overcoupled laser with

$$|\kappa L| >> m\pi, \qquad (3.27)$$

the magnitude of δ (equation (3.25)) may be approximated by

$$|\delta| \simeq |\kappa|. \qquad (3.28)$$

Therefore the profile of S expressed in equation (3.26) is approximately given by

$$|S| \simeq |A \cos \xi z| \simeq |R|. \qquad (3.29)$$

Hence the R wave and the S wave have similar intensity distribution profiles.

We noted that at $z = - L/2$, R is at a node (Figure 2.1); that is, $R = 0$. Therefore, we have from equation (3.15)

$$S_e = \frac{-R'(L/2)}{i\kappa}, \qquad (3.30)$$

where S_e is the value of S at $z = - L/2$. It can be shown that $R'(-L/2)$ is equal to ξA. And using equation (3.23), an expression for the light intensity at this end ($z = - L/2$) of the laser can be obtained:

$$|S_e|^2 = \left[\frac{m\pi}{|\kappa| L}\right]^2 |A|^2. \qquad (3.31)$$

Similarly, at the other end of the laser ($z = + L/2$)

$$|R_e|^2 = \left[\frac{m\pi}{|\kappa|L} \right]^2 |A|^2. \tag{3.32}$$

The remaining steps of the derivation of the equivalent cavity decay time τ_c were taken up by Chinn [13] by considering the end losses and internal energy storage of the distributed feedback structure. He started his analysis with an alternative form of equation (3.29):

$$|R| \simeq |S| \simeq A\, f(x,y) \cos \xi z; \tag{3.33}$$

a transverse spatial dependence described by $f(x,y)$ is included. And the square of the field amplitude at each end of the laser device is given by

$$|R_e|^2 = |S_e|^2 \simeq \left[\frac{m\pi}{|\kappa|L} \right]^2 A^2 f^2(x,y). \tag{3.34}$$

The total light energy escaping from the structure is proportional to

$$2\left[\frac{m\pi}{|\kappa|L}\right]^2 A^2 \iint f^2(x,y)\, dx\, dy, \tag{3.35}$$

and the rate of loss of photons $\dot{q}$ is given by

$$\dot{q} = 2\left[\frac{m\pi}{|\kappa|L}\right]^2 A^2 \frac{c}{\eta} \frac{\varepsilon}{h\nu} \iint f^2(x,y)\, dx\, dy, \tag{3.36}$$

where ε is the electric permittivity of the medium.

Now the total number of photons inside the cavity (q) can be found by integrating $(RR^* + SS^*)$ over the device length and the transverse cross-section using equation (3.33) and then multiplying the result by $\varepsilon/h\nu$:

$$q = 2\left[\left(\frac{1}{2} L\right)A^2\right] \frac{\varepsilon}{h\nu} \iint f^2(x,y)\, dx\, dy. \tag{3.37}$$

Then the equivalent cavity decay time, which is defined as the ratio of the total number of photons in the laser cavity to the rate of loss of photons ($q/\dot{q}$), can be obtained:

$$\tau_c = \frac{\eta L}{2c} \left[\frac{|\kappa| L}{m\pi}\right]^2. \qquad (3.38)$$

The integer m is related to the mode number of the resonance mode and for a first-order mode m is equal to one. Hence, the equivalent cavity decay time for a first-order overcoupled distributed feedback laser is given by

$$\tau_c = \frac{\eta L}{2c} \left[\frac{|\kappa| L}{\pi}\right]^2. \qquad (3.39)$$

This is the expression used by Bor [10] in his rate equation model of distributed feedback dye lasers.

A careful examination of the assumptions in the derivation would raise a few questions on the validity of the use of this expression for gain-coupled distributed feedback dye lasers.

Compare the basic coupled-wave equations (3.15) and (3.16) with those derived by Kogelnik and Shank (equation (2.20)). The use of κ^* in equation (3.16) implies that index-coupling has been assumed. In fact, this was explicitly stated by Haus [15].

The approximate solution of equation (3.22) works well for the case of index-coupling. However, for our gain-coupled laser, pumped by two equal intensity interfering beams, operated at the Bragg frequency, this approximation may not be justified. For, in this case, the value of γ, which can be calculated from equation (2.31), is a real numerical quantity. This means that ξ, which is equal to $\pm i\gamma$, is completely imaginary and equation (3.23) can never be satisfied. Another question arises in the approximation of equation (3.28). Since our laser is operated at the Bragg frequency, the value of δ is exactly equal to zero. Therefore equation (3.28) does not hold.

One of the most important assumptions made in the derivation of τ_c was that the laser was considered to be overcoupled. However, it can be shown that this assumption may not be valid. In fact, we can calculate the relative field distribution for our gain-coupled DFDL in the steady-state condition.

For a gain-coupled laser operating at the Bragg frequency (δ = 0), the dispersion relation (2.31) becomes

$$\gamma^2 = (i\alpha_1/2)^2 + (\alpha_0)^2. \tag{3.40}$$

Since the periodic modulation is accomplished by the interference of the pumping beam, α_1 can be expressed as

$$\alpha_1 = V\alpha_0. \tag{3.41}$$

Hence, the dispersion relation takes the form

$$\gamma^2 = \alpha_0^2 \left(1 - \frac{V}{4}\right), \tag{3.42}$$

and γ is given by

$$\gamma = \pm \alpha_0 \left(1 - \frac{V}{4}\right)^{1/2}. \tag{3.43}$$

Therefore, γ is a real quantity and the field distribution of R expressed in equation (2.28) is a real hyperbolic sine function, i.e.

$$R = A \sinh \gamma(z + L/2), \tag{3.44}$$

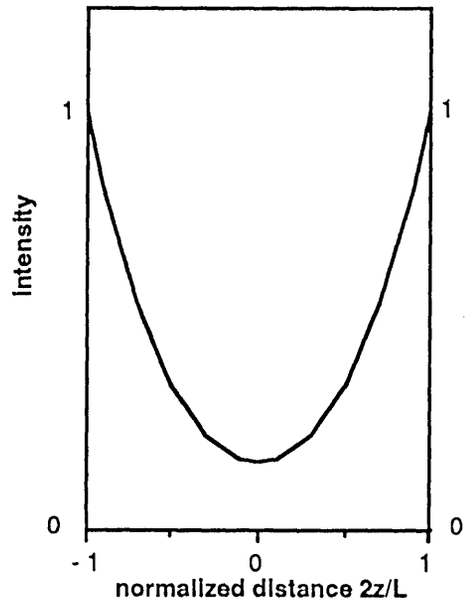
and similarly,

$$S = \pm A \sinh \gamma(z - L/2), \tag{3.45}$$

where A is a real quantity.

The point to note is that these field distribution functions cannot possibly be approximated by the cosine function as suggested in equation (3.22). Moreover, even the relative intensity distribution, $RR^* + SS^*$, is not compatible with the overcoupled pattern. Figure 3.13 is our calculation of the intensity distribution. This particular intensity pattern, in fact, is very similar to that obtained by Duling III and Raymer [16]. They investigated the time behaviour of the gain-coupled distributed feedback dye laser power output using a semiclassical theory which took into account the field propagation within the laser cavity. They found that in the case of steady-state operation, the gain-coupled DFDL is always undercoupled. Note that the introduction of a loss term α_L does not affect the general result so long as the visibility of the interference fringes is not affected by it. Hence,

Figure 3.13 Steady-state spatial intensity distribution



we can conclude that for the gain-coupled laser, the overcoupled condition can never be reached in the steady state or below the threshold. In fact, Duling III and Raymer have shown that in some cases the laser remains undercoupled even when the threshold has been exceeded. From their results of intensity distribution one can see that the "cosine" approximation for the field distribution (equation (3.22)) can hardly be justified [10]. Yet the calculations by Bor [10] using the τ_c expression suggest that the overcoupled condition is reached well below the threshold when the population inversion is only at about half of the threshold value. Clearly, the use of this τ_c expression may not be appropriate in the case of the DFDL.

The threshold-gain value $\alpha_0 L$ for the gain-coupled DFDL can be calculated, using the coupled-wave model, by solving the eigenvalue equation (2.32), which is

$$\kappa = \pm\, i\gamma/\sinh \gamma L. \tag{3.46}$$

Using equations (2.18), (3.41) and (3.43) and assuming that the visibility V is equal to 1, the eigenvalue equation can then be solved to obtain the results

$$\gamma L = 1.317, \tag{3.47}$$

and

$$\alpha_0 L = 1.52. \tag{3.48}$$

The steady-state value of $\alpha_0 L$ for Bor's rate equation model can also be calculated using equations (3.7) and (3.11) and the condition that V = 1. It is given by

$$\alpha_0 L = 2(\pi)^{2/3} = 4.29. \tag{3.49}$$

Again, this is inconsistent with the prediction based on the coupled-wave theory as given in equation (3.48).

In this section we have carried out the derivation of the equivalent cavity decay time τ_c. We have taken a closer look at the assumptions made in the derivation and raised a few questions on the validity of these assumptions for our particular type of lasers. We have also pointed out some discrepancies between the theory involving

the parameter τ_c and the other established theories. In particular, it was found that the important assumption of overcoupled operation could not be justified for the gain-coupled distributed feedback dye laser.

3.6 Conclusion

The basic elements of the rate equation model have been described in this chapter. They were used to simulate the generation of ultrashort pulses with the gain-coupled distributed feedback dye laser. Some typical computer solutions were obtained. The computer program developed during the course of this work has also been used to investigate two specific possibilities of generating shorter pulses; the laser action under high pumping power and the effect of a hypothetical external reflector were simulated using modified versions of the computer program. Although the basic results of the rate equation model were in good qualitative agreement with existing experimental results, there are, however, some doubts as to the validity of the use of the equivalent cavity decay time in the rate equation model for the DFDL. In Chapter 4 we shall continue to explore the pulse-forming mechanism with a modified rate equation model. In this new model, an appropriate cavity decay time will replace the one expressed in equation (3.8). It is only an approximate model; however, by approaching the same problem from a different angle, this model will provide an indirect way of exploring the physical mechanism responsible for the generation of short pulses by the gain-coupled distributed feedback dye lasers.

CHAPTER 4

RATE EQUATION MODEL OF UNDERCOUPLED DISTRIBUTED FEEDBACK DYE LASERS

4.1 Introduction

The rate equation model developed by Bor seems to be fairly adequate in describing the temporal behaviour of the gain-coupled distributed feedback dye laser (DFDL). The computer solutions of the equations were in good qualitative agreement with experimental observations. However, as we pointed out in the last chapter, the use of the equivalent cavity decay time in the rate equation model may not be appropriate.

Although a more rigorous theory on the time-dependent behaviour of the gain-coupled DFDL has recently been developed, the study of the physical origin of the mechanism behind the generation of ultrashort pulses by the DFDL has been far from thorough. In particular, the effect of the varying nature of the equivalent cavity decay time has never been seriously examined but has been in the past given as the main cause for the formation of ultrashort pulses.

In this chapter, we shall explore the mechanism of pulse formation using a simple theoretical model. This model is also based on the coupled rate equations but the equivalent cavity decay time is replaced by an appropriate constant cavity decay time, which corresponds to an undercoupled mode pattern. This is only an approximate model and is not as complete as some of the existing models. However, by approaching the same problem from a different angle, some of the underlying physical processes associated with pulse formation with DFDLs can be revealed in an indirect way. A reasonably accurate simple model may be much more effective in this respect than a full rigorous theory, the solutions of which can only be found by numerical computation. The relationships between different parameters and the interacting processes may not be so transparent in a complicated rigorous theory whereas simple analytical relationships may easily be derived from a simplified model. The results obtained from this new model will be compared with the results of the more rigorous and accurate theory. Any

discrepancy may well be due to the effect neglected in the original assumptions of the simplified model, in this case, the effect of the varying nature of the cavity decay time.

In the next section, an appropriate constant cavity decay time to be used in the new model will be proposed. Some computer solutions will also be presented. Comparisons between this new model and existing models will be the main subject of section 4.3. In section 4.4, approximate analytic expressions will be obtained from some simple algebraic analysis on the new set of photon rate equations. Comparisons with the results from full numerical computations will be given. Some of the relations derived with this approach will be shown to be consistent with experimental observations.

4.2 The Undercoupled DFDL Model

As pointed out in Chapter 3, the overcoupled approximation used by Bor may not be appropriate. It has also been shown [16] that the DFDL could be operating in an undercoupled condition throughout the entire process of pulse formation. It is therefore interesting to consider the transient behavour of the DFDL using an undercoupled approximation. In the following rate equation model, a constant cavity decay time corresponding to the undercoupled operation is used. As the pulse-formation process is associated with the oscillation of the population inversion about the steady-state threshold value, we shall choose the value of the cavity decay time corresponding to the steady-state condition. It is expected that the mean value of cavity decay time will be close to this threshold value. This is found to be consistent with the field intensity distribution pattern computed by Duling III and Raymer [16].

The calculation of this threshold cavity lifetime follows closely the approach used by Chinn [13]. We have shown in section 3.5 that the field distribution of the counter-propagating waves for the zeroth-order gain-coupled DFDL can be represented by real hyperbolic sine functions:

$$R = A \sinh \gamma(z + L/2), \tag{4.1}$$

and

$$S = \pm A \sinh \gamma(z - L/2). \tag{4.2}$$

Then, the square of the field amplitude at each end of the laser is given by

$$|R_e|^2 = |S_e|^2 = A^2 \sinh^2 \gamma L. \tag{4.3}$$

The total light intensity escaping from the structure is proportional to

$$2A^2 \sinh^2 \gamma L, \tag{4.4}$$

and the rate of loss of photons $\dot{q}$ is given by

$$\dot{q} = 2A^2 \sinh^2 \gamma L \, \frac{c}{\eta} \frac{\varepsilon}{h\nu} A_{xy}, \tag{4.5}$$

where A_{xy} represents the transverse effective area of the laser. The total number of photons inside the laser cavity, q, can be found by integrating $(RR^* + SS^*)A_{xy}\varepsilon/h\nu$ over the device length using equations (4.1) and (4.2):

$$q = \frac{2A^2}{\gamma} \left[\frac{1}{4} \sinh 2\gamma L - \frac{\gamma L}{2}\right] \frac{A_{xy}\varepsilon}{h\nu} . \tag{4.6}$$

The cavity decay time, τ_{cu}, defined as the ratio of the total number of photons in the laser cavity to the rate of loss of photons, may now be calculated using equations (4.5) and (4.6):

$$\tau_{cu} = \frac{\frac{1}{\gamma L}\left[\frac{1}{4} \sinh 2\gamma L - \frac{\gamma L}{2}\right]}{\sinh^2 \gamma L} \frac{\eta L}{c} , \tag{4.7}$$

where the second subscript on τ_{cu} denotes that the cavity decay time corresponds to an undercoupled approximation. The value γL for the gain-coupled DFDL has already been determined in Chapter 3. Substituting this value ($\gamma L = 1.317$), given by equation (3.48), into the above expression, the constant cavity decay time is obtained:

$$\tau_{cu} = 0.27 \frac{\eta L}{c} . \tag{4.8}$$

At first sight, it may seem unreasonable that the cavity decay time is shorter than the cavity transit time. However, its value is

Figure 4.1a Steady-state spatial intensity distribution

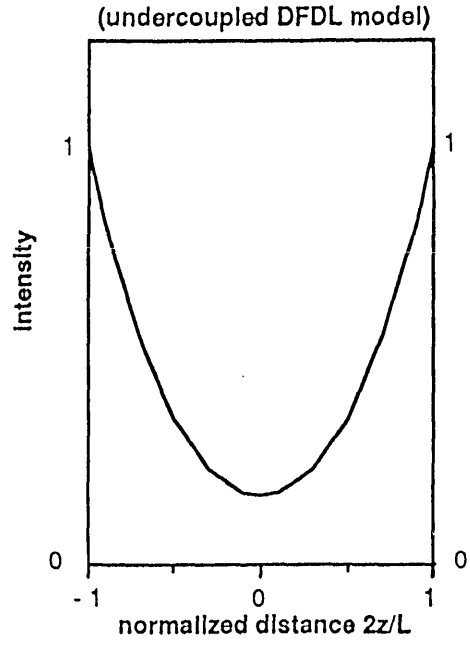


Figure 4.1b. Final intensity distribution for steady-state pumping (semi-classical model).

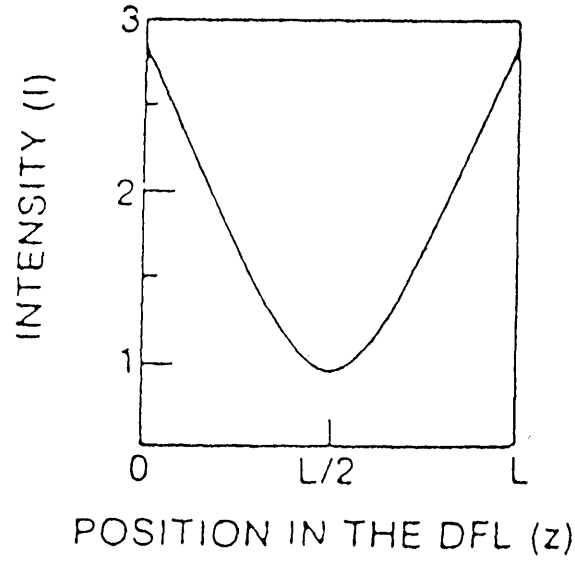
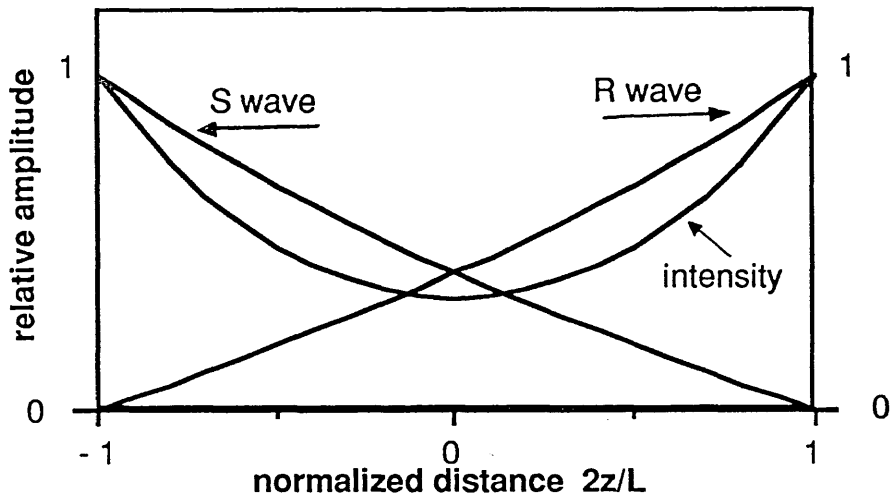


Figure 4.2 Coupled waves and spatial intensity distribution



in fact consistent with the results of the other established theories. In Bor's rate equation model, the value of the equivalent cavity decay time corresponding to the threshold population inversion was found to be 10.2 ps [10], whereas the corresponding cavity transit time for the 9 mm laser (with η = 1.44) was 43.2 ps. Also, in the semiclassical theory of DFDL [16], the durations of the pulses were found to be shorter than the cavity transit time, indicating that the absolute equivalent value of the cavity decay time may even be smaller.

It should be noted that the spatial intensity distribution ($RR^* + SS^*$) obtained by us (Figure 4.1a) and used in the derivation of τ_{cu} is very close to the steady-state intensity distribution calculated from the numerical computation (Figure 4.1b) using the semiclassical model [16].

It is more revealing to consider the relative amplitude distribution of the counter-propagating waves (Figure 4.2). The parameters used in the calculation of the curves in Figure 4.2 correspond to the zeroth-order gain-coupled DFDL (i.e. γL = 1.317). It can be seen that the photons leaking out at the left end of the laser are associated with the S wave. Now the field distribution of the S wave implies that most of these photons are generated near the left end of the laser. Similar arguments apply to the photons associated with the R waves. Therefore, the average time spent by the photons inside the laser cavity is less than the cavity transit time, resulting in a short cavity decay time. This argument is consistent with the spatial population inversion distributions calculated by Duling III and Raymer [16]. They showed that after the formation of a pulse, the original uniform distribution had been changed in a way which suggested that the depletion was heaviest near the ends of the laser device.

By replacing the time-dependent value of τ_c in the coupled rate equations (equations (3.1) and (3.2)) with this new constant cavity decay time τ_{cu}, we obtain a rate-equation model for the DFDL with an undercoupled approximation. These new coupled rate equations can now be solved exactly as described in section 3.3. Some typical results are shown in Figure 4.3. The parameters used in these calculations are also the same as those given in section 3.3.

It can be seen that these results are very similar to those obtained in section 3.3. Detailed comparisons between the results of

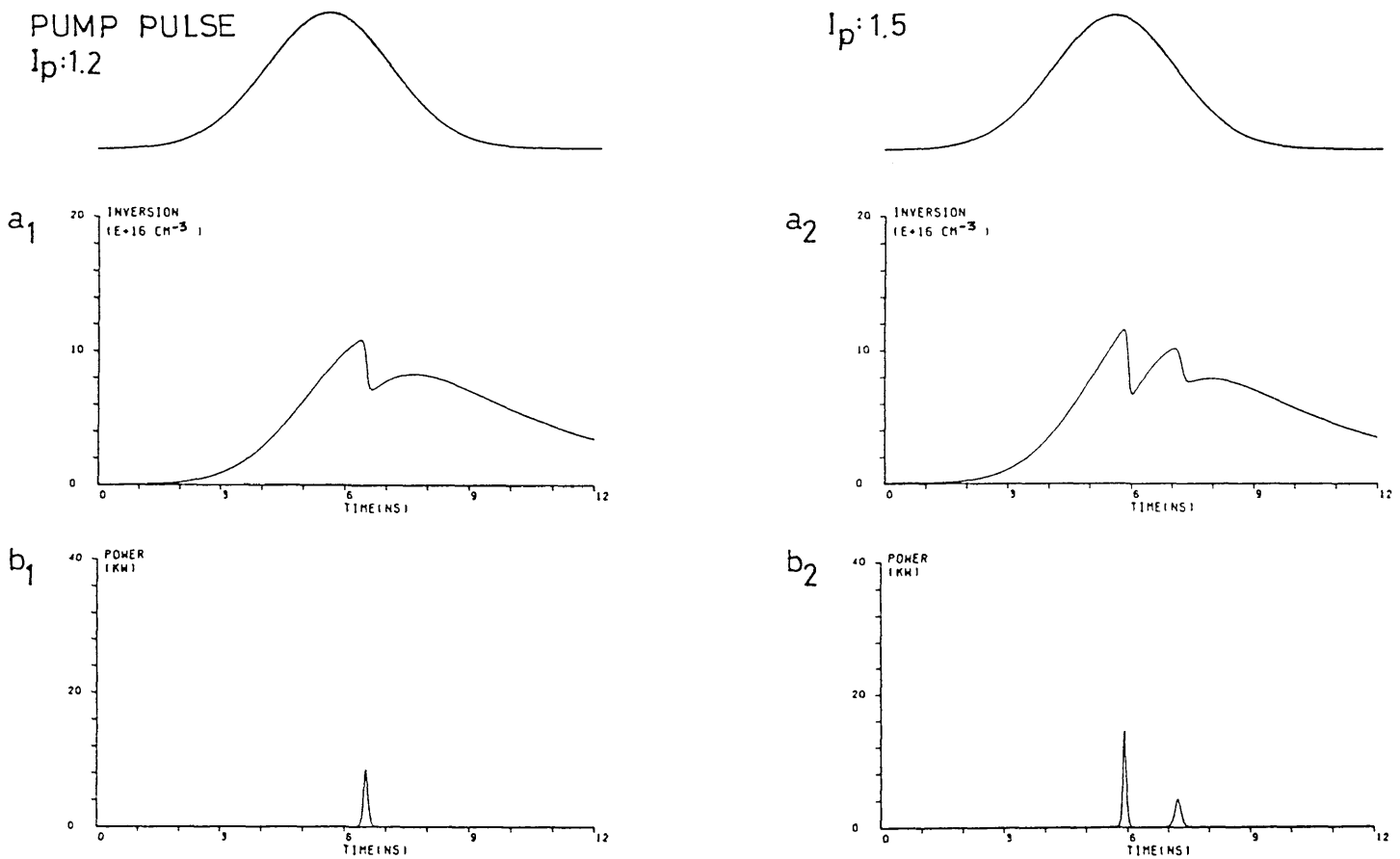


Figure 4.3 (Part 1) Computer solutions of the rate equations for an undercoupled DFDL with a constant cavity decay time τ_{cu}. a_1-a_4: population inversion profile, b_1-b_4: output power of the DFDL. The relative pumping rates are 1.2, 1.5, 2.0 and 3.0 respectively. Normalized unit pumping rate ($I_p\sigma_p N$) is 5.05×10^{25} $cm^{-3}s^{-1}$, corresponding to 4.83 kW.

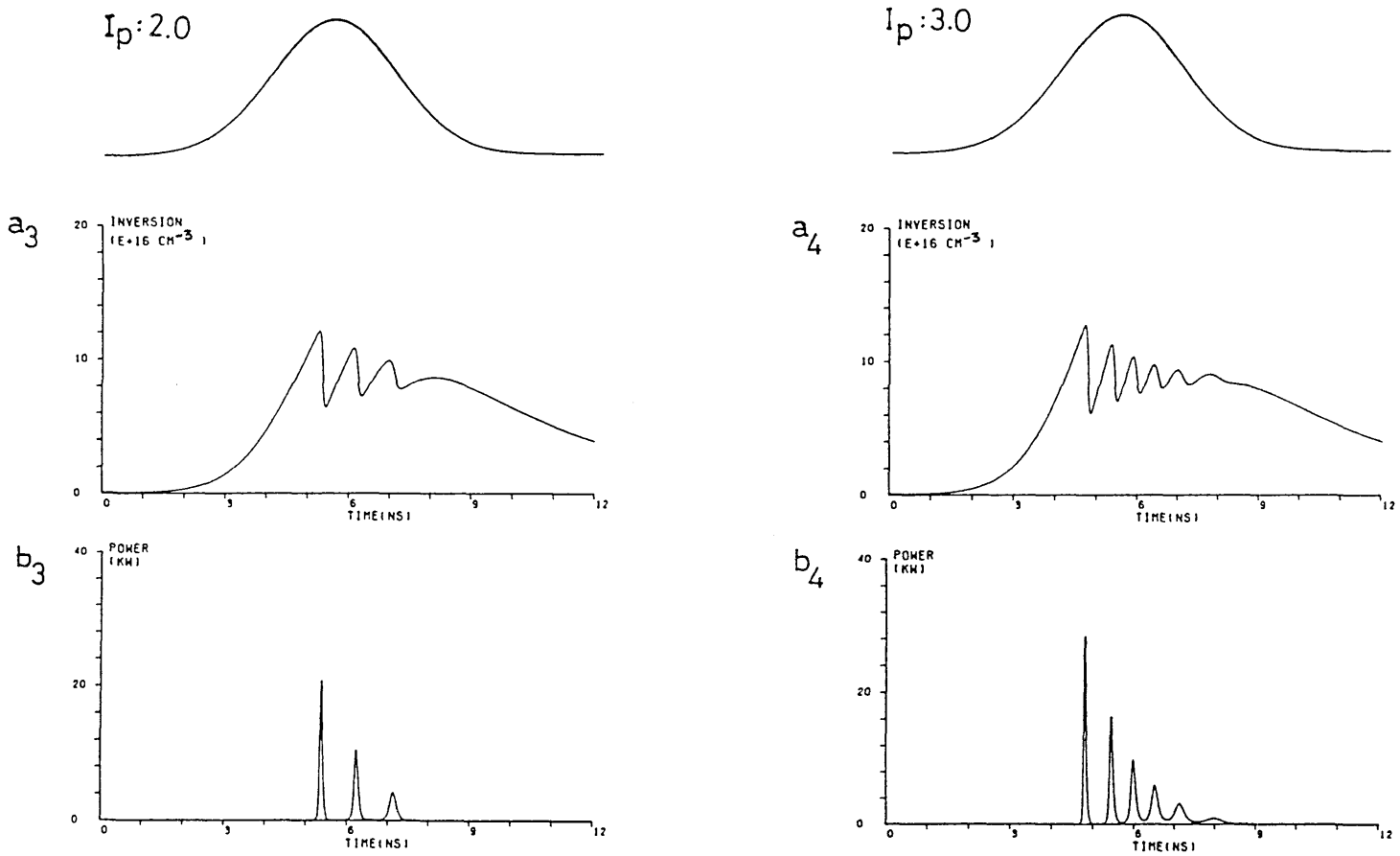


Figure 4.3 (Part 2) Computer solutions of the rate equations for an undercoupled DFDL with a constant cavity decay time τ_{cu}. a_1-a_4: population inversion profile, b_1-b_4: output power of the DFDL. The relative pumping rates are 1.2, 1.5, 2.0 and 3.0 respectively. Normalized unit pumping rate ($I_p \sigma_p N$) is 5.05×10^{25} $cm^{-3}s^{-1}$, corresponding to 4.83 kW.

the two-rate equation models and the semiclassical model will be the main subject of the next section. It is useful at this stage to consider the basic assumptions and the limitations of this undercoupled DFDL model.

First of all, the rate equation model is basically a mean-field approximation; only the spatial averages of the time-dependent parameters are used in the calculations. Field propagation effects and the spatial variation of the coupling strength, for instance, are neglected in this model. These effects may alter the field pattern during pulse formation. The use of the constant cavity decay time means that only the average value of the cavity decay time is considered in the approximation. Effects arising from the temporal variations of the coupling strength and the field pattern are not taken into account at all. Therefore, the corresponding temporal variation of the cavity decay time has been totally ignored in this model. In fact, this is the most fundamental difference between this model and the more rigorous and more accurate semiclassical model. The effect resulting from the temporal variation of the cavity decay time is generally referred to as the self Q-switching effect. Hence, comparisons of the results generated by the two models may lead to some sensible evaluation of the influence of the self Q-switching effect on the pulse-forming process in DFDLs.

4.3 Comparisons with Other Theoretical Models

The general features of the computer solutions of the undercoupled DFDL model were shown to be very similar to those of the original rate equation model proposed by Bor (we shall refer to Bor's model as the overcoupled DFDL model). In this section, we shall compare the two models in more detail. Results from the semiclassical model of the DFDL [16] will also be used in some discussions. The parameters used in the calculations in this section are basically the same as those given in section 3.3 unless stated otherwise.

Figure 4.4a shows the dependence of the duration of the first pulse on the pumping rate. This is calculated with the undercoupled DFDL model. Figure 4.4b is the corresponding result calculated using Bor's overcoupled DFDL model. Apart from the absolute values of

Figure 4.4a First-pulse duration versus pumping rate

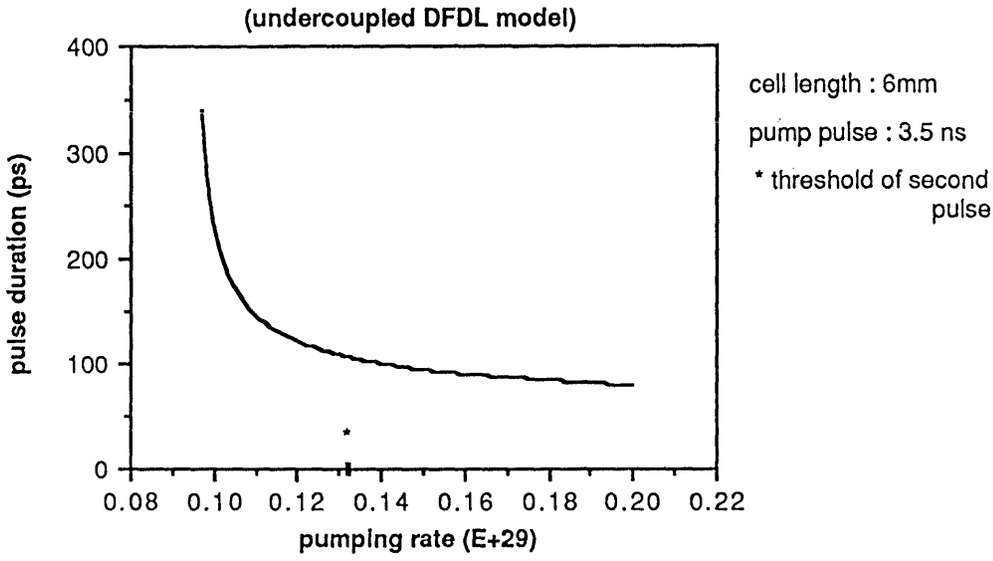


Figure 4.4b First-pulse duration versus pumping rate

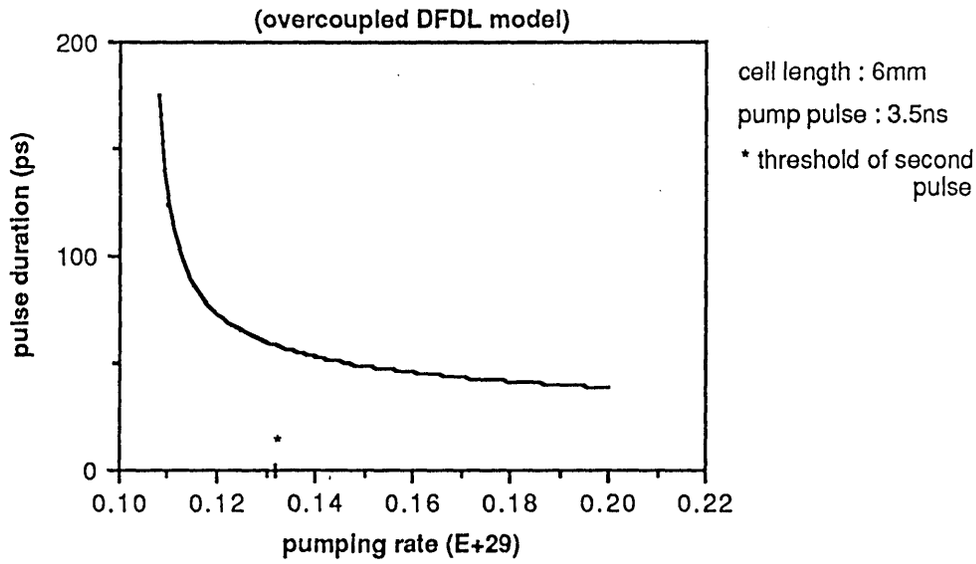


Figure 4.5a First-pulse energy versus pumping rate

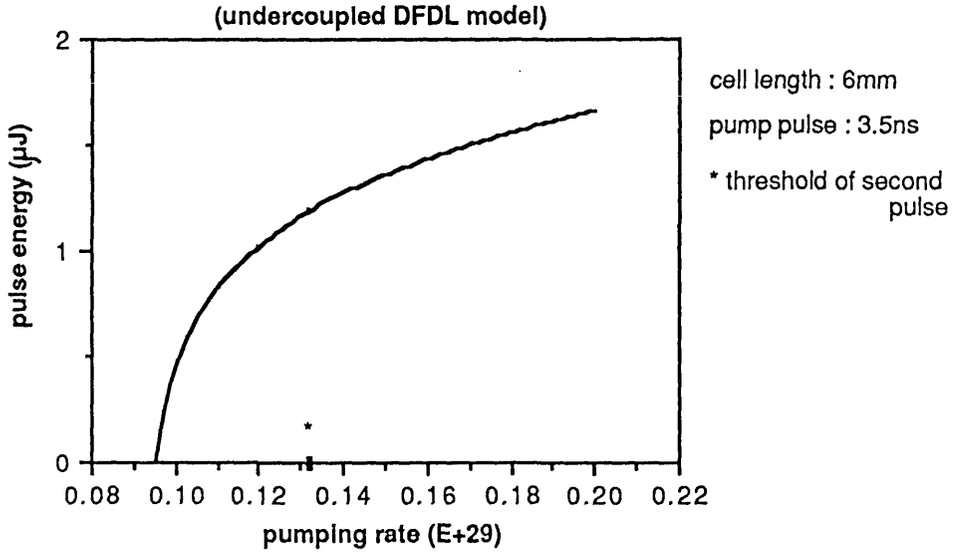


Figure 4.5b First-pulse energy versus pumping rate

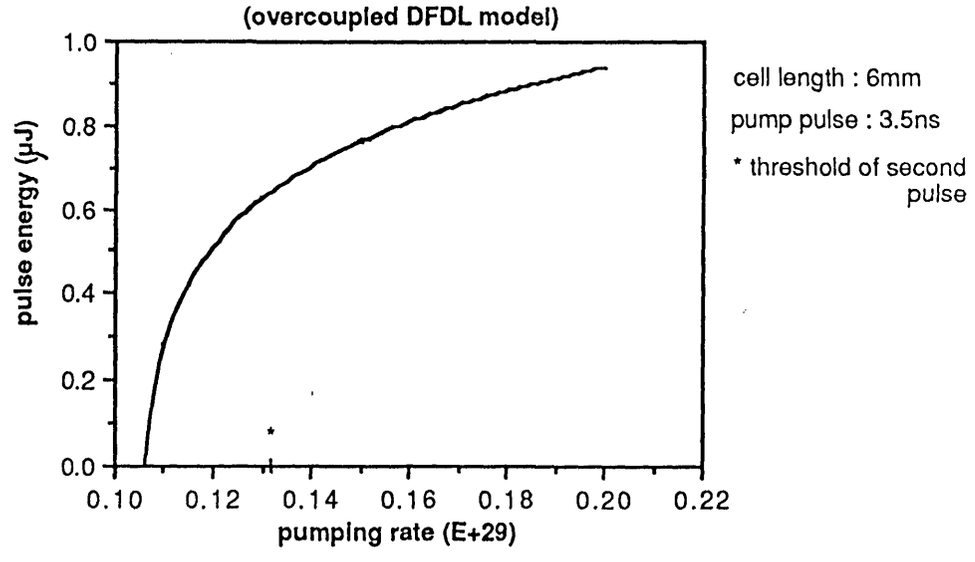
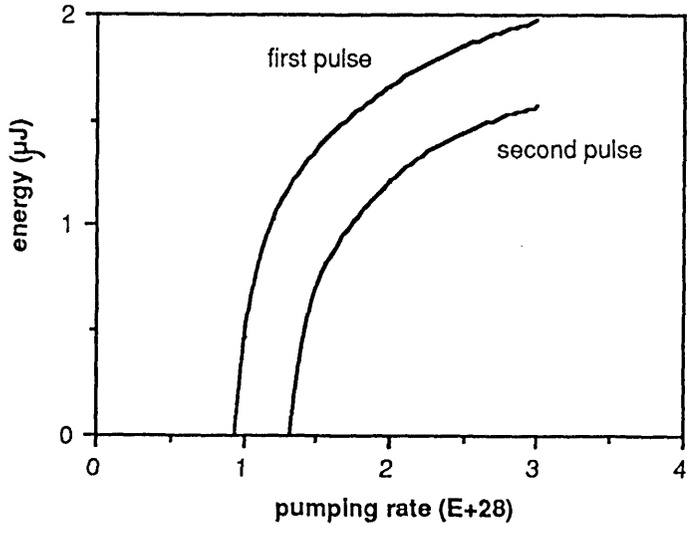


Figure 4.6 Dependence of pulse energy on pumping rate



pulse durations, the similarities are obvious. Figures 4.5a and 4.5b show the corresponding dependence of the energy of the first pulse on the pumping rate calculated from the undercoupled and overcoupled models, respectively. The sharpness of the threshold of the DFDL is clearly shown. The threshold of the second pulse is also marked by the symbol *. The range of pumping rate suitable for single-pulse operation is best illustrated in a diagram such as Figure 4.6. Clearly, the threshold of the second pulse is well defined. Hence the second-pulse threshold pumping rate can be used as the reference for defining the duration of the first pulse. This pulse duration, of course, corresponds to the minimum pulse duration under single-pulse operation. Comparisons between the first-pulse durations under different operating conditions will be based on this common reference.

It is well known that shorter DFDL pulses can be generated if the length of the laser device is decreased. The temporal characteristics of the first DFDL pulse for a shorter device length of 1 mm are shown in Figures 4.7a and 4.7b, which correspond to the calculations from the undercoupled DFDL model and the overcoupled DFDL model, respectively. Figures 4.8a and 4.8b show the corresponding energy characteristics. The durations of the first pulse, in each case, are indeed shorter than the corresponding values for the longer 6 mm device. However, the range of pumping rate for single-pulse operation (as a percentage of the second-pulse threshold value) is considerably narrower. Also the pumping required for laser oscillation is increased by a large factor.

The dependence of pulse duration on laser device length is better illustrated in Figure 4.9. The curve "C1" is calculated using our undercoupled DFDL model whereas the curve "C2" is computed from the overcoupled DFDL model. The discrete points on curve "E2" are extracted from the experimental results obtained by Bor [11]. It can be seen that despite the simplicity of the undercoupled approximation, this new model does show good qualitative agreement with experimental observations. At least, it gives a good first-order estimate of the temporal characteristics of the gain-coupled DFDL. More comparisons of experimental data with the predictions of this model will be presented later on.

We mentioned that the most fundamental difference between the undercoupled DFDL model and the more complete semiclassical model

Figure 4.7a First-pulse duration versus pumping rate

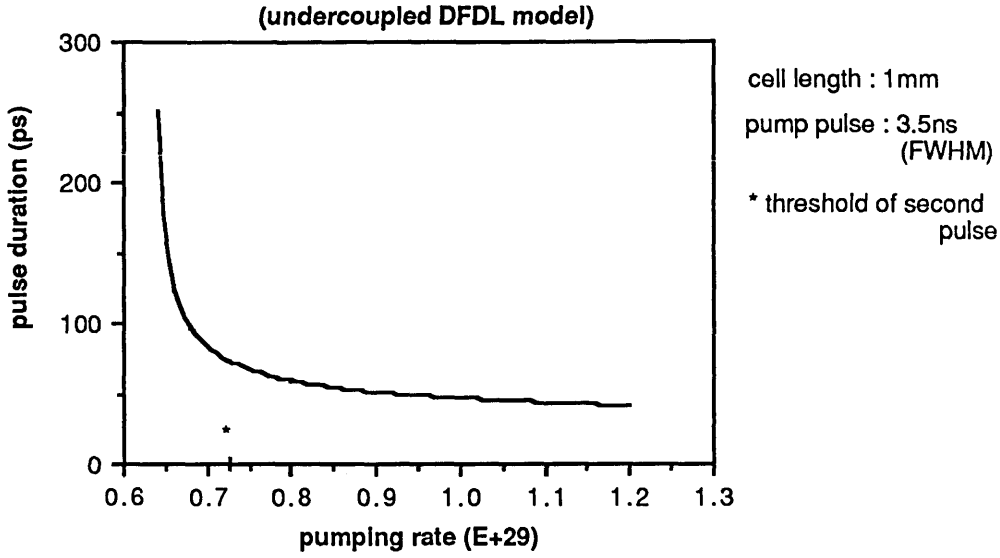


Figure 4.7b First-pulse duration versus pumping rate

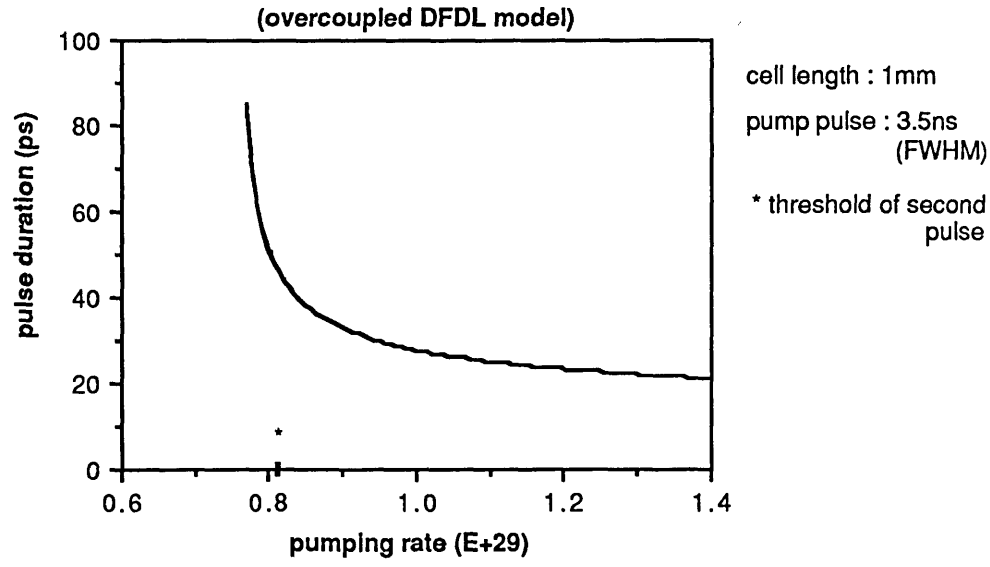


Figure 4.8a First-pulse energy versus pumping rate

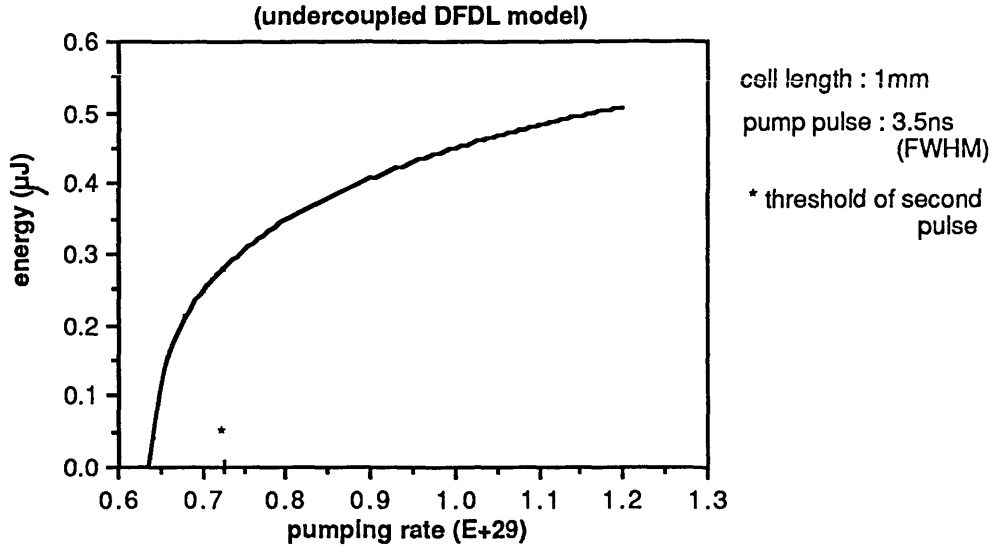


Figure 4.8b First-pulse energy versus pumping rate

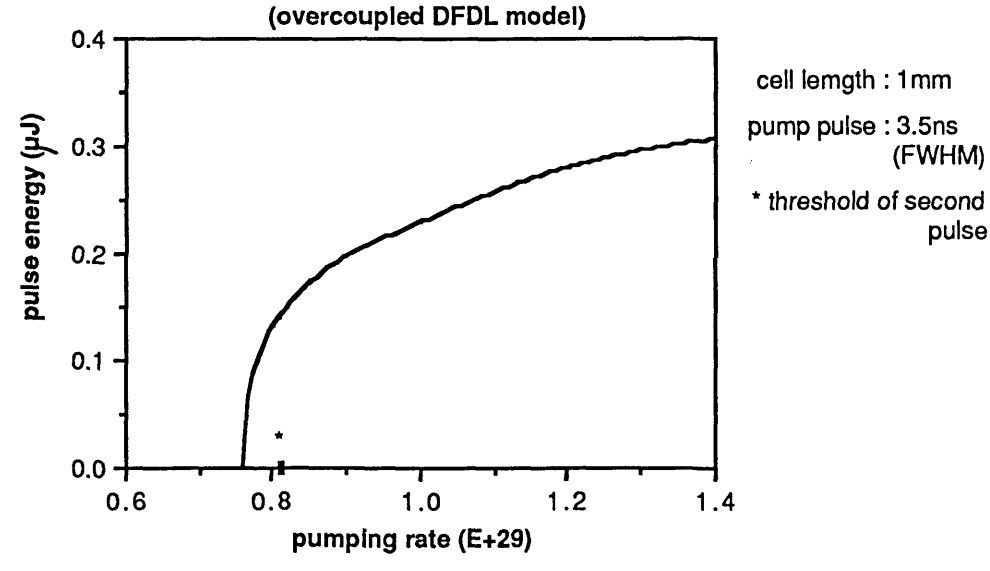
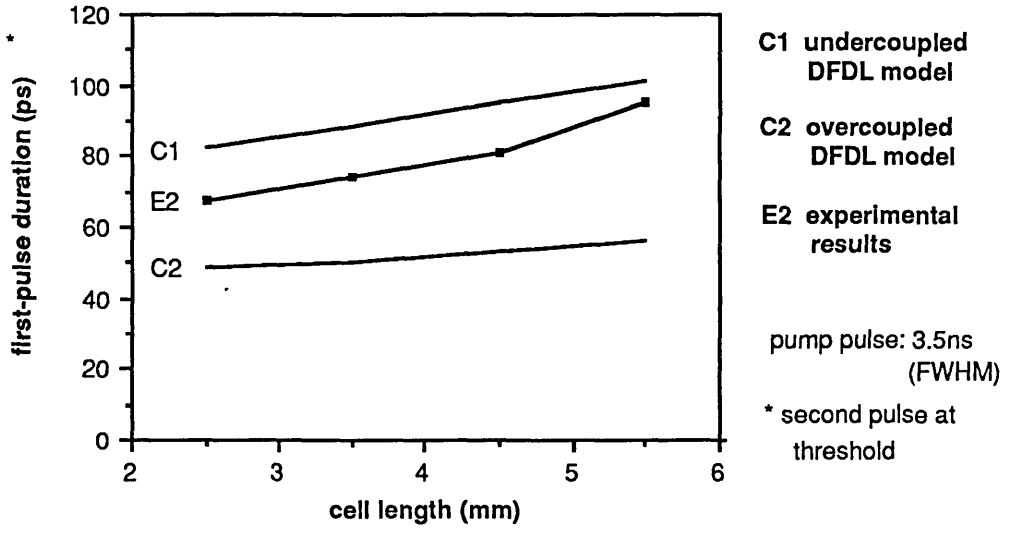


Figure 4.9 Pulse duration versus device length



[16] was that the self Q-switching effect was neglected in the former model. It is therefore interesting to compare the temporal characteristics calculated from the two models. Figure 4.10 illustrates some typical results. The curve "C1" was obtained from the undercoupled DFDL model whereas the curve "C2" was extracted from the semiclassical model results of Duling III and Raymer [16]. The difference between the two curves should give some reasonable estimates of the self Q-switching effect on the pulse duration of a typical DFDL. Obviously, the self Q-switching effect does give rise to shorter pulses. However, the contribution to pulse shortening due to this effect may not be as large as it was often believed to be. Other factors may be just as important. For instance, the absolute average value of the cavity decay time may play a major role in the formation of short pulses.

The dependence of pulse duration on the magnitude of the cavity decay time has been investigated using the undercoupled model. By varying arbitrarily the value of the constant cavity decay time, the corresponding duration of the first DFDL pulse is determined (at second-pulse threshold). Figure 4.11 summarizes the results. The importance of the absolute magnitude of the cavity decay time cannot be ignored.

One of the shortcomings of Bor's rate equation model, as pointed out by Duling III and Raymer [16] was its failure in predicting the pulse duration of the DFDL pulses when the pump pulse duration is approaching the cavity transit time. The semiclassical theory developed by Duling III and Raymer, on the other hand, should work well in this regime. It should be interesting to compare the results of the undercoupled DFDL model and those of the other theoretical models.

We shall, first of all, present some results from the undercoupled DFDL model. Figures 4.12a and 4.12b are the computer simulations of the generation of single DFDL pulses with a short duration pump pulse having a duration of 70 ps (FWHM). The laser device lengths are 1 mm and 4 mm, respectively. Otherwise, the parameters used in the calculations are the same as those given in section 3.3.

Figure 4.13 shows the dependence of the duration of the first pulse on the pumping rate for the 1 mm laser. Figure 4.14 shows the corresponding energy dependency. The general features of these

Figure 4.10 Theoretical dependence of pulse duration on device length

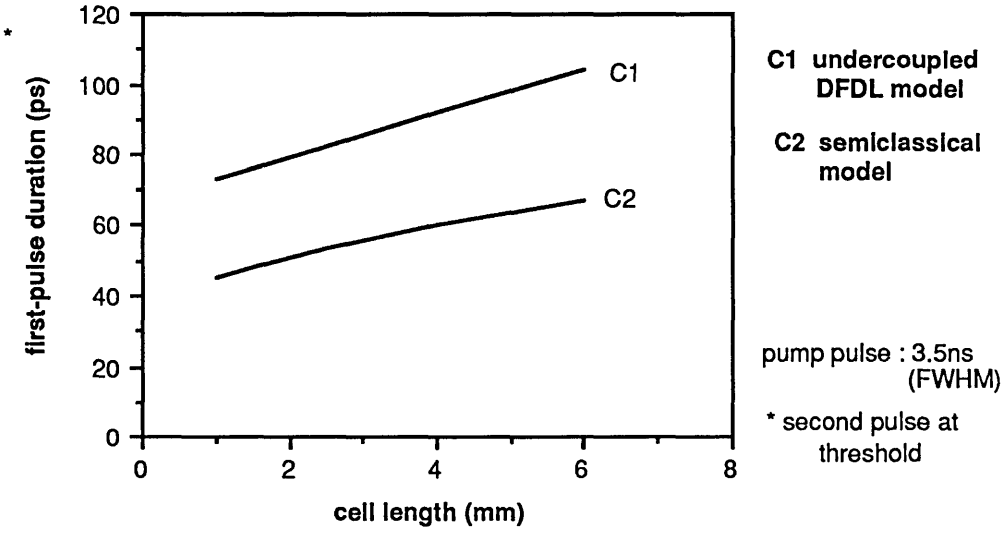
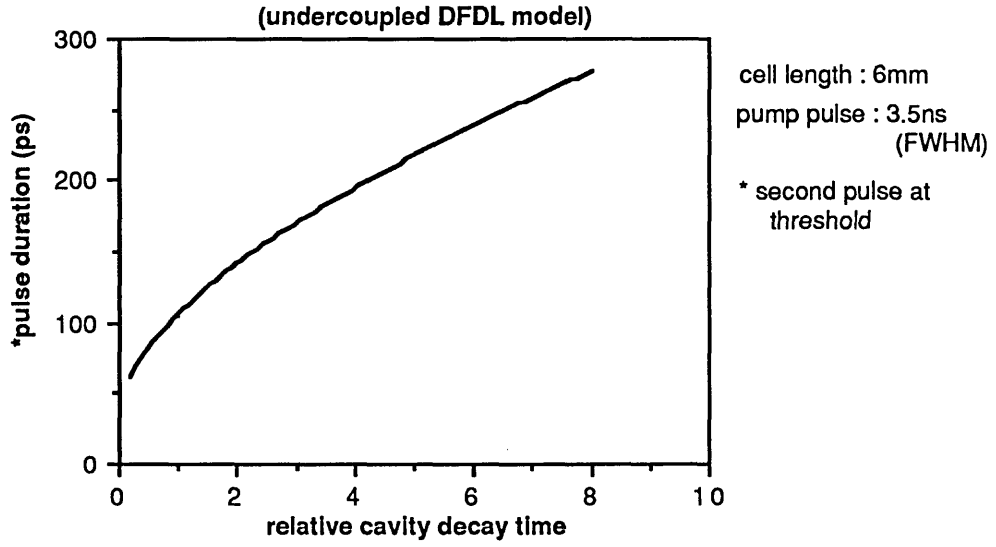


Figure 4.11 First-pulse duration versus cavity lifetime



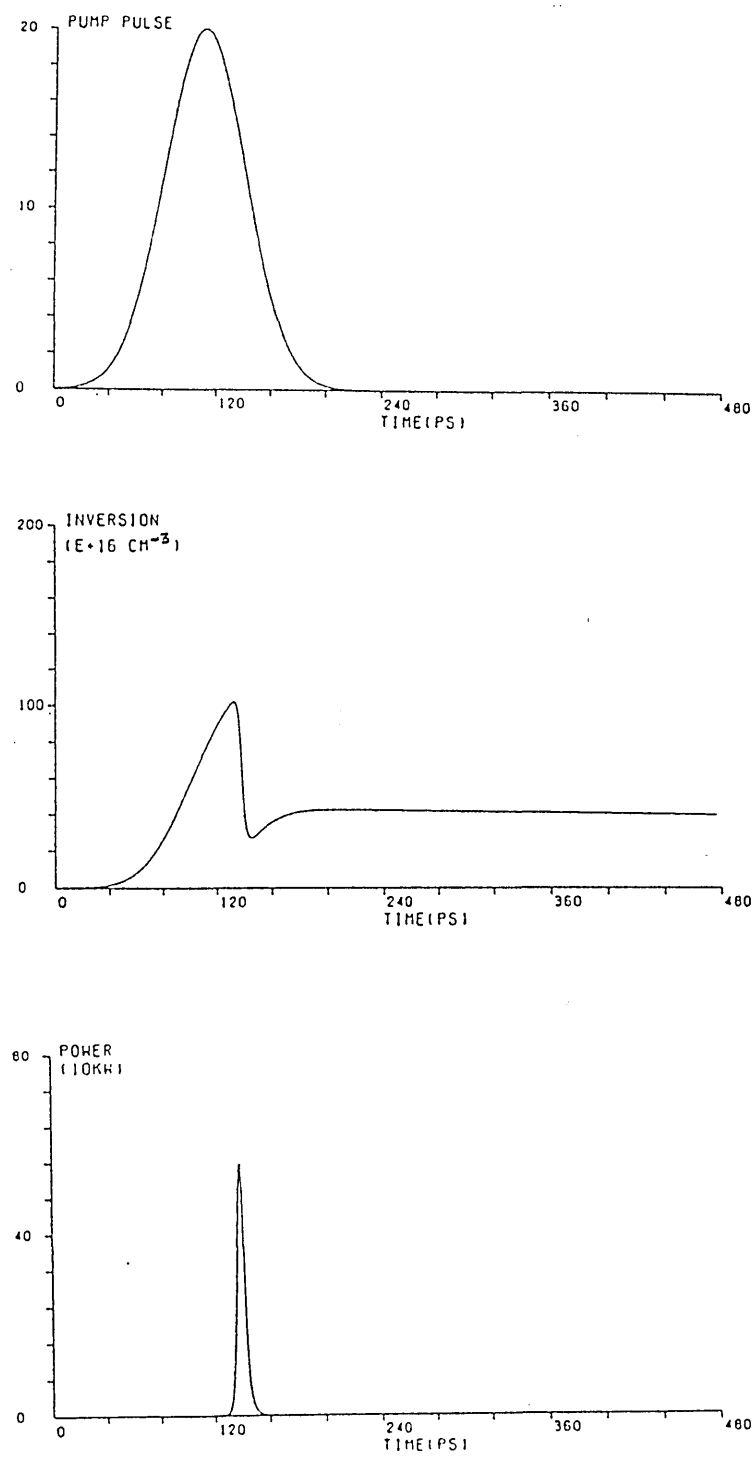


Figure 4.12a. Generation of single DFDL pulse with a short pump pulse (device length: 1 mm).

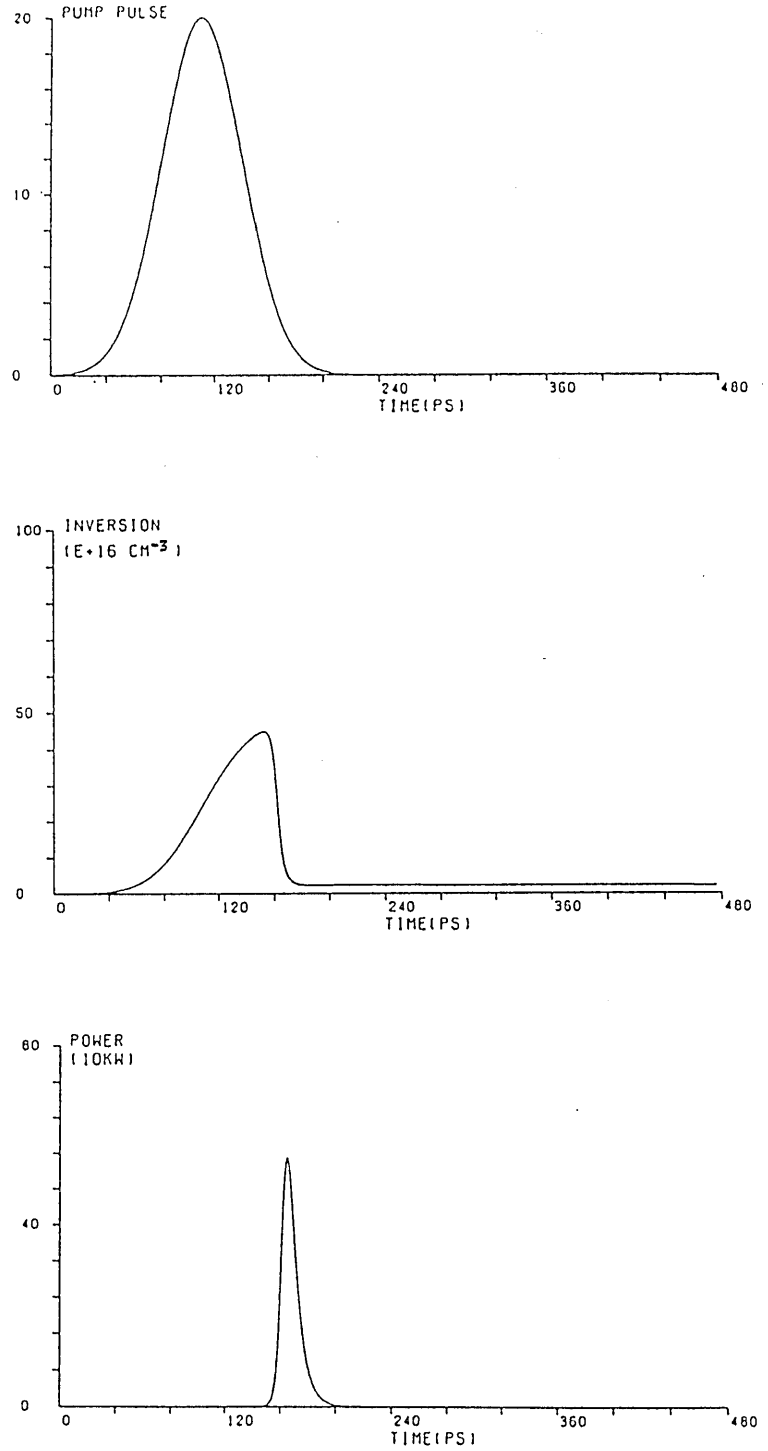


Figure 4.12b. Generation of single DFDL pulse with a short pump pulse (device length: 4 mm).

Figure 4.13 First-pulse duration versus pumping rate

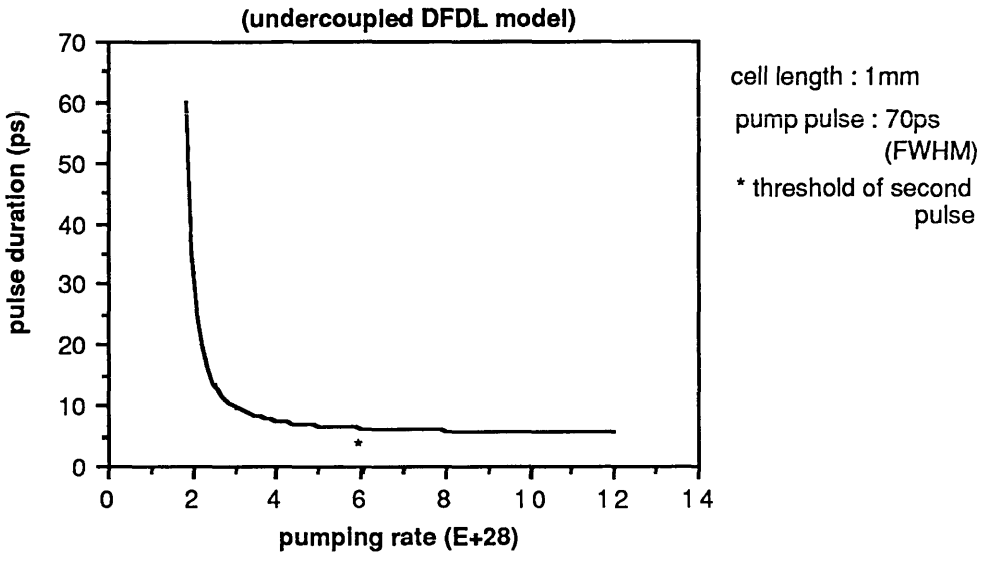
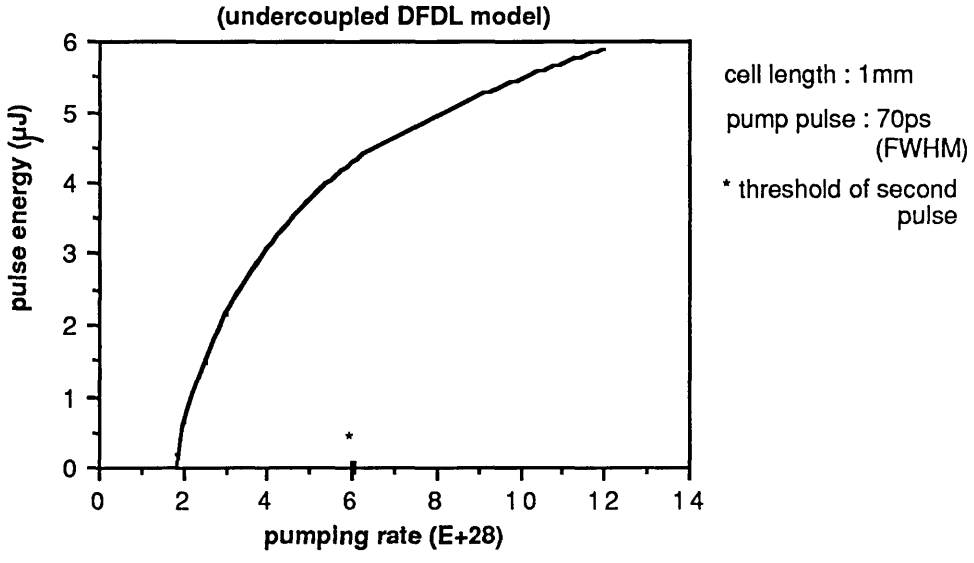


Figure 4.14 First-pulse energy versus pumping rate

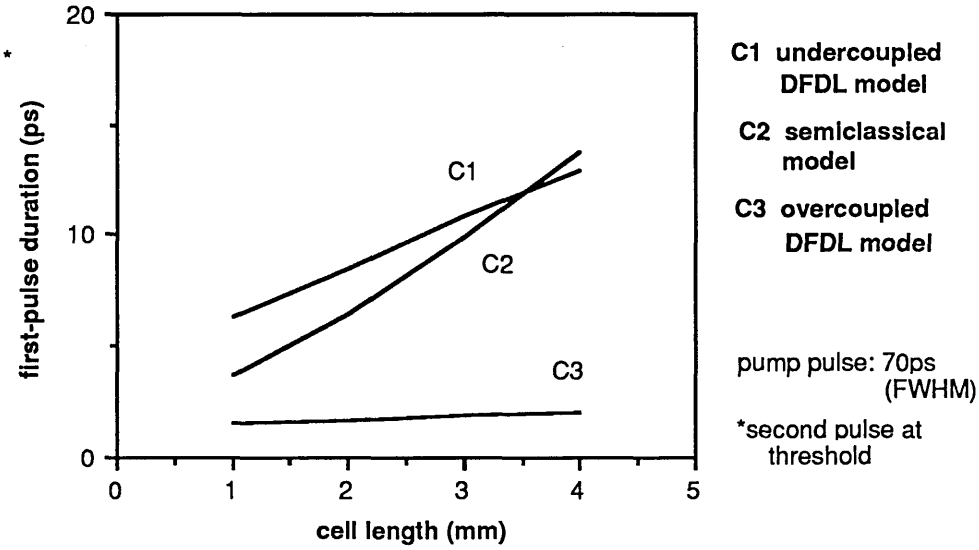


curves are similar to those of Figures 4.7a and 4.7b for which the corresponding pump-pulse duration is much longer. As expected, shorter duration DFDL pulses are produced with a shorter pump pulse. Moreover, there are a few more practical advantages of using shorter duration pump pulse for single-pulse operation. Firstly, the range of pumping rate suitable for single-pulse operation is very much wider. Secondly, over a large part of this range, the durations of the first pulse are quite stable. Hence it is much easier to obtain short and stable single pulses. These results are consistent with the theoretical predictions from the semiclassical model [16].

By considering the dependence of the duration of the first pulse as a function of the length of the DFDL for the case of a short duration pump pulse, Duling III and Raymer pointed out the discrepancy between their semiclassical model and Bor's overcoupled DFDL model, which failed completely as the cavity transit time was approaching the pump pulse duration. It is therefore interesting to bring in the results from the undercoupled DFDL model for comparison. Figure 4.15 shows the results from the three different models. The curve "C1" is calculated from the undercoupled DFDL model. The curve "C2" is extracted from the results of the semiclassical model [16] and the curve "C3" is the corresponding result calculated from Bor's overcoupled DFDL model. The discrepancy between Bor's model and the semiclassical model is evident. The undercoupled DFDL model, on the other hand, still gives reasonable estimation on the duration of the first pulse.

Some important limitations on the undercoupled DFDL model in the regime of short pump pulse should be noted. Although the undercoupled field pattern is a reasonable approximation in the vicinity of pulse formation, the use of a constant cavity decay time will affect the dumping rate of cavity photons at the tail of the first pulse. Although, within our assumptions, this does not seriously affect the duration of the first pulse, it does lead to an over-estimation of the number of cavity photons at the end of the first pulse and therefore affects the temporal structure of the second pulse and the other oncoming pulses. This is particularly serious for the cases of high pumping rate and short duration pump pulse. The temporal structure of the DFDL pulses may suffer from distortion. Instead of two discrete pulses, the computer simulation may give a picture of two pulses beginning to merge together (Figure

Figure 4.15 Pulse duration versus device length



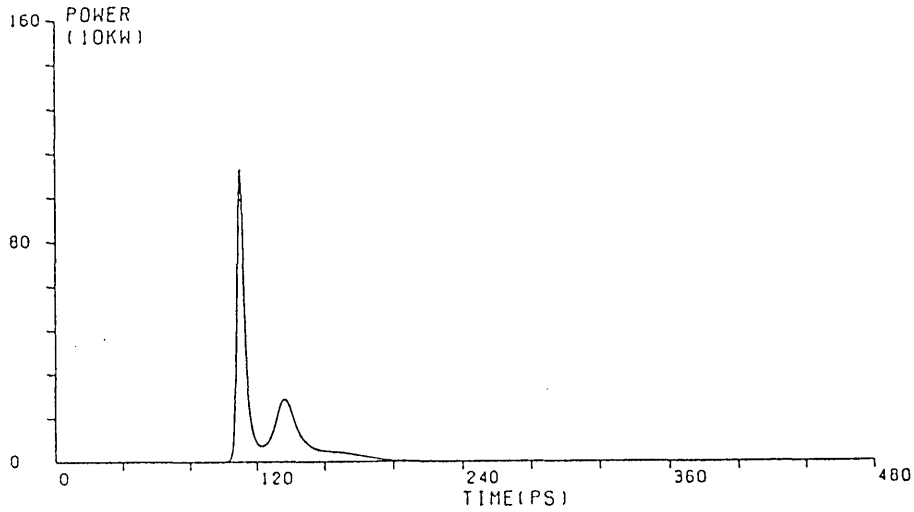


Figure 4.16a. A computer-generated multiple-pulse profile from the undercoupled DFDL model (short pump pulse). (L = 1 mm).

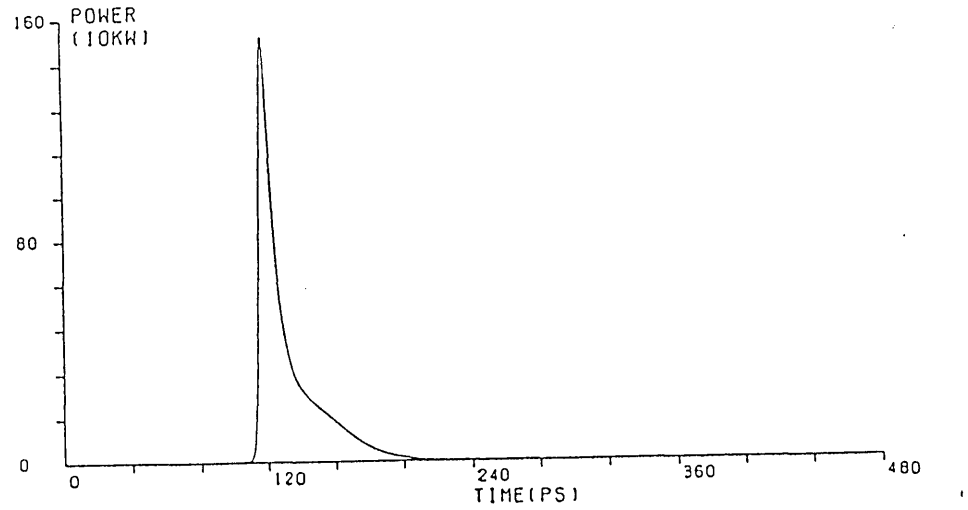
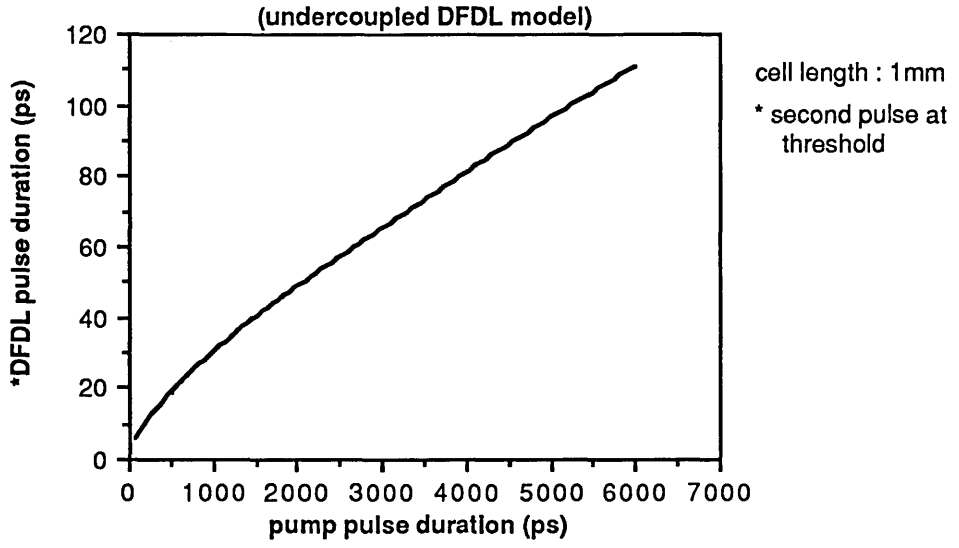


Figure 4.16b. A computer-generated temporal profile from the undercoupled DFDL model (short pump pulse). (L = 4 mm).

Figure 4.17 First-pulse duration versus pump pulse duration



4.16a). The distortion can become very serious if the pumping rate is high and the laser device length is long. The "second pulse", for instance, may merge completely with the first pulse to give an appearance of a strange-looking single pulse (Figure 4.16b). This undercoupled model obviously cannot be used to simulate multiple-pulse operation in the short pump pulse regime. Nevertheless, as we have shown, this model should remain a good first-order approximation for determining the pulse duration under the single-pulse operation conditions.

As discussed above, shorter DFDL single pulses are produced if the duration of the pump-pulse is short. This dependency of DFDL pulse-width on the pump pulse duration has been investigated more thoroughly using the undercoupled DFDL model. The results are summarized in Figure 4.17. The advantage of using a short pump pulse to generate short DFDL pulses is clearly shown.

Although shorter pulses can be produced using a shorter duration pump pulse, such a pulse may not, however, be readily available in practice. For example, in the experimental laser system to be described in the next chapters, the duration of the pump pulse is about five to six nanoseconds. It is therefore useful to consider the temporal and energy characteristics for this experimental condition. We shall set the duration of the pump pulse at 5 ns and the device length at 5 mm. Otherwise, the parameters used for the following calculations are the same as those given in section 3.3. Figures 4.18a and 4.18b, which show the dependence of the pulse duration on the pumping rate, are the theoretical results from the undercoupled DFDL model and the overcoupled DFDL model, respectively. Figures 4.19a and 4.19b show the corresponding energy dependence.

It is sometimes useful to know the effect of varying a particular parameter on the pulse duration of the DFDL. Some results of these studies are presented below. Again, we use both the undercoupled DFDL model and the overcoupled DFDL model in the investigations. Figures 4.20a and 4.20b show the effect of the upper-state lifetime on the pulse duration of the first pulse. Figures 4.21a and 4.21b show the dependence of the pulse duration on the refractive index of the dye solvent. In the rate equation models, the number of initial cavity noise-photons is estimated by approximating a stationary initial condition. It is interesting to see how the pulse duration and the required pumping rate for single-pulse operation are affected

Figure 4.18a First-pulse duration versus pumping rate

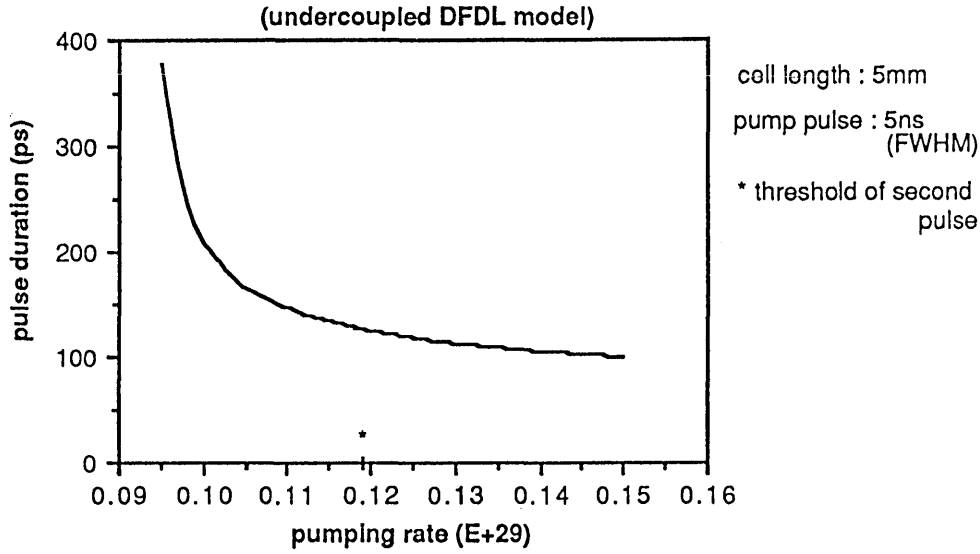


Figure 4.18b First-pulse duration versus pumping rate

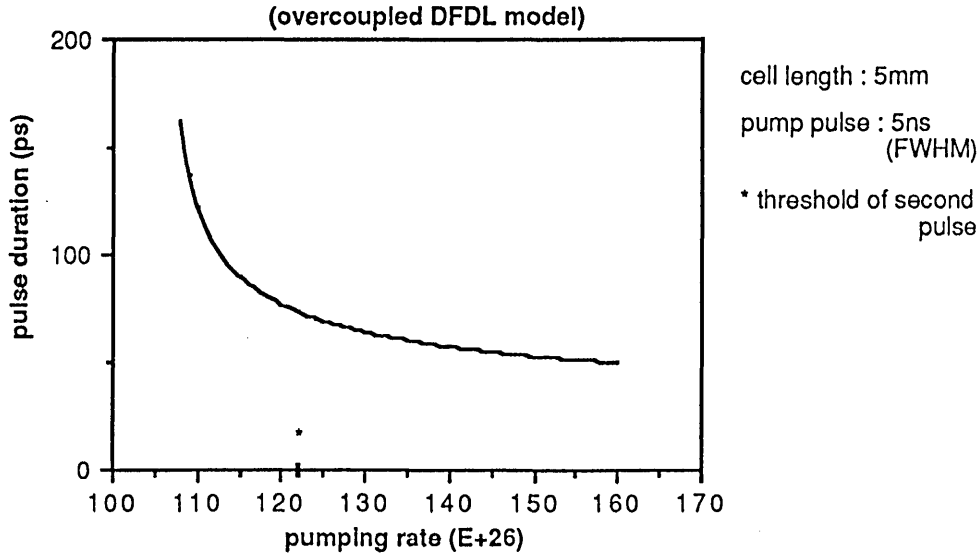


Figure 4.19a First-pulse energy versus pumping rate

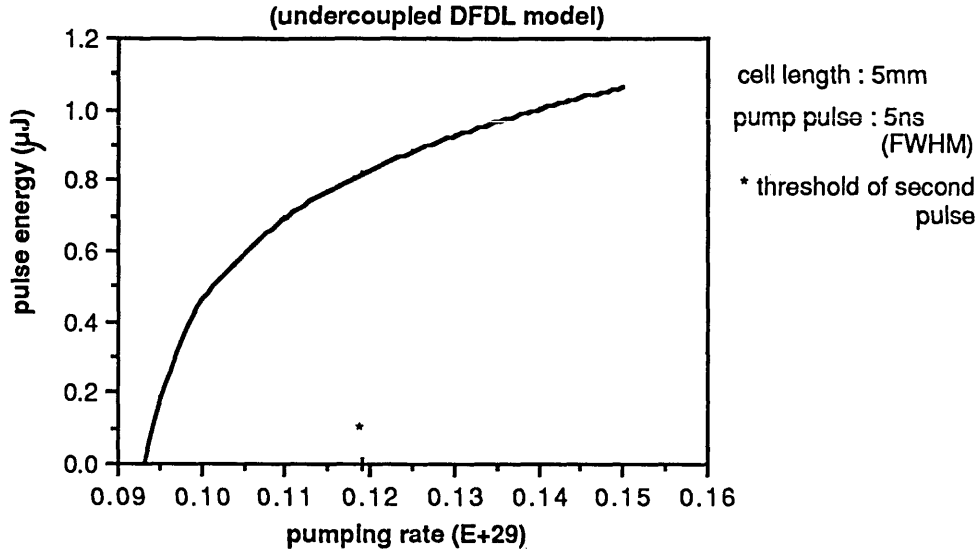


Figure 4.19b First-pulse energy versus pumping rate

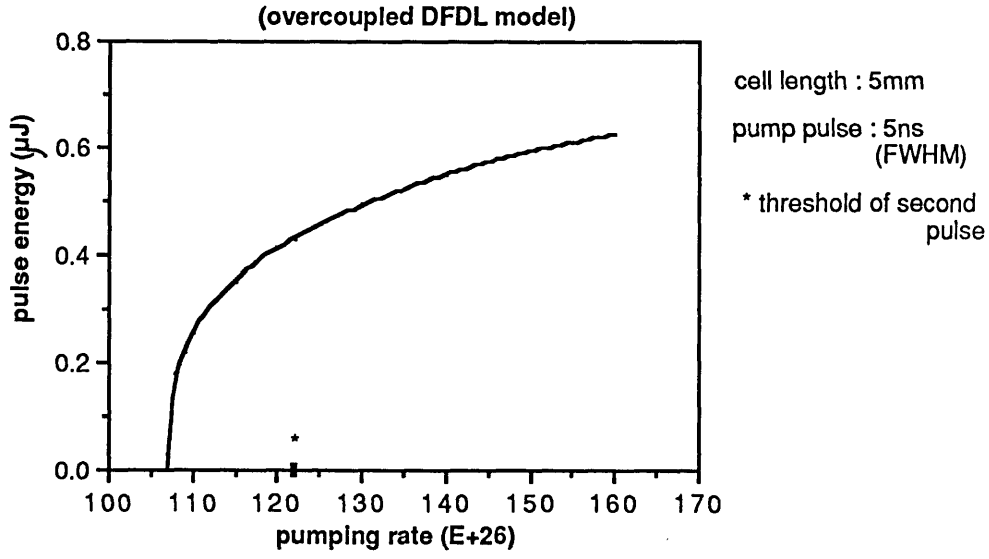


Figure 4.20a Effect of upper-state lifetime on pulse duration

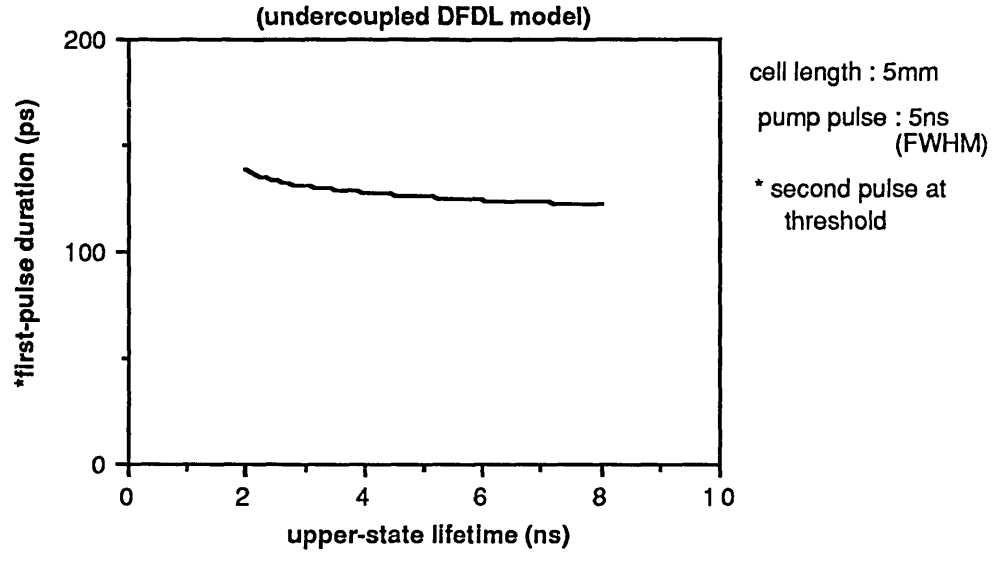


Figure 4.20b Effect of upper-state lifetime on pulse duration

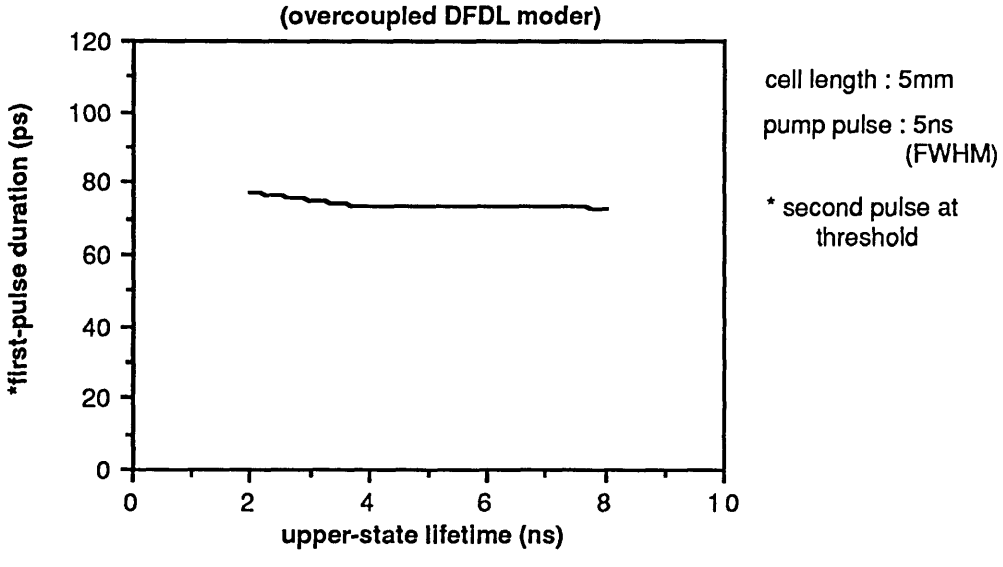


Figure 4.21a Effect of solvent refractive index on pulse duration

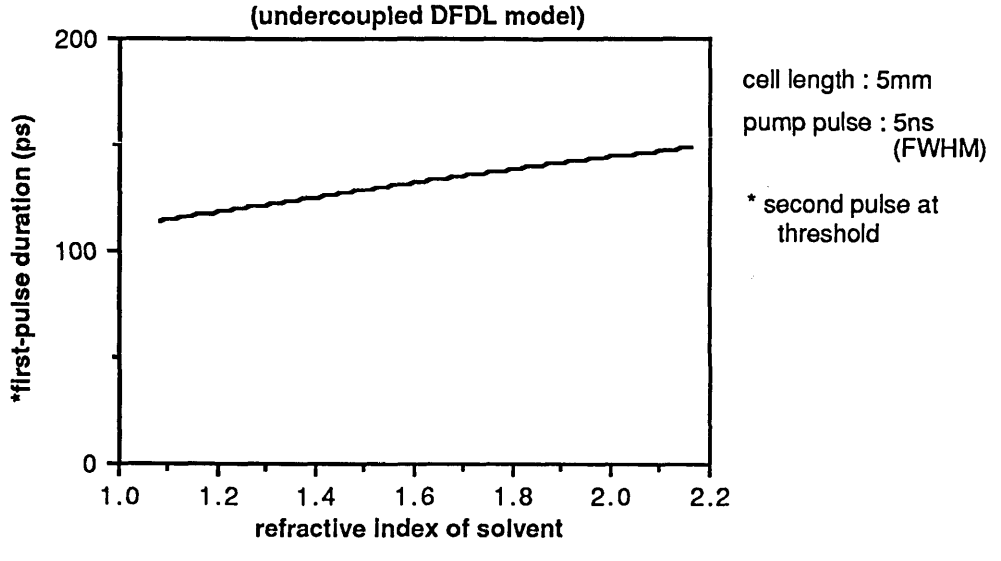


Figure 4.21b Effect of solvent refractive index on pulse duration

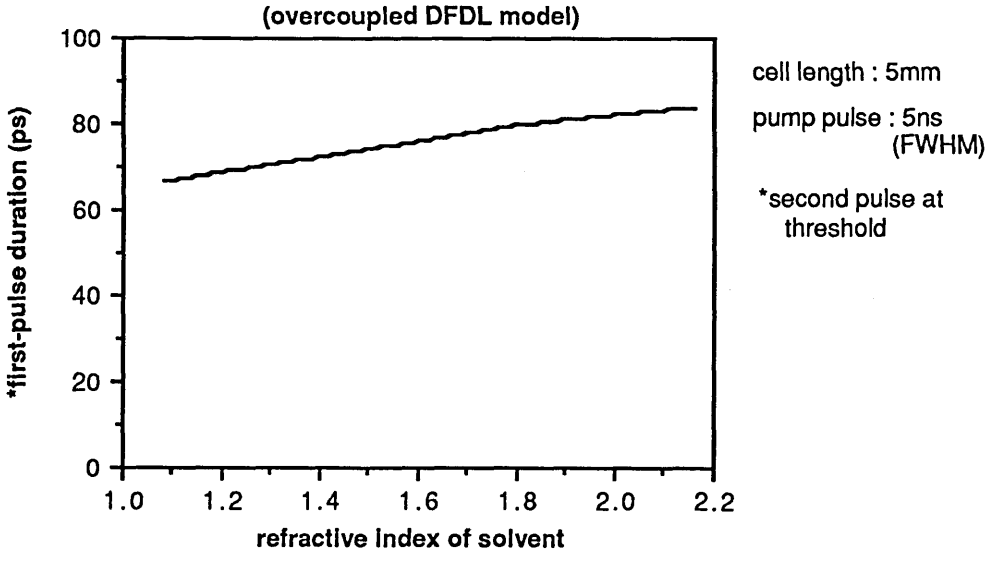


Figure 4.22a Effects of initial noise-photon number

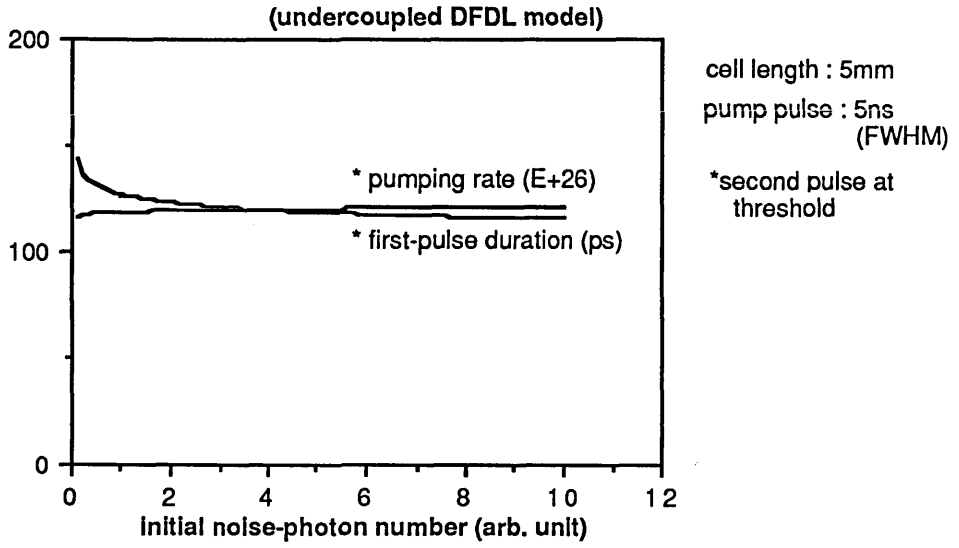
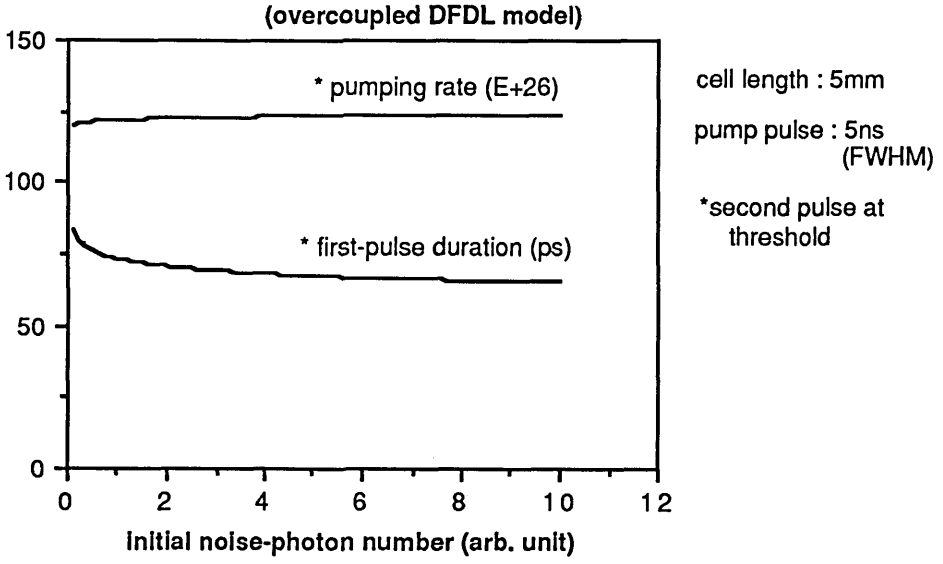


Figure 4.22b Effects of initial noise-photon number



if the initial noise-photon number is varied. Figures 4.22a and 4.22b illustrate these effects. The curves are calculated for a range of initial photon numbers over two orders of magnitude.

As shown above, the general features of the results from the undercoupled DFDL model were very similar to those obtained using the overcoupled DFDL model first developed by Bor. Despite the inappropriate assumptions made in the derivation of the equivalent cavity decay time in Bor's model (see section 3.5), the results predicted from this overcoupled DFDL model seemed to fit the experimental data quite well. A close examination of the fundamental similarities between the two rate equation models may provide some clues to the reason why Bor's model can give good approximate results.

We have shown that the magnitude of the cavity decay time in these rate equation models has a strong influence on the DFDL pulse duration. The constant cavity decay time used in the undercoupled DFDL model has been derived from the steady-state coupled-wave theory and its magnitude should be a good approximation to the average time a photon spends inside the laser cavity. The mean value of the time-dependent equivalent cavity decay time (during pulse formation) in Bor's overcoupled model is in fact very close to the value of the constant cavity decay time in the undercoupled DFDL model. It is therefore expected that the results generated from the two models would be very close.

But the undercoupled DFDL model neglects the effect due to the varying nature of the cavity decay time whereas in Bor's overcoupled DFDL model the equivalent cavity decay time is a rapidly changing quantity in the vicinity of pulse formation. Hence Bor's model does contain some features which can simulate the varying Bragg reflectivity effect. Therefore, the overcoupled DFDL model could sometimes give better computer simulations than the undercoupled DFDL model. Comparisons of the results from the theoretical models suggest that this self Q-switching effect may well give rise to a further pulse shortening of around 40% in the case of a long duration pump pulse being used.

The undercoupled DFDL model has been shown to give fairly good first-order approximation to the laser output characteristics under various conditions. The absolute magnitude of the average cavity decay time was found to play an important role in the process of

short pulse formation in DFDLs. By comparing this model with the more complete semiclassical model, it was deduced that the self Q-switching effect could shorten the pulse duration further by another factor of about two.

One of the major features of the undercoupled DFDL model is its simplicity. In the next section, we shall use this simple model to analyse some basic characteristics of the DFDL pulses. As we shall see, the results of some simple analysis agree very well with the calculations from full numerical computations. Some of these results will also be compared with available experimental data; good qualitative agreement has been found.

4.4 Characteristics of DFDL Pulses

The undercoupled DFDL model has been shown to give reasonably good first-order approximations. It is, however, only an approximate model and cannot match a more complete theory such as the semi-classical model. Nevertheless, the simplicity of this model can be exploited to yield simple analytic expressions which may give some clues to the underlying physical mechanism for the formation of short pulses in the DFDL. These expressions will be compared with the full numerical computational results. Qualitative agreement between some of the analytic expressions and experimental results has also been found. However, it should be noted that this analysis is valid only in the regime of long-duration pump pulse.

In our undercoupled DFDL model, the cavity decay time is assumed to be a constant. The resulting rate equations are, in fact, equivalent to the coupled rate equations for relaxation oscillations. Hence the results for the undercoupled DFDL model should be relevant to relaxation oscillations under the appropriate conditions.

The computer simulations from Bor's original rate equation model suggest that the formation of short pulses is due to the rapid variation of the value of the equivalent cavity decay time in the vicinity of pulse formation. This seems reasonable if we consider a diagram such as Figure 4.23. Apparently, the pulse is formed when the equivalent cavity decay time drops. However, a similar diagram (Figure 4.24) can also be generated in the undercoupled DFDL model. In this case, it is shown that the pulse is formed when the

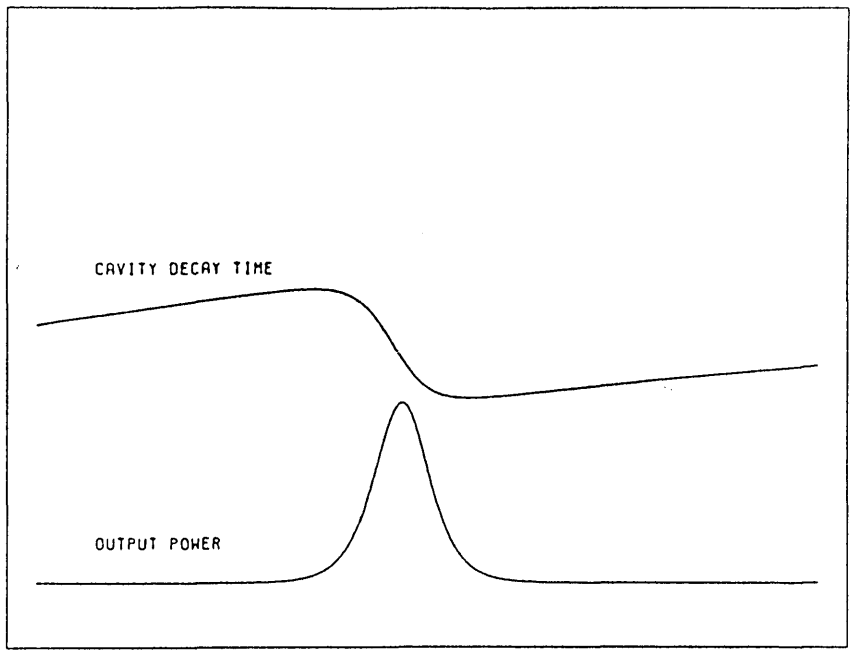


Figure 4.23. The formation of an ultrashort pulse in a DFDL (overcoupled DFDL model).

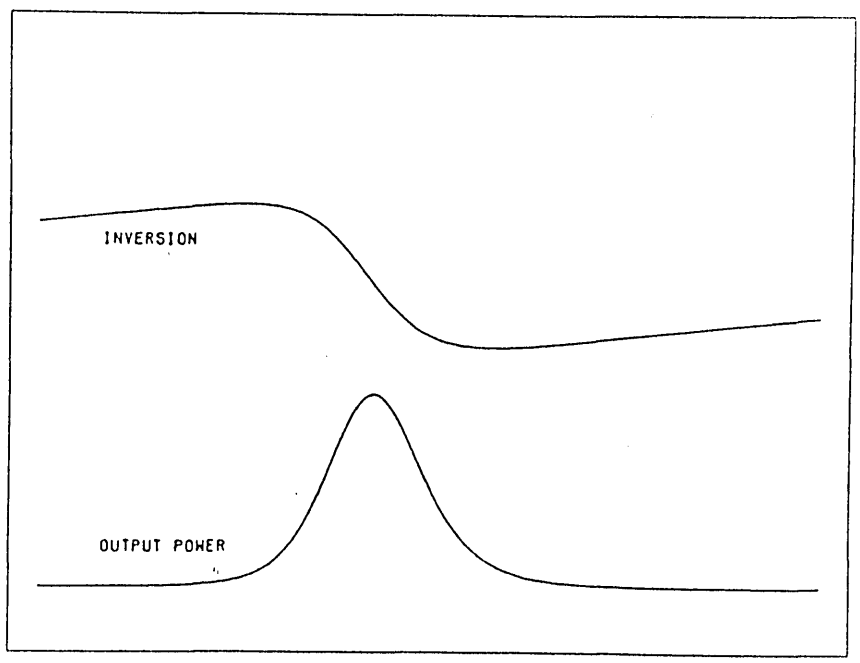


Figure 4.24. The formation of an ultrashort pulse in a DFDL (undercoupled DFDL model).

population inversion drops while the cavity decay time has remained constant throughout. It is therefore reasonable as a first-order approximation to treat the process of pulse formation as the interaction of the cavity photons and the population inversion in a laser cavity with a constant Q factor. This is the basis of the following rate equation analysis. It will be shown that with slight modification, the general results are applicable to Bor's overcoupled DFDL model as well. This shows that the most basic mechanism of pulse formation can be adequately described within the simple undercoupled DFDL model and the self Q-switching effect can be treated separately as a second-order correction.

In our undercoupled DFDL model, the coupled rate equations are given by

$$\frac{dn}{dt} = I_p \sigma_p (N - n) - \frac{\sigma_e c}{\eta} nq - \frac{n}{\tau}, \tag{4.9}$$

$$\frac{dq}{dt} = \frac{(\sigma_e - \sigma_a)c}{\eta} nq - \frac{q}{\tau_{cu}} + \frac{\Omega n}{\tau} . \tag{4.10}$$

These equations are the same as equations (3.1) and (3.2) except that the equivalent cavity decay time τ_c is now replaced by the constant cavity decay time τ_{cu}. The meanings of the other symbols are the same as those given in section 3.3.

In the vicinity of pulse formation, spontaneous emission may be neglected; the simplified rate equations become

$$\frac{dn}{dt} = I_p \sigma_p (N - n) - \frac{\sigma_e c}{\eta} nq, \tag{4.11}$$

$$\frac{dq}{dt} = \frac{(\sigma_e - \sigma_a)c}{\eta} nq - \frac{q}{\tau_{cu}} . \tag{4.12}$$

During pulse formation, the system experiences gain and the intensity of the output pulse continues to increase so long as the population inversion is above the steady-state threshold value. And when the population inversion drops to this value, the intensity of the output pulse stops growing; this is the peak of the output pulse. The time when this occurs will be taken as "time zero" ($t = 0$). Hence, when $t = 0$, $n = n_0$ and $\left.\frac{dq}{dt}\right|_{t_0} = 0$, where n_0 is the threshold inversion and t_0 denotes the value at $t = 0$. Putting these into equation (4.12)

yields

$$\frac{(\sigma_e - \sigma_a)c}{\eta} = \frac{1}{n_0 \tau_{cu}} \tag{4.13}$$

This equation can be put back into equation (4.12) to give an alternative version of the cavity photon equation:

$$\frac{dq}{dt} = \left[\frac{n}{n_0} - 1\right] \frac{q}{\tau_{cu}} . \tag{4.14}$$

In the vicinity of pulse formation, the population inversion may be written as

$$n(t) = n_0 - k_n t, \tag{4.15}$$

where k_n is the rate of depletion of the inverted population. We note that the value of k_n varies very slowly for most of the time during pulse formation. Therefore, the value of k_n is assumed to be constant. This is a fair assumption to make so far as the following analysis is concerned. Substitution of equation (4.15) into equation (4.14) gives

$$\frac{dq}{dt} = \left[-\frac{k_n t}{n_0 \tau_{cu}}\right] q. \tag{4.16}$$

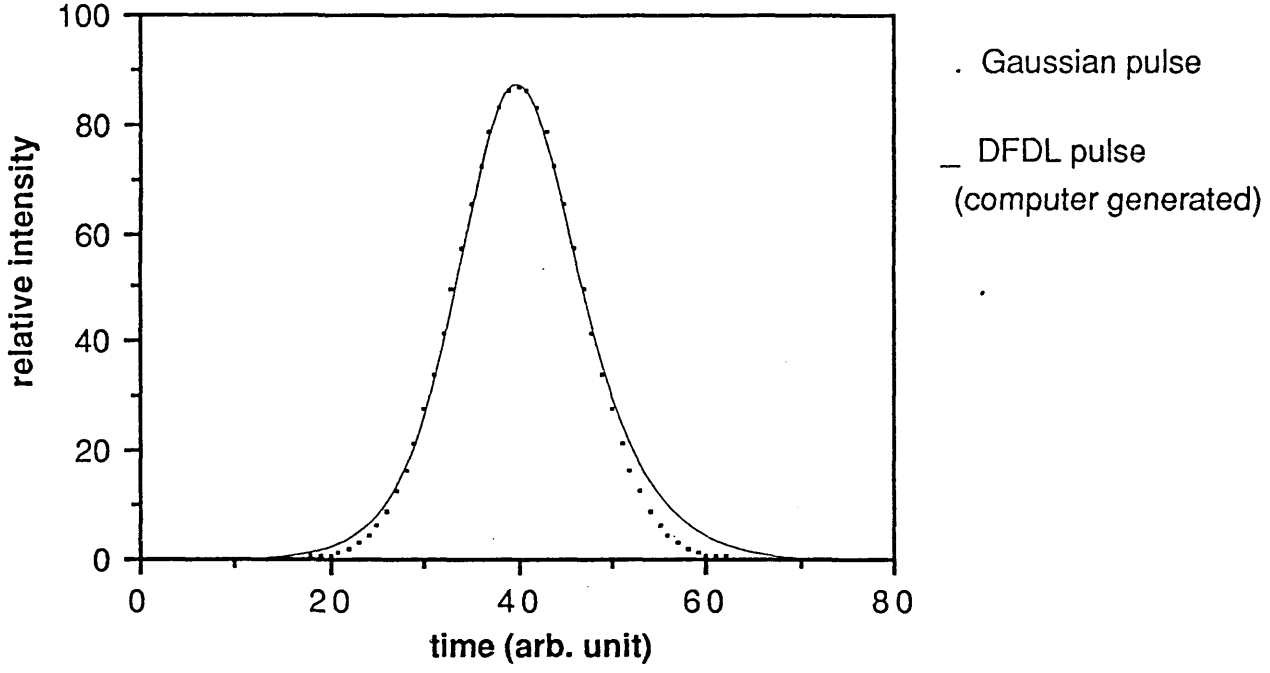
Integration gives

$$q(t) = q_0 \exp\left[-\frac{k_n}{2n_0 \tau_{cu}} t^2\right] , \tag{4.17}$$

where q_0 corresponds to the peak of the pulse centred at $t = 0$. Since the output intensity is directly proportional to the number of cavity photons, the DFDL pulse is therefore expected to have a profile very close to that of a Gaussian pulse as described by equation (4.17). Figure 4.25 is a comparison between the Gaussian pulse and the DFDL pulse profile generated with the full numerical calculation by the computer. The two profiles are basically very close to each other.

Figure 4.26 is a microdensitometer plot of a streak camera trace of a DFDL pulse obtained in our experiment at Imperial College. The

Figure 4.25 Comparision of computed DFDL pulse and Gaussian pulse profiles



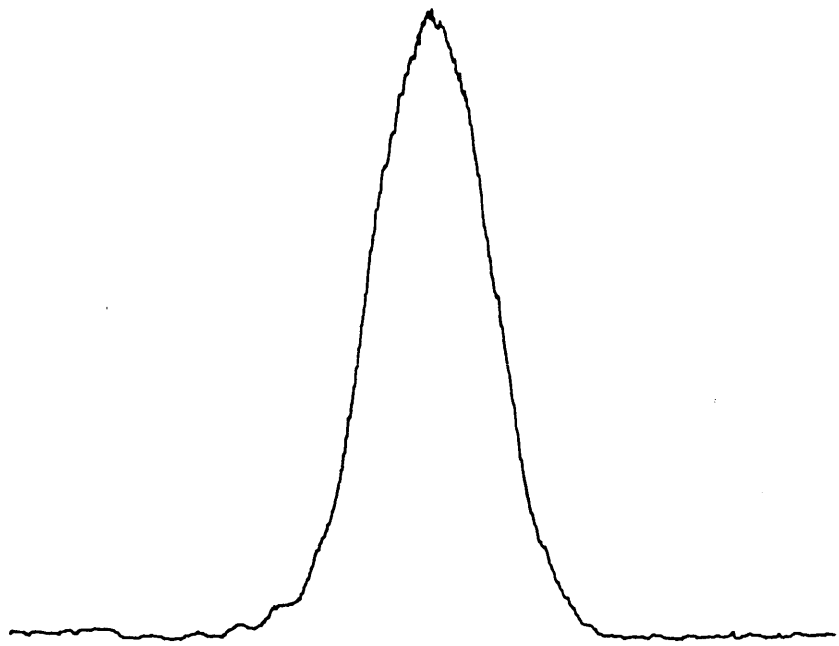
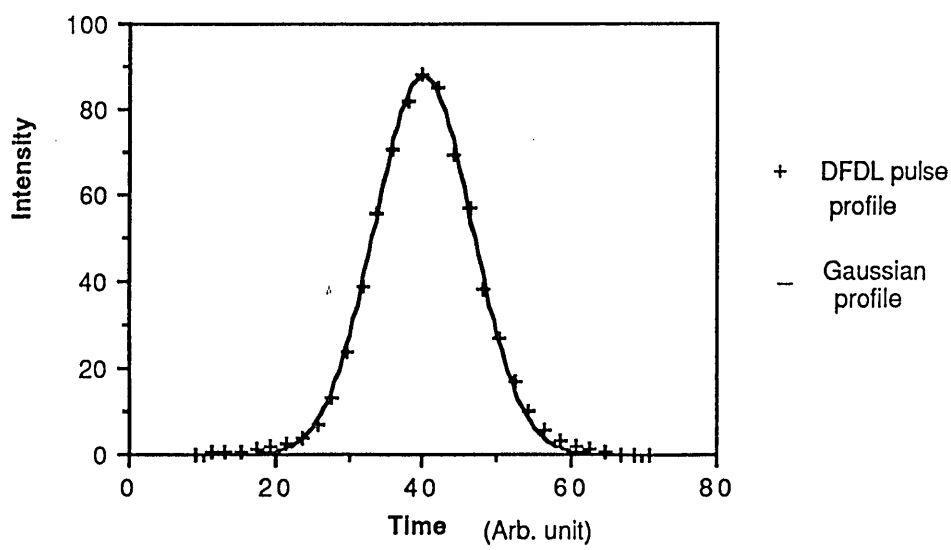


Figure 4.26. Microdensitometer plot of a DFDL pulse profile obtained with a streak camera.

Figure 4.27 Comparision of Gaussian and DFDL pulse profiles



vertical scale, which represents the intensity, is logarithmic. The corresponding linear plot of the DFDL pulse profile is compared with the Gaussian pulse in Figure 4.27. They are obviously very similar. In particular, there is very little difference at the top half of the pulse profiles. It is therefore reasonable to approximate the DFDL pulse as a Gaussian pulse.

For the Gaussian profile described by equation (4.17), the pulse duration (FWHM (full width at half maximum)), Δt, is given by

$$\Delta t = \sqrt{\frac{8 n_0 \tau_{cu} \ln 2}{k_n}} . \qquad (4.18)$$

The relationship between the pulse duration and the rate of depletion of population is clearly expressed in this equation.

The total number of photons emitted (q_t) for the entire pulse may be expressed as

$$q_t = \frac{V}{\tau_{cu}} \int_{-\infty}^{\infty} q(t)\, dt, \qquad (4.19)$$

where V is the volume of the laser cavity. Now, substituting equation (4.17) into equation (4.19) and evaluating the integral gives

$$q_t = \frac{V q_0}{\tau_{cu}} \sqrt{\frac{2\pi n_0 \tau_{cu}}{k_n}} . \qquad (4.20)$$

Combining this with equation (4.18) gives

$$\Delta t = \frac{q_t}{q_0} \frac{\tau_{cu}}{V} \sqrt{\frac{8 \ln 2}{2\pi}} . \qquad (4.21)$$

For a four-level laser system with the stimulated emission process totally dominating the de-excitation of the upper state population, the total number of emitted photons can be expressed as

$$q_t = f |\Delta n| V, \qquad (4.22)$$

where $|\Delta n|$ is the total drop of population inversion per unit volume

and f is the fraction of energy, released as a result of population de-excitation, being converted into the emitted photons. If there is no loss in the system, f will be close to unity.

For a Gaussian pulse, 76% of all the photons are emitted within the "FWHM" pulse-width, Δt. Within our assumption, the drop of population inversion during this period is therefore roughly equal to 76% of the total drop of population, $|\Delta n|$. Hence, a reasonable estimate of the population depletion rate (k_n) would be obtained by dividing $0.76|\Delta n|$ by Δt:

$$k_n = 0.76 \frac{|\Delta n|}{\Delta t} . \tag{4.23}$$

The values of k_n and $|\Delta n|$ can be measured from the graphical outputs of the computer simulations, whereas the calculations of Δt are performed within the computer program. Equation (4.23) was found to agree fairly well with the results of computer simulations. For example, the data corresponding to Figure 4.28 are $|\Delta n| = 3.8 \times 10^{22}/m^3$, $\Delta t = 121.4$ ps. This gives a value of k_n at $2.4 \times 10^{32}/m^3s$ according to equation (4.23). It should be compared with the value of k_n measured from the graph: $2.8 \times 10^{32}/m^3s$.

By combining equations (4.22), (4.23) and (4.21), we obtain

$$q_0 = 1.23 f k_n \tau_{cu} . \tag{4.24}$$

This equation, together with equation (4.13), may now be substituted into equation (4.18) to give

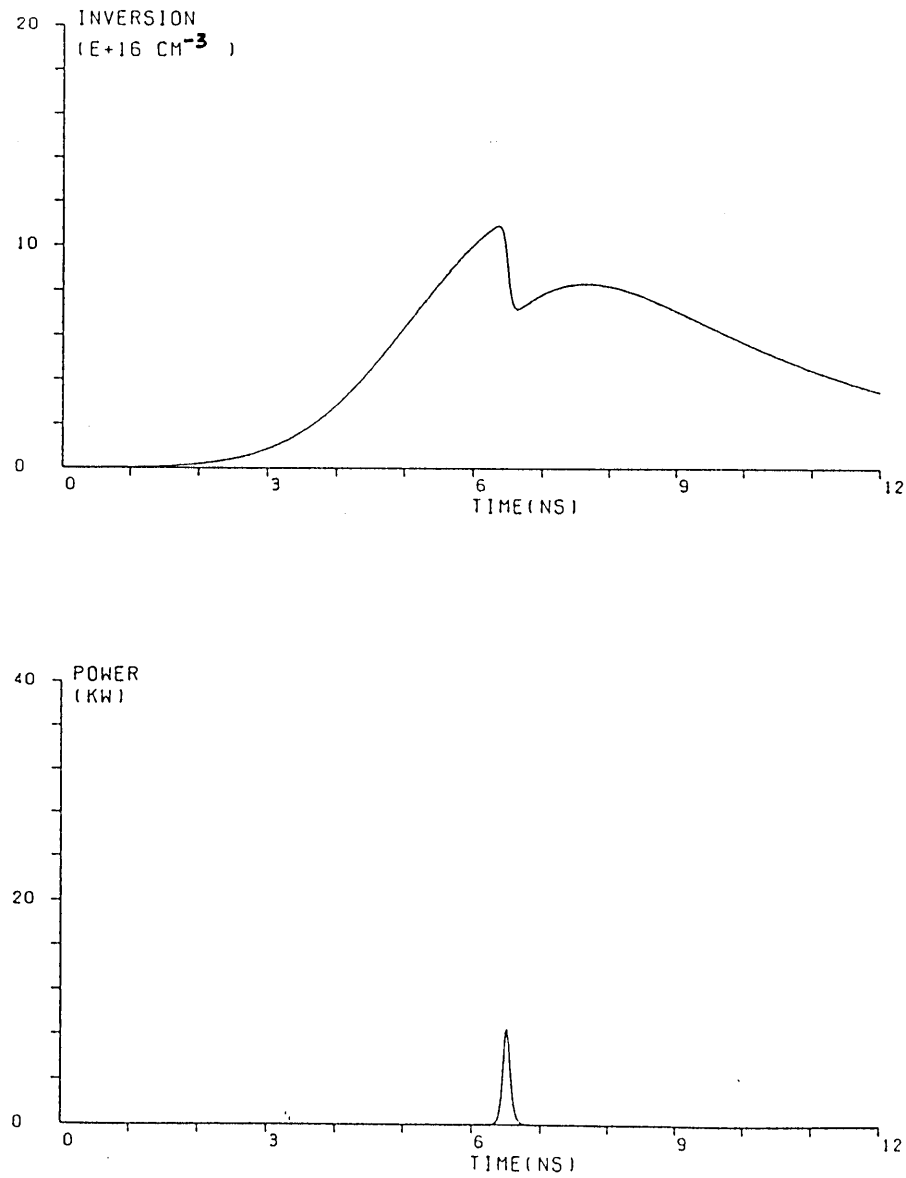
$$\Delta t = \sqrt{\frac{6.82 f \eta \tau_{cu}}{(\sigma_e - \sigma_a) c q_0}} . \tag{4.25}$$

The output power of the DFDL was given by equation (3.9). In the undercoupled DFDL model, the peak power of a DFDL pulse (P_0) is therefore given by

$$P_0 = \frac{1}{2} \frac{hc}{\lambda_0} \frac{q_0 Lab}{\tau_{cu}} . \tag{4.26}$$

Combining this with equation (4.25) yields

Figure 4.28. Temporal characteristics of a DFDL.



$$\Delta t = \sqrt{\frac{3.41 f \eta h L a b}{(\sigma_e - \sigma_a)\lambda_0}} \quad \frac{1}{\sqrt{P_0}} . \qquad (4.27)$$

In our computer simulations, the value of σ_e is twice as much as σ_a. This implies that for every two photons being involved in the stimulated emission process, there is another one being absorbed by an excited-state molecule, which will subsequently end up in an even higher excited state. Therefore only 2/3 of all the photons generated as a result of de-excitation will end up as emission photons. In this case, the value of f in equation (4.22) should be equal to 2/3. Again, the magnitude of the value f may be determined from the results of computer simulations. For example, the data corresponding to Figure 4.28 are $|\Delta n| = 3.8 \times 10^{22}/m^3$, $\Delta t = 121.4$ ps, $P_0 = 8.5$ kW. The value of q_t is therefore equal to 6.8×10^{12}. This implies that the value of f is 0.69.

The relationship between the peak power and the pulse duration of a DFDL pulse is clearly expressed in equation (4.27). The results of computer simulations can be used to check the accuracy of this expression. Table 4.1 gives such a comparison. Column 1 of each row shows the pumping rate used. The peak power of the pulse is written down in column 2, and column 3 shows the corresponding pulse duration. For each particular value of peak power, the pulse duration can also be calculated using the expression in equation (4.27); the result is shown in column 4. The differences between the results calculated from the expressions in equation (4.27) and the full computer numerical evaluations are less than 10%.

Equation (4.27) may be expressed more generally as a simple proportionality relationship:

$$\Delta t \propto \frac{1}{\sqrt{P_0}} \qquad (4.28)$$

or

$$\Delta t \sqrt{P_0} = \text{constant}. \qquad (4.29)$$

This relationship may easily be verified by plotting the value of $1/\sqrt{P_0}$ against the pulse duration Δt. Figure 4.29 shows the theoretical relationship between the peak power (P_0) and the pulse duration (Δt) calculated using the undercoupled DFDL (computer) model. The different pumping rates used range from $0.6 \times 10^{26} cm^{-3} s^{-1}$

Table 4.1: Relationship between Peak Power and Pulse Duration

Pumping Rate (E + 28)	Computer Simulation Results		Δt calculated from eqn. (3.27)
	Peak Power P_o	Pulse Duration Δt	
1.20	8.5 kW	121 ps	132 ps
1.32	11.2 kW	107 ps	115 ps
1.50	14.4 kW	95 ps	102 ps
1.50	4.1 kW	174 ps	191 ps
2.0	20.8 kW	80 ps	85 ps
2.0	10.4 kW	116 ps	120 ps
2.0	4.1 kW	186 ps	191 ps

Figure 4.29 Theorectical relationship between peak power and pulse duration

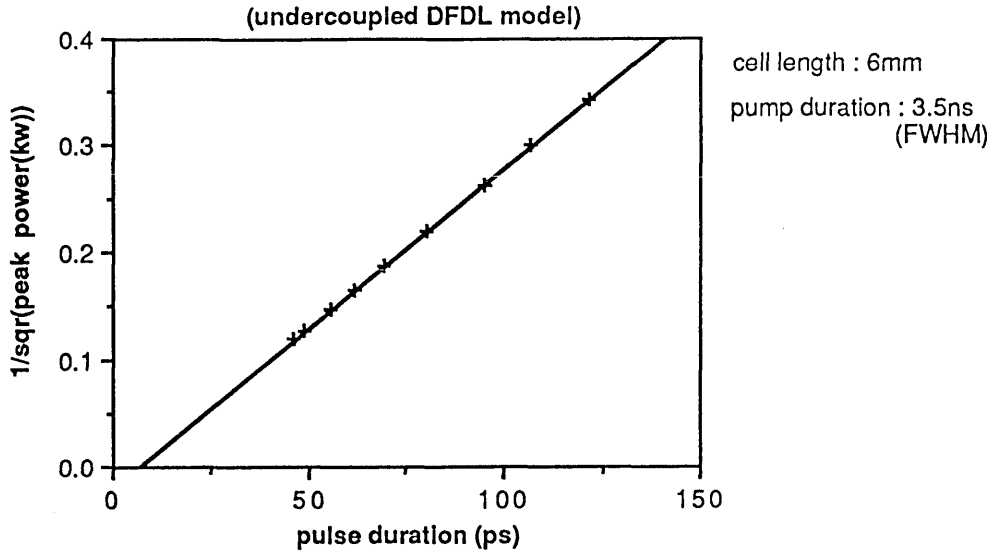
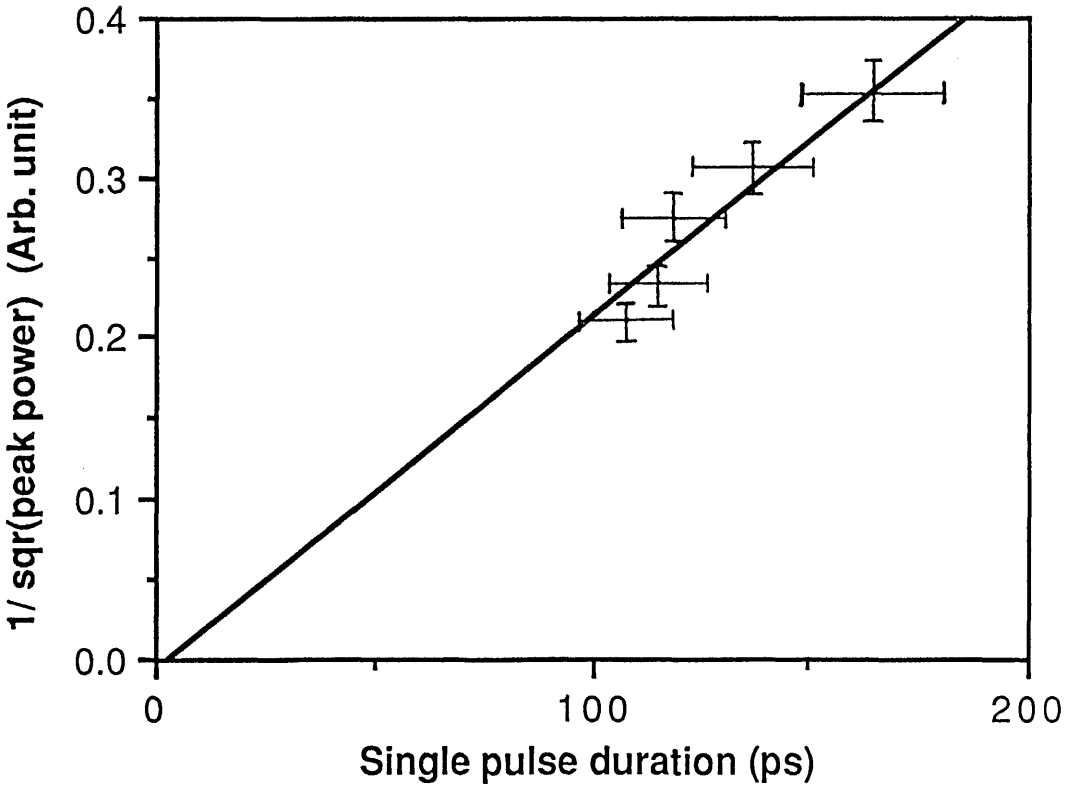


Figure 4.30 Relationship between peak power and pulse duration : experimental result



to 40 x $10^{26}cm^{-3}s^{-1}$. The data are associated with the first DFDL pulse for each level of pumping rate. Apart from a small offset, the linear relationship is clearly a fairly good approximation.

Some experimental results obtained by us at Imperial College are also used to compare with this simple relationship (4.28). Figure 4.30 is obtained from the measurements of the streak-camera traces of single pulses from a distributed feedback dye laser. The experimental results agree fairly well with the simple analytic expression of equation (4.28).

It is interesting to see whether the same relationship applies to the overcoupled DFDL model which is based on a varying cavity decay time. Figure 4.31 gives the results computed with this model. Clearly, the relationship described by equation (4.28) is equally applicable in this case despite the fact that it is originally derived from a model based on a constant cavity decay time. This is understandable since, apart from the self Q-switching effect, both models should have similar basic features and therefore should produce results having common general characteristics. This further supports the argument that the self Q-switching effect may be treated separately as a further pulse-shortening effect on top of the more basic pulse-shortening mechanism that can be satisfactorily described in terms of relaxation oscillation. The data in Figure 4.32 are extracted from the results published by Bor [10]. The parameters used are slightly different from those for our calculations but the linear relationship (4.28) is clearly a good approximation.

Another interesting expression can be obtained by combining equations (4.21) and (4.25):

$$\Delta t \propto 1/q_t \ . \tag{4.30}$$

Since the energy of a pulse (E) is directly proportional to the number of emitted photons (q_t), therefore we would expect

$$\Delta t \propto 1/E \tag{4.31}$$

or

$$E\Delta t = \text{constant}. \tag{4.32}$$

Figure 4.33 illustrates this theoretical relationship between the

Figure 4.31 Theoretical relationship between peak power and pulse duration

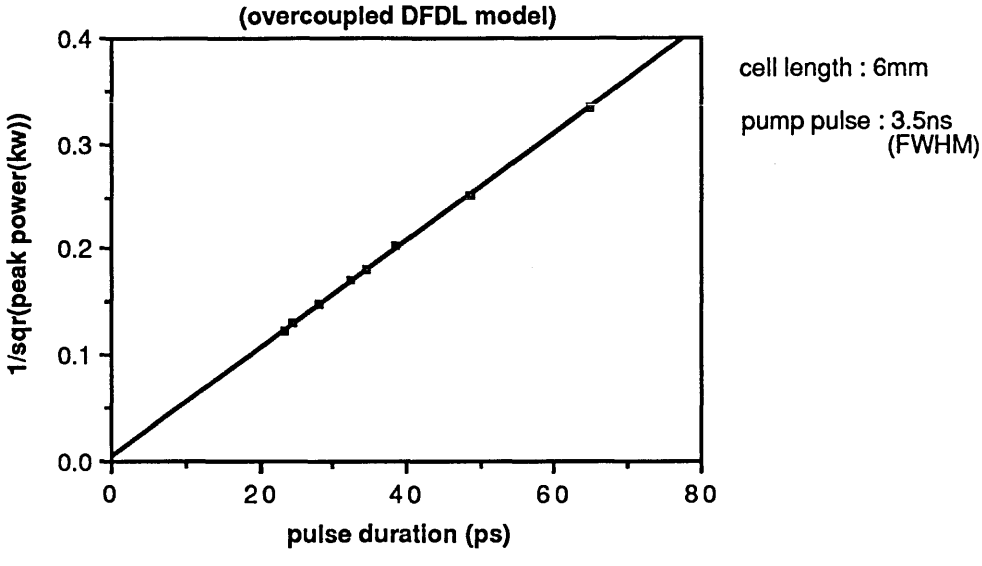


Figure 4.32 Theoretical relationship between peak power and pulse duration

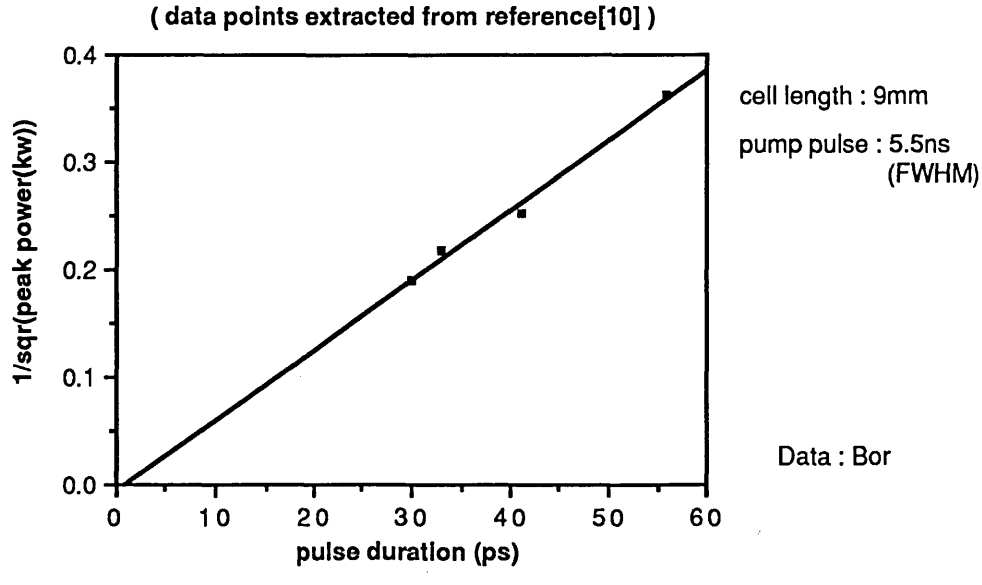


Figure 4.33 Theoretical relationship between pulse energy and pulse duration

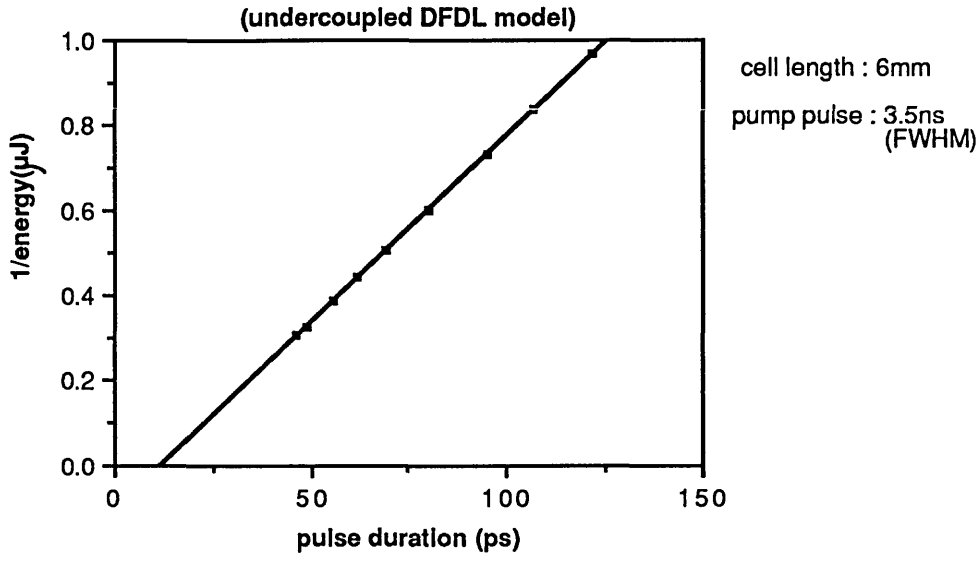
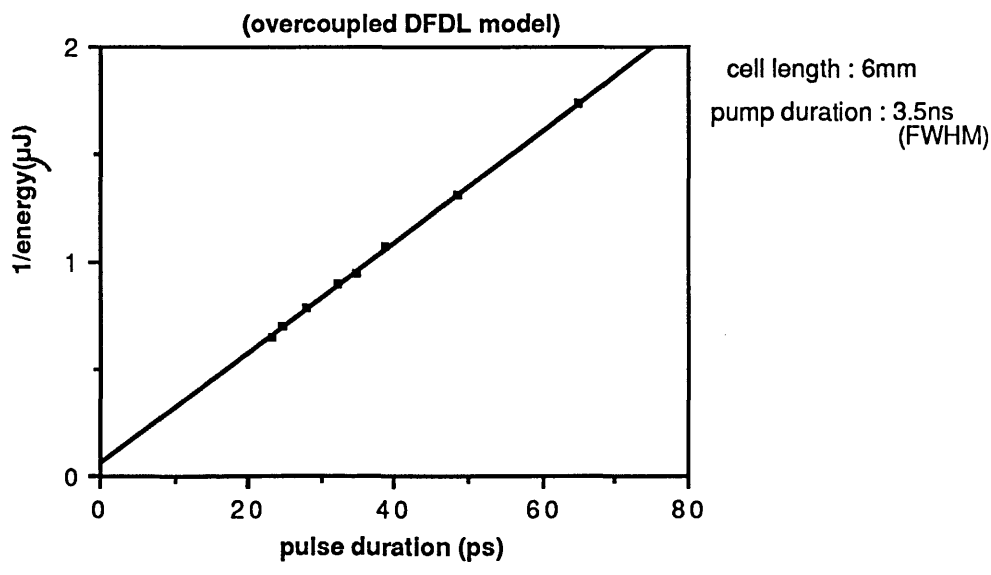


Figure 4.34 Theoretical relationship between pulse energy and pulse duration



pulse energy and the pulse duration. The data points are obtained from the full numerical computations using the undercoupled DFDL model. Apart from some offset, the relationship expressed in equation (4.31) is a fairly reasonable approximation. Again, we can test whether the same relationship applies to Bor's overcoupled DFDL model. Figure (4.34) shows that the relationship applies equally well as before.

It can be deduced from the computer simulations of laser output that the duration of a pulse is related to how much the population inversion has dropped during pulse formation. A more formal relationship can be obtained by combining equations (4.22) and (4.23):

$$\Delta t \propto 1/|\Delta n|. \qquad (4.33)$$

From another point of view, the total drop of population inversion depends on the maximum value of inversion reached prior to pulse formation. More importantly, it is related to the initial "overshoot", that is, the difference between the maximum value and the threshold value of population inversion (or the excess population inversion). When the population inversion first exceeds the threshold value, the main "pulse" is not emitted immediately but some pulse build-up time is passed before the pulse is formed. In fact, during this pulse build-up time interval, energy from the pump pulse is continuously being deposited into the laser system and the population inversion continues to increase until the cavity-photon number grows to such a high level that the stimulated emission rate exceeds the pumping rate. It is the amount of this excess population inversion which will strongly influence the pulse duration as well as the energy of the coming pulse.

Obviously, the excess population inversion depends strongly on the pumping rate during the pulse build-up time, since part of the pumping rate is required to keep the laser above the threshold by balancing out the de-excitation processes. We would therefore expect the excess pumping rate (i.e. the difference between the average pumping rate and the threshold value) to be the basic determinant on the excess population inversion achieved at the end of this pulse build-up time. Hence, the pulse duration should ultimately depend on the average excess pumping rate during this pulse build-up time. One

way of showing this dependence is illustrated by Figure 4.35. The pulse duration is plotted against the reciprocal of the square root of the excess pumping rate. The data points are obtained from the computer calculations using the undercoupled DFDL model. The corresponding peak power of the 3.5ns-duration pump pulse ranges over three orders of magnitude (from $I_p = 0.12 \times 10^{25} cm^{-2} s^{-1}$ to $I_p = 256 \times 10^{25} cm^{-2} s^{-1}$). Apart from some offset, the relationship is rather close to a linear one. Figure 4.36 is the corresponding theoretical relationship between the pulse duration and the excess pumping rate for the overcoupled DFDL model. The data points are extracted from Bor's computer solutions in reference [10]. The similaries between the results of the two models are apparent.

We have seen from previous results that the duration of the first pulse decreases rapidly initially as the pumping rate increases above the threshold. However, further increase in the pumping rate does not lead to significantly shorter pulse duration. This can be explained in terms of the relationship between the pulse duration and the excess pumping rate.

As soon as the pumping rate of the pump pulse exceeds the threshold, the gain of the system starts to build up and the number of cavity photons in the cavity starts to increase exponentially leading to the formation of a pulse at the end of the pulse build-up time. With a higher power pump pulse, the gain will be increased at a faster rate and the pulse build-up time will be shorter. The process of pulse build-up will be fast enough so that the pumping rate at the end of the pulse build-up interval does not exceed the threshold value by a large factor. Therefore, the average excess pumping rate during this period remains relatively constant even if the peak power of the pump pulse is increased by a large factor. Hence the pulse duration cannot be shortened by any significant amount. For example, computer solutions show that the excess pumping rate increases by a factor of only five while the peak power of the pump pulse is increased by a factor of almost a thousand (from $I_p = 0.3 \times 10^{25} cm^{-2} s^{-1}$ to $I_p = 256 \times 10^{25} cm^{-2} s^{-1}$). The corresponding duration of the first pulse in this case is only shortened by a factor of two over this range.

Fig 4.35 Theorectical relationship between pulse duration and excess pump power

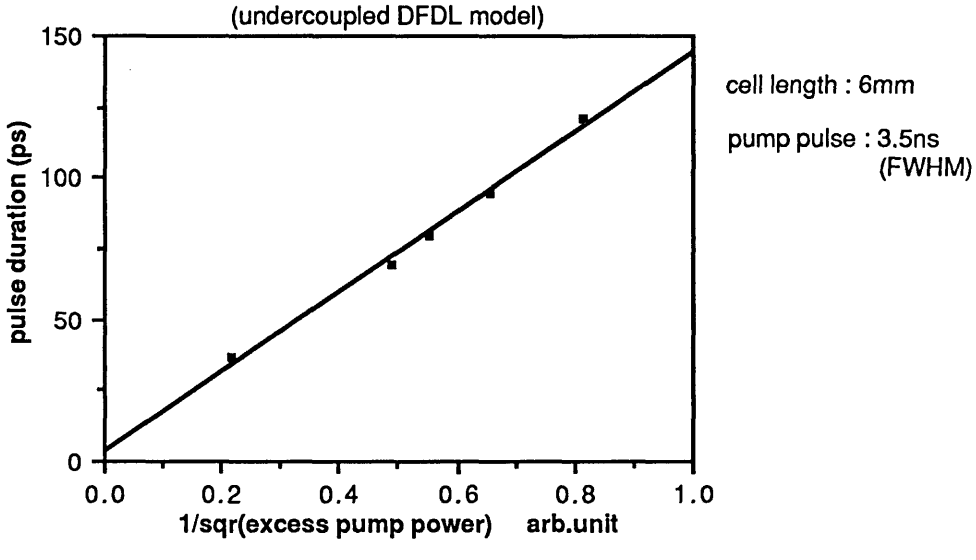
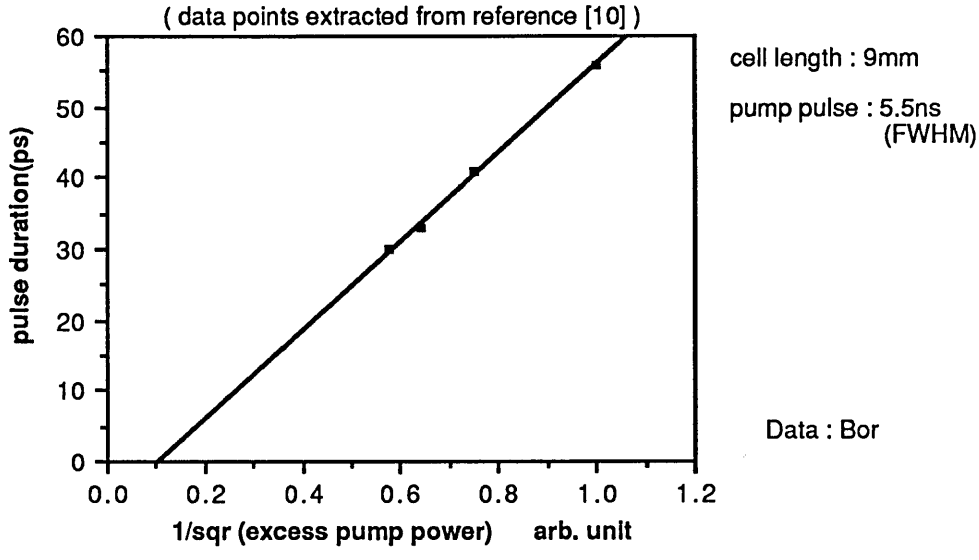


Figure 4.36 Theoretical relationship between pulse duration and excess pump power



4.5 Conclusion

A simple undercoupled DFDL model has been used to analyse the basic pulse-forming mechanism of distributed feedback dye lasers. The results from this model have been compared with other theoretical predictions. In general, the pulse durations obtained with this simple model were longer than those from the other models because the self Q-switching effect has been ignored. The similarities between these theoretical models suggested that the self Q-switching effect could be treated as a second-order effect. The pulse-forming mechanism could well be described in terms of relaxative oscillation which involved the interplay between the excess population inversion and the cavity photons. The self Q-switching effect could be regarded as an additional effect contributing to further pulse-shortening by a factor of around 40%. The undercoupled DFDL model has also been used to obtain some simple approximate analytic expressions related to the general characteristics of the DFDL pulses. These expressions were shown to be in good agreement with the results from the full numerical computer calculations. Some experimental results were also used to confirm the validity of these relationships. Although the analytic expressions were derived from the simple undercoupled DFDL model, they were shown to apply equally well to the results from the overcoupled DFDL model which is based on a varying cavity decay time. This gave further support to the approach that the pulse-forming mechanism could be described in terms of relaxation oscillation and that the self Q-switching effect can be treated separately. The results of the analysis showed, among other things, that the output profiles of the DFDL pulses closely resembled the Gaussian pulse and that the pulse duration was inversely proportional to the square root of the peak power of the pulse. It was also deduced that the duration of the first pulse of a DFDL was ultimately determined by the average excess pumping rate during the pulse build-up time.

CHAPTER 5

EXCIMER LASER PUMPED DISTRIBUTED FEEDBACK DYE LASER

5.1 Introduction

The gain-coupled distributed feedback dye laser (DFDL) was invented by Shank, Bjorkholm and Kogelnik in 1971 [3]. Since then, the spectral characteristics of the DFDL have been extensively studied. Whereas it was well known for some time that narrow linewidth coherent light could be generated by these lasers, the temporal behaviour of the DFDLs was largely ignored until it was discovered that these lasers emitted picosecond pulses under certain pumping conditions [17]. The first detailed studies of picosecond pulse generation with gain-coupled DFDLs were described by Bor [10]. Instead of a beam splitter, as used by Shank et al. [3], a holographic grating was used as the beam-splitting device. A nitrogen laser pump beam, of normal incidence to the grating, was diffracted by the holographic grating into the +1 and -1 orders, which were then recombined, via two mirrors, at a dye cell containing the active medium, an organic dye solution of rhodamine 6G. The interference fringes of the pump beams led to a spatial modulation of gain in the active medium, thus providing the feedback essential for laser oscillation. Within certain pumping power range, single short pulses of duration of about 100 ps were generated. The pulses were also found to be nearly transform-limited.

Further experimental work on the DFDL has since then led to other elaborated methods of generating shorter pulses. For example, with the help of a quencher laser, it was possible to reduce the DFDL pulse duration by a factor of 1.5 to 1.7 [14]. Usually, a train of short pulses is generated when the laser is pumped well above threshold. However, by the proper timing of the injection of a quencher laser pulse into the DFDL cavity, part of the stored energy is extracted so that after the formation of the first pulse, the DFDL remains below threshold for the rest of the pump pulse. Hence only the first DFDL pulse is generated while the successive pulses are suppressed.

A very effective way of generating shorter pulses is simply to use shorter pump pulses. Bor et al. [18] investigated this experimentally. For example, a passively mode-locked Nd:YAG laser was used as the source of short pump pulses in an experiment. Pulses of 16 ps duration, obtained from frequency tripling (355 nm), were used to pump a DFDL. The duration of the DFDL pulses generated with these short duration pump pulses was as short as 1.6 ps [19].

Using a travelling-wave pumping scheme, the pulse duration generated by a DFDL could become as short as 1 ps when pumped by a 5 ps duration pump pulse [20]. And very recently, a new achromatic distributed feedback dye laser arrangement has been developed [21]. Subpicosecond pulses (~ 320 fs) were generated with a pump pulse duration of 8 ps.

Undoubtedly, the distributed feedback dye laser is an attractive system for the generation of ultrashort pulses of duration in the range of 1 ps to 100 ps. In fact, in some respects, the DFDL systems have certain special features that give them some advantages over the conventional mode-locking systems in the generation of picosecond pulses. The DFDL, in its simplest form, is inexpensive, compact and reliable. No sophisticated optical or electronic components are required for its operation. Continuous tuning over several nanometers without mode hopping has been demonstrated experimentally and shown to be straightforward [17]. Since saturable absorbers are not needed, the system can be used to generate short pulses at any wavelength ranging from 360 nm to 800 nm [22]. Hence the entire visible spectrum can be covered with the help of various tuning methods. With a special but simple optical pumping arrangement, any pulsed pumping laser (with an appropriate excitation wavelength) including broadband lasers, such as the nitrogen and excimer lasers, can be used to produce high spectral quality outputs. The pulse repetition rate is continuously variable and is simply determined by the repetition rate of the pumping laser. Single picosecond pulses can be obtained without pulse selectors. Also, the spectral properties of the gain-coupled DFDL are excellent; simultaneous measurements of the pulse duration and spectral linewidth have shown that the DFDL pulses were close to being transform-limited. Since only a small fraction of the pump energy is required to pump the DFDL, an oscillator-amplifier system can be constructed to generate high power laser pulses [23]. In the following, experimental studies

of an excimer pumped distributed feedback dye laser will be described. The laser has been used as the basis for the construction of a master oscillator-amplifier system which is used to generate intense ultrashort UV pulses.

5.2 XeCl Excimer Laser Pumped DFDL

5.2.1 Introduction

The construction of an excimer laser pumped DFDL system producing transform-limited single pulses of 100 ps duration with good transverse beam quality will be described.

The organic dye laser is the most versatile continuously tunable coherent light source. The fluorescence bands of individual dyes are several tens of nanometres wide. For the operation of pulsed laser pumped dye lasers, the spectral range from the UV at 310 nm to the near IR (infrared) at 1285 nm can be covered by different dyes. In particular, the XeCl excimer laser system on its own can provide coverage of the entire spectrum from 330 nm in the UV to 975 nm in the IR; only the lasing dye itself needs to be changed [24]. This is because most dyes have an absorption band at the lasing wavelength of the XeCl laser (308 nm), and because these populated states of the dyes are coupled very efficiently with the upper laser level S, through fast internal relaxation processes.

In general, commercial rare gas halide excimer lasers offer high peak power and high repetition rates, and the operation of such laser systems is relatively simple. The XeCl laser is especially attractive because of its long gas-fill lifetime; this also means relatively low operational costs. The excimer laser used in our DFDL experiments was made by Lamda Physik (EMG 101). Normally, a standard gas fill was used to obtain the XeCl emission at 308 nm. The maximum energy output from the XeCl laser was 150 mJ in a pulse of duration of approximately 10 ns. A typical pulse shape is shown in Figure 5.1. Although the laser could be operated at a repetition rate of up to 50 Hz, most of the experiments were carried out with single shots. The output beam of the excimer laser was quite uniform across the rectangular beam which had a dimension of 10 mm times 26 mm at the front window of the laser. The vertical divergence for XeCl

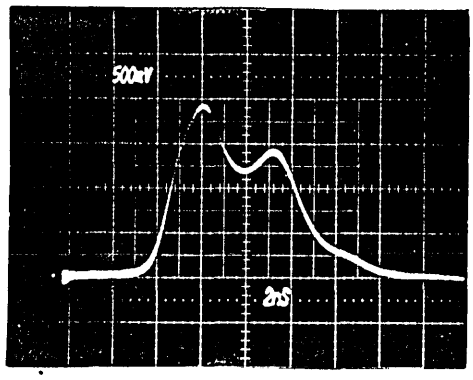


Figure 5.1. Typical pulse shape of the Lambda Physik EMG 101 XeCl laser output.

operations was quoted as 1.1 mrad and the horizontal divergence is 2.5 mrad .

To create the spatial gain modulation required for the essential distributed feedback, the UV beam from the XeCl excimer laser was split into two which were then recombined to produce the interference fringes at the dye cell. The spatial modulation of pump intensity would lead to a spatial modulation of population inversion and hence the gain. It is important that the visibility of the interference fringes should be good so that the gain modulation is deep enough to give the strong feedback required for laser oscillation. This can be easily achieved with pump source of high spatial and temporal coherence. However, the XeCl excimer laser is a broadband laser with low spatial coherence; a special pumping arrangement is thus required.

5.2.2 Pumping arrangement for the DFDL

In order to produce good visibility fringes from the broadband XeCl excimer laser, the "achromatic" pumping arrangements, first proposed by Bor [25], was used in our distributed feedback dye laser. A schematic diagram of this pumping arrangement is shown in Figure 5.2. The pumping beam enters normally into the quartz parallelepiped (15 mm x 50 mm x 58 mm) after passing through a cylindrical lens (focal length 190 mm), which is not shown in the diagram. The holographic grating diffracts the normal incidence beam into the +1 and -1 orders. The diffracted beams undergo total internal reflection at the sides of the quartz block and recombine on the surface of the dye cell. The focal line on the dye cell is perpendicular to the grooves of the grating. The use of a wedge dye cell can prevent reflection of the DFDL output beam from the side windows of the cell directly into the lasing region of the active medium. Careful consideration of the geometry shows that the interference fringe separation Λ is given by

$$\Lambda = d/2, \qquad (5.1)$$

where d is the grating constant, the reciprocal of the number of lines per unit length. Therefore the fringe separation at the dye

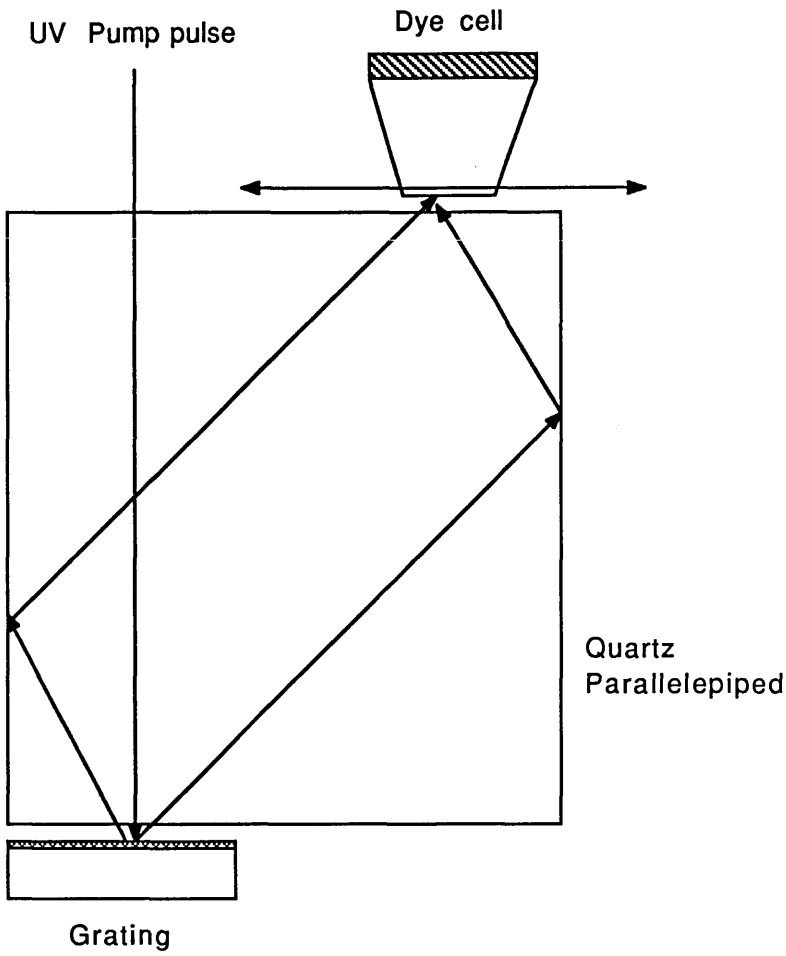


Figure 5.2 Schematic diagram of distributed feedback dye laser

cell is independent of the pumping wavelength. This means that each spectral component of the XeCl laser radiation creates an interference pattern with the same fringe separation. Another important property of this special geometry is that for each point on the dye cell, the two interfering beams have been diffracted from the same point on the grating. This point-to-point matching between the holographic grating and the active region of the dye makes it possible to obtain good visibility interference fringes although the spatial coherence of the XeCl beam is relatively low. The main drawback of this special pumping scheme is that the only practical way of tuning the laser is by changing the refractive index of the solvent.

It must be stressed that the intensities of the two non-zero diffracted pumping beams from the grating must be well-balanced. Otherwise, the visibility of the interference fringes may not be good enough to generate sufficient feedback for laser oscillation or the DFDL output beam may have a very high content of amplified spontaneous emission (ASE).

The alignment of the distributed feedback dye laser involved the steering and focusing of the diffracted pumping beams into narrow-beam-waist focal lines, which had to overlap each other right at the inner surface of the dye cell. Some of the alignments were found to be critical to the proper operation of the DFDL. Nine micrometer screw gauges were used in the mounts for the fine adjustments of the relative positions and orientations of the main optical components. The holographic grating was fixed on a kinematic mount so that the direction of the normal of the grating can be aligned with the incoming UV pumping beam. The kinematic mount was on a translational stage so that the distance between the grating and the quartz parallelopiped could be adjusted. The orientation of the quartz parallelopiped was controlled by three micrometer screw gauges; they provide the fine adjustments in the rotational movements about the three orthogonal axes. The dye cell could be rotated about the vertical axes to become parallel with the grating. Its position relative to the rest of the optical components was controlled with a translational stage. The cylindrical lens was also on a translational stage so that the position of the focal plane can be independently controlled.

Apertures, UV attenuators and beam splitters were used to control

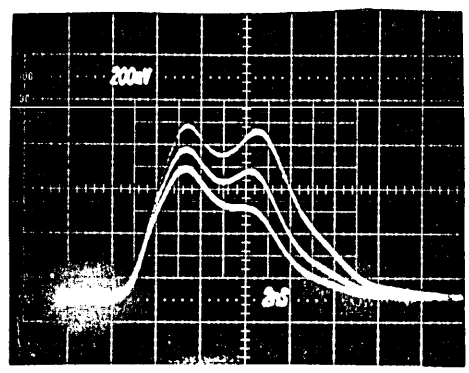
the UV pumping power entering the distributed feedback dye laser. The fine adjustment of the pumping power was made with a uniformly thick glass slide, which was mounted on a rotational stage. By varying the angle of the glass slide to the propagation direction of the pumping beam, the effective thickness of the glass slide, as seen by the pumping beam could be changed and the amount of attenuation by the glass slide varied.

5.2.3 Experimental studies of the DFDL

The pumping pulse as well as the DFDL output were usually monitored with ITL TF1850 UV photodiodes connected to a Tektronix storage oscilloscope with an amplifier having a rise-time of 1 ns (Tektronix 7A19) and a timebase with a maximum resolution of 1 ns per cm (7B72A). Theoretical simulations showed that the laser output of a DFDL could be fairly sensitive to the power of the pumping pulse. In fact, the pumping pulse shape could have some important effects on the operation of a DFDL. For our XeCl laser, this required attention since the pulse shape varied with the main discharge voltage of the laser. Figure 5.3 shows such variations for a fresh gas fill. The pulse energy and peak power decreased as the discharge voltage was decreased. The discharge voltages corresponding to the three traces in Figure 5.3a are 30 kV, 25 kV and 23 kV respectively. The corresponding energies are 105 mJ, 77 mJ and 57 mJ respectively. For Figure 5.3b, the corresponding discharge voltages are 23 kV, 22.5 kV and 22 kV, and the pulse energies are 57 mJ, 46 mJ and 38 mJ respectively. In general, there were two peaks in the pulse profile of the XeCl laser output. The drop in the total pulse energy, as the discharge voltage decreased, was largely due to the diminishing power of the second peak, although there was a reduction in the power of the first peak. In fact, for an old gas fill (after ~ 10^6 shots), the second peak almost disappeared completely even when the discharge voltage was high. An example is shown in Figure 5.4; the discharge voltage of the XeCl laser pulse was 30 kV and the pulse energy, measured with a calorimeter, was 48 mJ.

With a double-peak pump pulse, the generation of single DFDL pulses can be problematic, for double DFDL pulses are expected to be formed as soon as the pumping threshold is exceeded. It should be

a)



b)

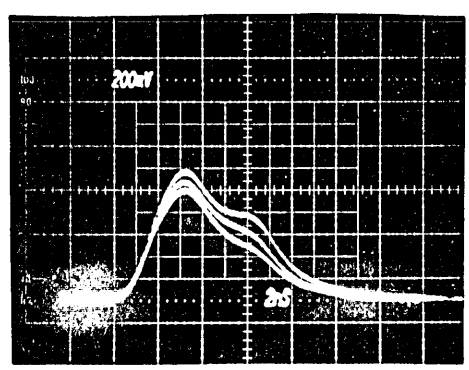


Figure 5.3. Variation of the XeCl pulse shape with main discharge voltage.

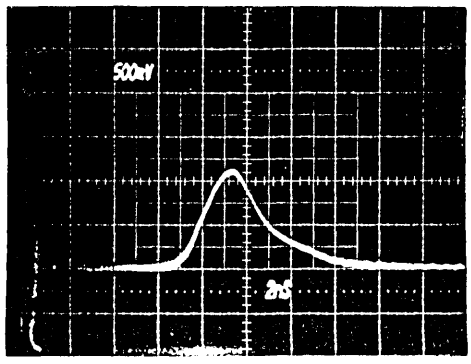
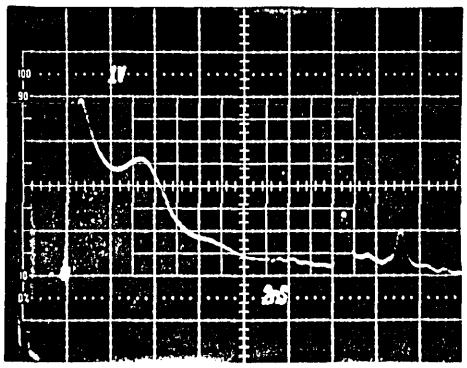


Figure 5.4. XeCl pulse shape for an old gas-fill.

Figure 5.5. Generation of DFDL double-pulse with a double-peak pump pulse.



impossible to have single-pulse generation. In fact, this behaviour was observed in early experiments (Figure 5.5). Part of the double-peak XeCl pump pulse is shown on the left-hand side in Figure 5.5; the two DFDL pulses generated are also recorded on the right-hand side. The temporal separation of the two DFDL pulses is very close to the separation of the two peaks of the pump pulse.

Although it is possible to avoid having the double peak simply by using a lower discharge voltage, the XeCl pump pulse produced would tend to be less stable. The use of an old gas fill also has this stability problem. On the other hand, it was found that the pulse shape of the UV pump pulse as shown on the oscilloscope did not truly represent the pulse shape at the region of optical excitation. In fact, it was possible to obtain single DFDL pulses without having to use a very low discharge voltage on the excimer laser. There will be further discussions on this in section 5.3.

Quite a few different laser dyes and solvents were used in our DFDL to generate short pulses at different wavelength. Information on some of these is summarized in Table 5.1. The exact wavelength of operation in each case depended upon the refractive index of the mixture of solvents and the grating constant (or the number of lines per millimetre). The dye was chosen to match the required wavelength so that the efficiency of the laser is optimized. The concentration of the dye solution was chosen so that the energy of the DFDL single pulses was high while the ASE level was still reasonably low. In general, the basic characteristics of the different DFDLs are similar.

Usually, the DFDL device length was set at 6 mm. The effective cross-sectional area of the pumped region in the dye was approximately 140 μm (width of focal line) x 160 μm (penetration depth). The threshold for lasing was reached with a pump energy of about 70 μJ, corresponding to a threshold pump power of around 10 kW. Single pulses (Figure 5.6a) of duration around 100 ps were generated if the pump energy did not exceed the threshold value by more than ~ 25%. Above this pumping level, double or multiple pulses were produced (Figures 5.6b and 5.6c).

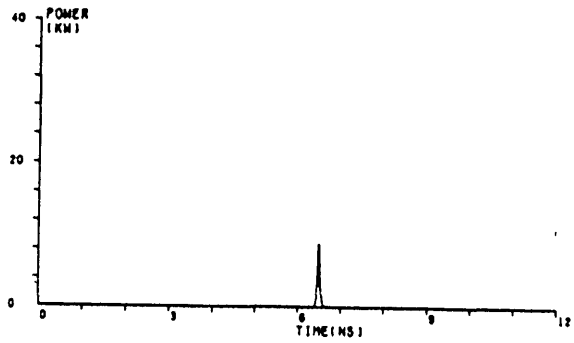
The energy of the DFDL pulses in single-pulse operation was about 0.5 μJ. The measured divergences of the DFDL beam were approximately 12 mrad (horizontal) by 15 mrad (vertical). The transverse intensity profile of the beam could be described as 'Gaussian-like'.

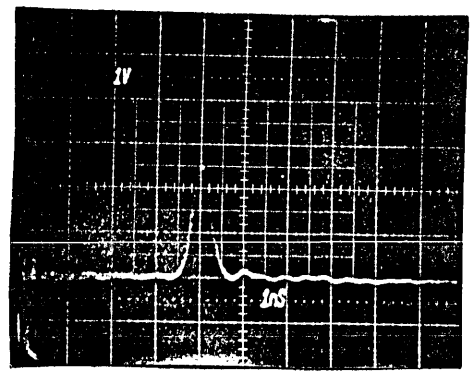
Table 5.1: Laser Dyes and Solvents used in The Distributed Feedback Dye Laser

Dye+	Solvents	Concentration	Grating (lines / mm)	Refractive Index	Wavelength
Rhodamine 6 G	80 % ethanol 20 % benzyl – alcohol	3×10^{-3} M	2400	1.40	580 nm
Coumarin 153	50 % methanol 50 % ethanol	1.3×10^{-2} M	2400	1.35	560 nm
Rhodamine B	35 % ethanol 65 % benzyl – alcohol	6×10^{-2} M	2400	1.48	616 nm
Rhodamine B	50 % methanol 50 % ethanol	2×10^{-3} M	2180	1.35	616 nm

+ Lambda Physik dyes

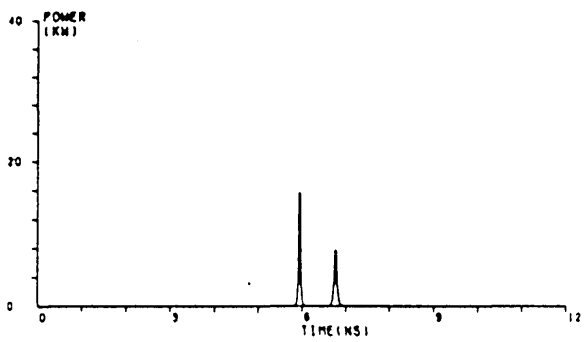
single pulse

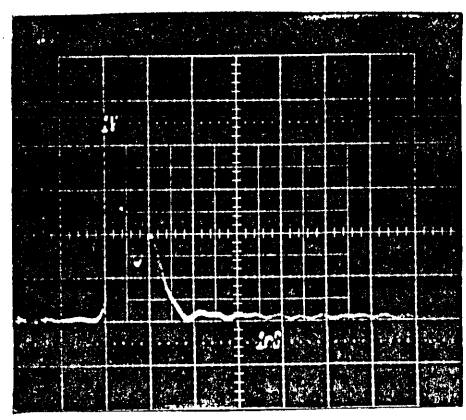




oscilloscope trace

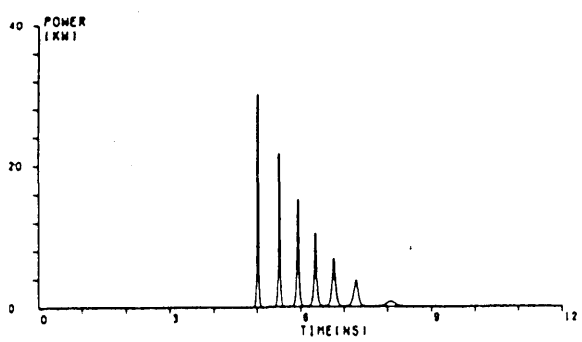
double pulse

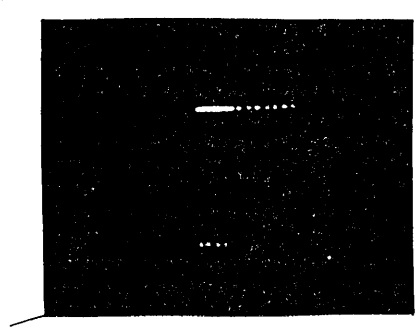




oscilloscope trace

multiple pulse





streak-camera traces

Figure 5.6. Generation of ultrashort pulses with DFDL.

In fact, the propagation of the DFDL beam was very similar to that of the fundamental Gaussian beam.

A Photocron electron-optical streak camera with a resolution of 1 ps was used for the measurements of the duration of DFDL pulses. The spectral linewidth of the pulses were measured with a plane-parallel Fabry-Perot interferometer (30 GHz free spectral range). The linewidth resolution of the interferometer was 1 GHz. Simultaneous measurements of the pulse durations and the linewidths of DFDL single pulses showed that the pulses were effectively transform-limited.

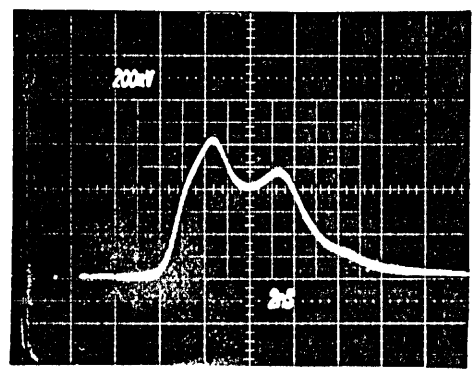
5.3 General Characteristics of the DFDL

5.3.1 Single pulse operation

The computer simulations of the temporal characteristics of the DFDL showed that a single pulse would be generated if the power of the pump pulse did not exceed the threshold value by a certain percentage. However, as was discussed in section 5.2.3, the exact shape of the pump pulse could strongly influence the output characteristics of the DFDL. The double-peak feature of the pump pulse obtained from our XeCl laser apparently could not possibly give rise to single DFDL pulses. However, our study of the divergence properties of the XeCl beam revealed that the pulse shape actually varied with the divergence angle.

Using a quartz spherical lens of focal length of 66 cm and a 100 μm pin-hole placed at the focal plane, the shape and relative intensity of the UV pulse across different regions of the focal spot could be monitored. The pulse shape and intensity were found to be quite constant across the horizontal direction over a region of 1.2 mm, corresponding to a divergence angle of 1.8 mrad. Across the vertical direction, the region of constant pulse shape and intensity was only about 200 μm (± 50 μm) wide, corresponding to a divergence angle of about 0.3 mrad. Within this region, the shot-to-shot stability of the pulse was also very good (± 5%). The pulse shape, however, was different from that of the entire beam. Figure 5.7 illustrates this point. The pulse shape at the top was the temporal profile of the whole beam that entered the dye cell of the DFDL. The profile at the bottom was obtained near the central region of the

a)



b)

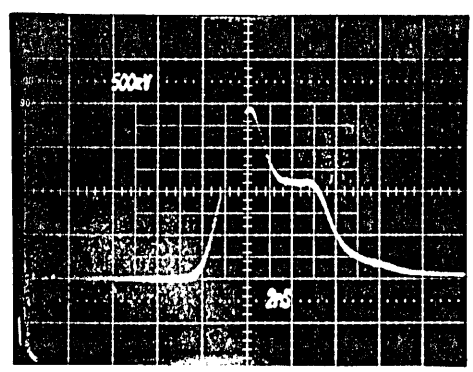


Figure 5.7. Pulse shapes of XeCl pump beam.

a) for the entire beam

b) near the central region of the focused beam

focused beam. In fact, at the very centre of the focal spot, the pulse shape was rather similar to the Gaussian pulse profile and resembled the pulse shape from the laser with an old gas fill (Figure 5.4). Outside the central region, the pulse intensity decreased rapidly. Both the pulse shape and intensity became very unstable from shot to shot. Some of the pulse shapes were very different from the profiles shown in Figure 5.7.

In the distributed feedback dye laser, a cylindrical lens of focal length 190 mm was used to focus the pump beam into the dye cell. The results obtained above imply that the effective width of the focal line at the dye cell could be somewhat smaller than expected (at approximately 60 μm ± 15 μm). If only the central region is pumped with an intensity high enough to exceed the lasing threshold, it will be expected that the DFDL output characteristics will depend almost entirely on the exact pulse shape at this particular region. This explains why a beam of an apparently double-peak pump pulse can produce a perfectly clean single pulse. On the other hand, a clean pulse can be generated only if the central regions of the focal lines of the interfering beams overlap each other very substantially. Indeed, the alignment which controlled this overlap was found to be very critical to the proper operation of the DFDL. It was found that this alignment had to be exact to within about 7 μm.

When the DFDL was well aligned, clean single pulses were produced with reasonably good shot-to-shot stability (± 10% : amplitude on oscilloscope). The lasing threshold was, as expected, well defined. Signals obtained from the oscilloscope showed that single pulses were generated if the pumping power level did not exceed the threshold value by more than 25%.

5.3.2 Optical beam quality

The beam quality of the laser source is usually an important parameter for many experiments involving coherent light sources. It was therefore useful to have some knowledge of the propagation characteristics of the DFDL output beam.

First of all, it was discovered that the laser beam behaved as if it was coming from a point source situated at the middle of the DFDL

cavity (6 mm in length). By placing a simple converging lens (f/ℓ 50 cm) a certain distance away from the DFDL cavity (object distance), the laser beam would be focused down to a small spot at some distance (image distance) from the lens on the opposite side. It was found that the simple lens law was obeyed.

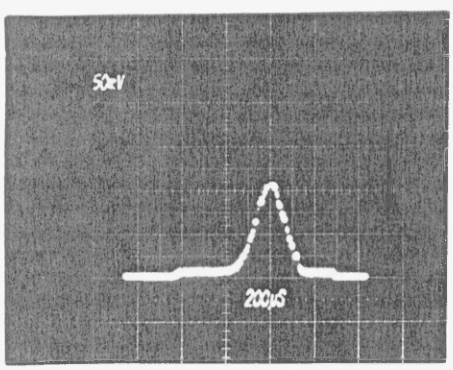
The shape of the DFDL beam was elliptical with the major axis aligned with the vertical direction. The exact transverse intensity profile across each axis of the beam was recorded with a diode-array (RECTICON CCPD 1024) connected to an oscilloscope. The profiles were found to be smooth and 'Gaussian-like'. It is therefore appropriate to analyse the propagation of the DFDL beam using the theory of Gaussian beam propagation. For the fundamental Gaussian beam, the intensity (in the transverse direction) falls off slowly without any sharp edges. Hence it is necessary to use some criterion to define the beam radius (or spot size). The beam radius is conventionally defined as the distance from the axis of the beam to the position at which the field intensity is down by a factor of $1/e^2$ compared to its value on the axis. For our elliptical "Gaussian-type" beam profile, it was necessary to specify both the horizontal beam radius and the vertical beam radius (see Figure 5.8).

The far-field divergence of the laser beam can be determined by measuring the radius of the beam at a distance far away from the laser cavity. Measurements were carried out at different positions. The vertical divergence was found to be 15 mrad (full angular spread) and the horizontal divergence 12 mrad . The vertical divergence, in fact, can be related to the intensity distribution of the UV pump beam at the focal line.

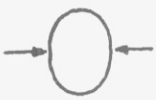
According to the theory of Gaussian beam propagation, the beam waist (w_0) (i.e. the beam radius at the centre of the DFDL cavity) is related to the far-field beam divergence angle θ_f (half angle) by

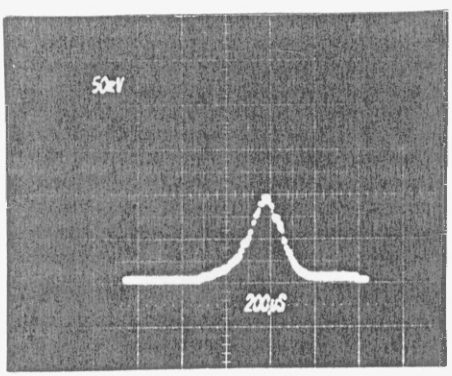
$$\theta_f = \lambda/\pi w_0 \eta, \qquad (5.2)$$

where λ/η is the wavelength in the propagating medium. This expression, however, applies to diffraction-limited beams only. For our laser, operating at 616 nm, the full vertical divergence angle of 15.3 mrad implies that the vertical beam waist should be 26 μm (i.e. beam diameter = 52 μm (± 10%)) if the beam is diffraction-limited. This value is in fact consistent with the effective width of the



horizontal beam
profile





vertical beam
profile



Figure 5.8. Diode-array records of DFDL beam profiles.

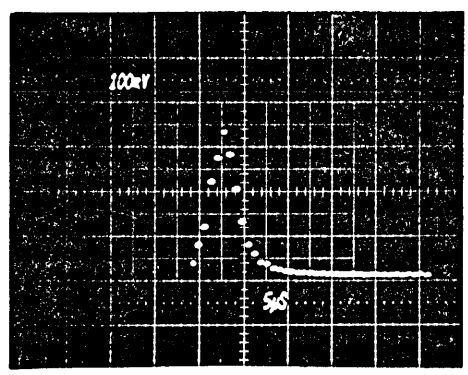


Figure 5.9. Intensity profile of a focused DFDL beam at the focal spot.

focal line of the UV pump beam (60 μm (± 25%)) found in section 5.3.1.

The beam waist of the DFDL beam can also be determined by simple geometrical optics measurements. The theory of the focusing of the fundamental Gaussian beam is also involved in this method. By placing a simple converging lens on the axis of the laser beam some distance away from the laser cavity, the focal spot at the other side of the lens was monitored using the diode array (Figure 5.9). Simple geometry, together with the paraxial approximation, can be used to show that for a fundamental Gaussian beam, the ratio of the image distance to the object distance is equal to the ratio of the size of the recorded focal spot to that of the beam waist at the laser cavity. For example, when a simple lens (f/ℓ 80 cm) was placed at 130 cm from the laser cavity, a focal spot of 110 μm (± 10%) diameter ($1/e^2$ criterion) was recorded at a distance of 224 cm from the lens. This implies that the beam diameter was 64 μm (± 10%) at the laser cavity. Again, this agrees fairly well with the earlier results, indicating that the DFDL beam was fairly close to being diffraction-limited.

According to the theory of Gaussian beam propagation, the extent of the collimated waist region of the laser beam is characterised by the confocal parameter, b, where

$$b = 2\pi w_0^2 \eta/\lambda. \qquad (5.3)$$

The confocal parameter is twice the distance which the beam travels from the waist before the beam diameter increases by a factor of $\sqrt{2}$, or before the beam area doubles. For a laser operating at 616 nm with a solvent index of 1.345, a beam waist of 64 μm implies that the confocal parameter is 14 mm. This, in fact, indicates that the beam diameter should be fairly constant throughout the 6 mm length of the laser cavity.

5.3.3 Temporal characteristics

Single-pulse generation is one of the most important features of the DFDL. In this section, the pulse intensity profiles and the durations of single pulses generated by the DFDL will be examined.

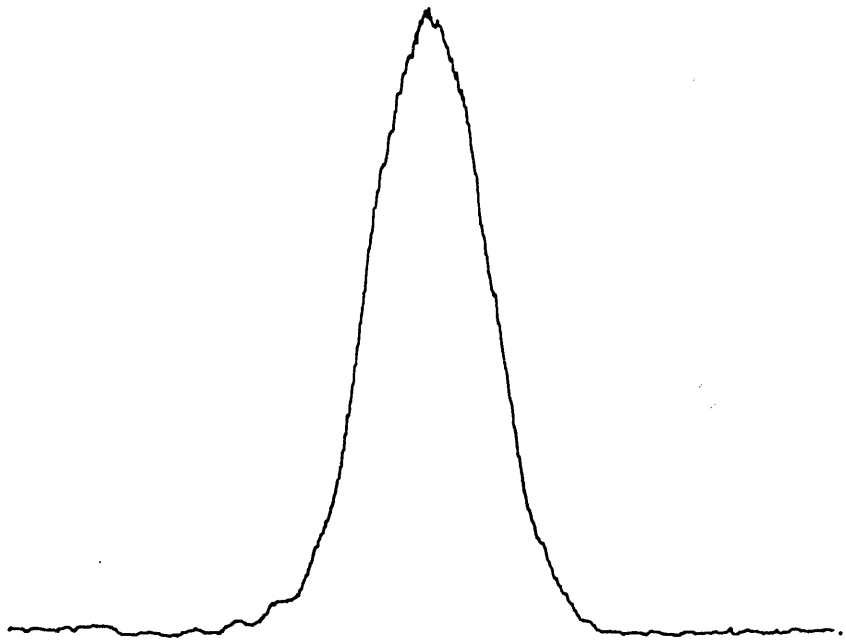


Figure 5.10. Microdensitometer plot of a DFDL pulse profile.

Figure 5.11 Linear plot of a DFDL pulse profile

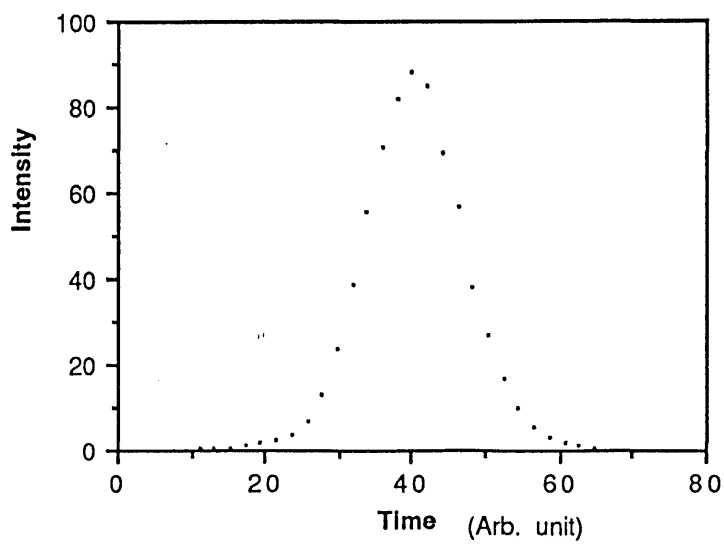


Figure 5.12 Comparision of Gaussian and DFDL pulse profiles

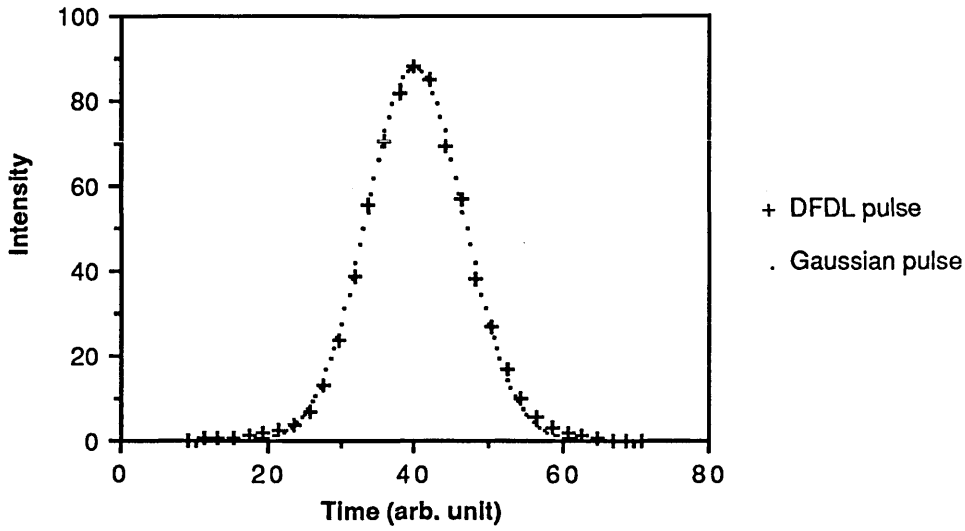
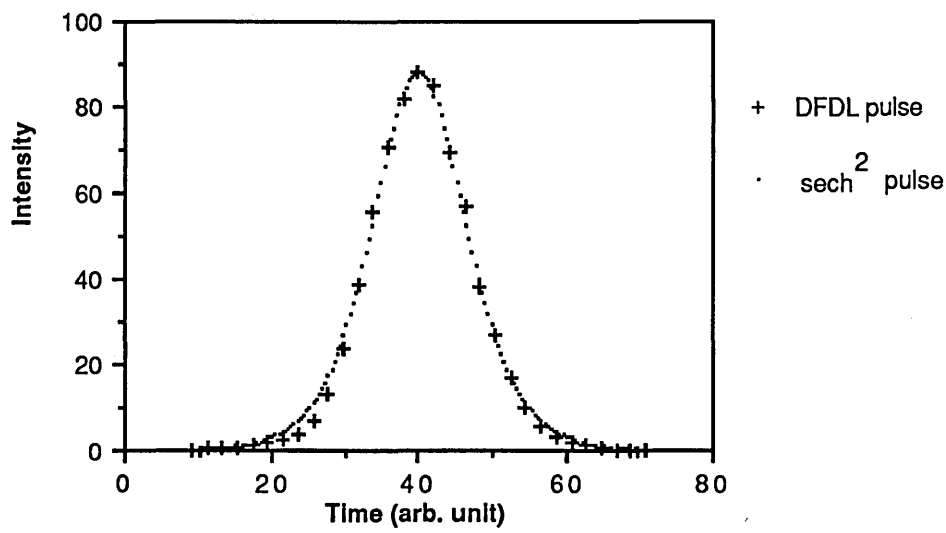


Figure 5.13 Comparison of $(sech)^2$ and DFDL pulse profiles



The resolution of the oscilloscope is not high enough to monitor the temporal characteristics of the DFDL pulses. For proper pulse-duration measurements, a Photocron electron-optical streak camera (with a resolution of ~ 1 ps) was used. The temporal profiles were converted into spatial variations of film density, which could then be analysed with a microdensitometer. The recorded optical density on the film as a function of input intensity could be calibrated with neutral density filters. The calibration of the streak timescale could be obtained by having two appropriately time-delayed identical input pulses, which were derived from one single pulse by beam-splitting. It should be noted that the microdensitometer plots of the streak traces were linear in the optical density scale but logarithmic in the light intensity scale.

Since the intensity of the DFDL pulse was low, amplification (x 100) was needed before the pulse duration could be measured with the streak camera. When the laser was well aligned, single pulses with clean profiles were obtained. Figure 5.10 is a microdensitometer trace of a DFDL single pulse. The exact pulse shape in the intensity scale can be obtained by simple conversion of a number of points into the linear scale. After the removal of the "background noise", the linear plot of intensity against time can be obtained (Figure 5.11). The intensity profile of the DFDL pulse can be compared with the Gaussian pulse profile (Figure 5.12) and the $sech^2$ pulse profile (Figure 5.13).

In general, with a well aligned laser, the pulse shape of the DFDL single pulse varied only slightly from shot to shot and the pulses were always very smooth and free from substructures. However, although the laser could be set to emit single pulses, the durations of the pulses might vary from shot to shot within a range of ± 15% about the mean value. For operation at 616 nm, single pulses of duration in the range 90 ps to 120 ps were obtained when the DFDL was pumped just below the threshold of the second DFDL pulse. When the UV pump power was decreased by 15%, pulses of duration in the range 150 ps to 200 ps were generated. All these pulses were quite smooth and without any significant substructures. The intensity of the pulses was found to decrease as the pulse duration increased (see Figure 4.30 of section 4.4).

5.3.4 Spectral properties and the time-bandwidth product

The excellent spectral qualities of distributed feedback laser sources have been known for a long time. They are the direct consequences of the wavelength sensitivity of the Bragg scattering process. The gain-coupled DFDL, in particular, has a significant additional advantage in that there is only one mode having the lowest threshold gain. The threshold for this zeroth-order mode is considerably lower than the rest of the resonant modes, making it possible for the laser to oscillate in a single mode. The fact that the transitions of the organic dye system are homogeneously broadened also favours single-mode operation.

For single-pulse operation, the laser is pumped just above threshold. Calculations from the coupled-wave theory suggest that for the zeroth-order gain-coupled DFDL, the gain of the system must exceed 1.5 times the threshold value for the next resonant mode to be excited at all. Computer simulations can show that this will never happen in our experimental conditions for single-pulse operation. Indeed, all gain-coupled distributed feedback dye lasers operated in single-pulse generation always produce single-mode output.

The spectral properties of the distributed feedback dye laser output were investigated with a 30 GHz (F.S.R.) plane-parallel Fabry-Perot interferometer (resolution = 1 GHz). Since the intensity of the DFDL output was low, the signal was amplified (x 100) before measurements on the bandwidth were taken. The pattern of circular fringes which emerged, after passing through the interferometer, could be recorded on a Polaroid film (type 612). Figure 5.14 shows a typical fringe pattern. In this case, twelve consecutive shots were superimposed onto this film. The fringes are sharp and without sub-structure; the short-term shot-to-shot stability of the lasing wavelength was obviously good.

For quantitative measurements, a diode array (RECTICON CCPD 1024) was placed along a radial direction of the circular fringes. Since the fringe-separations were becoming constant at positions far away from the centre, measurements were taken on these fringes. Figure 5.15 shows an oscilloscope trace of a fringe pattern recorded with the diode array. Now the mode separation for a 6 mm DFDL can be calculated from the coupled-wave theory and is equal to 18.6 GHz. This single shot measurement clearly shows that the laser was in

Figure 5.14. Typical Fabry-Perot interferometer fringe pattern of DFDL single pulses.

12 shots
superimposed

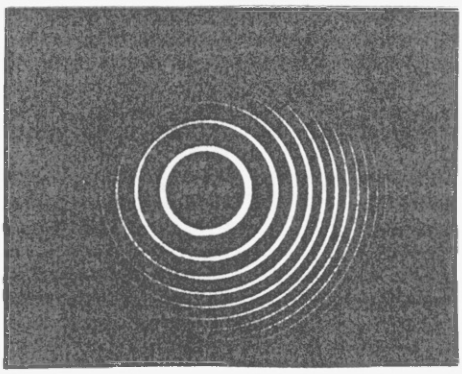


Figure 5.15. Diode-array record of interferometer fringe pattern of a DFDL single pulse.

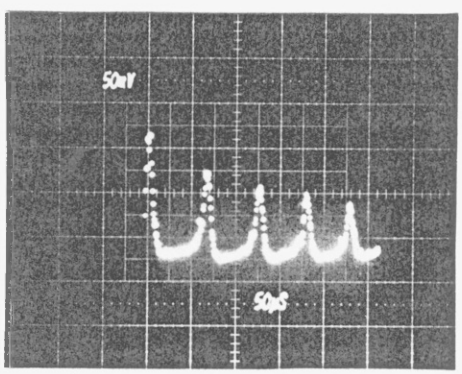
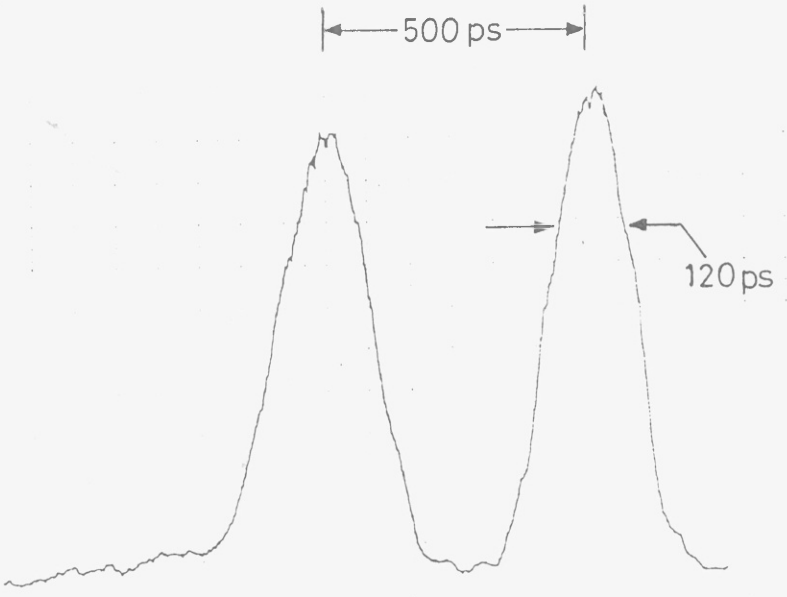
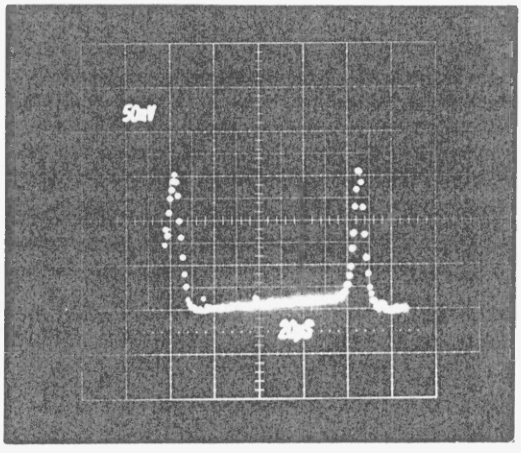


Figure 5.16. Simultaneous measurement of pulse duration and spectral linewidth for a DFDL single pulse.



pulse duration = 120 ps (FWHM)



linewidth = 2.6 GHz (FWHM)

TIME-BANDWIDTH PRODUCT = 0.31

Table 5.2: Simultaneous Measurements of Pulse Duration and Bandwidth

Pulse Duration (ps)	Bandwidth (GHz)	Time-Bandwidth Product
88	3.1	0.28
100	2.9	0.29
108	2.4	0.26
115	2.4	0.28
119	2.6	0.31
154	2.1	0.32
164	2.1	0.34
165	2.1	0.34

single-mode operation. The spectral line of the laser output was smooth and structureless. Quantitative measurements showed that the spectral linewidth of the DFDL (λ = 616 nm) was about 2 to 3 GHz (FWHM).

An important parameter for coherent light sources is the time-bandwidth product. Simultaneous measurements of the pulse duration and the spectral linewidth were performed on the single pulses of the DFDL operated at 616 nm. Typical results are shown in Figure 5.16. At the top is the microdensitometer trace of the streak camera record of the two identical time-delayed pulses. The separation between the pulses, used for the calibration of the timescale, is 500 ps. The duration of the single pulse is 120 ps. The spectral linewidth, recorded with the diode array, can be determined from the oscilloscope trace at the bottom of Figure 5.16. The measured linewidth is 2.6 GHz (FWHM). The two simultaneous measurements imply that the time-bandwidth product in this case has a value of 0.31.

The other results of simultaneous measurements of pulse duration and spectral linewidth are summarized in Table 5.2. The values of the time-bandwidth products were found to be in the range between 0.28 and 0.34. However, due to the lack of a proper calibration of the film density response in the measurement of pulse duration with the streak camera, the accuracy of these results was only ± 30%.

The time-bandwidth product is 0.441 for a transform-limited Gaussian pulse and 0.315 for the sech^2 pulse profile. In the last section, we have shown that the DFDL pulse shape closely resembled these pulse profiles. It can therefore be concluded that the DFDL pulses were indeed very close to being transform-limited.

5.3.5 Other characteristics

Many applications involving coherent sources required the wavelength of the source to be at a specific value, which may not be precisely known beforehand. On some other occasions, it may be necessary for the wavelength to be continuously variable across a certain range. In both cases, a tunable source is required for the exact desired wavelength to be reached. One slight disadvantage of the achromatic pumping arrangement for the DFDLs is that the tunability of the laser is not as versatile as other pumping schemes.

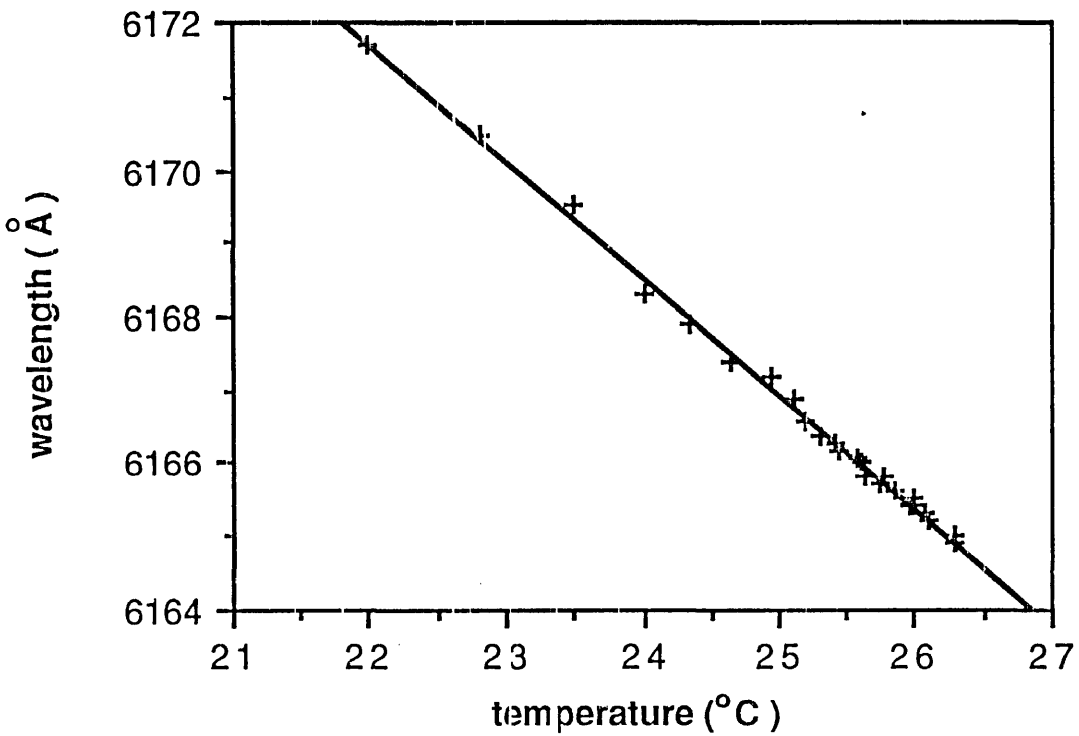
Nevertheless, it is still possible to change the wavelength of the laser by several means with this pumping arrangement.

As shown in Table 5.1 in section 5.2.3, the wavelengths covered with just one holographic grating (2400 lines/mm) range over 56 nm. In each case, the exact wavelength is determined by the refractive index of the solvent mixture. Hence, by using different dye solvents and mixture of solvents, any wavelength within the range can be reached.

In our experiments, the wavelength of the laser output was measured with a one-metre spectrometer (Monospek 1000) with a resolution of 0.1Å. After the operation wavelength had been decided, the composition of the required solvent mixture could be calculated. The exact volume of the required mixture put into the dye circulation system was noted down. The wavelength of the laser could then be checked with the spectrometer which had been calibrated with a He-Ne laser at 6328 Å. Any difference between the measured wavelength and desired wavelength was then noted. Knowing the volume and the refractive index of the mixture of solvents in the system, it would then be possible to calculate the amount of one of the solvents required to be added to reach the desired wavelength. It was found that the laser wavelength can be changed to within 2 Å of the aimed value using this simple procedure only once.

If the refractive indices of the solvents are dependent on temperature, then tuning can be achieved by controlling the temperature of the dye solution. We investigated the dependence of wavelength on the temperature of the solvent-mixture of methanol and ethanol (50%/50% mixture by volume). The laser dye used was rhodamine B of concentration 2.4×10^{-3} M). The wavelength of the DFDL output was measured with the spectrometer, whereas the temperature of the dye solution was recorded with a thermometer, which could be read with a resolution of 1/40 of a degree Centigrade. Figure 5.17 illustrates the dependence of laser wavelength on temperature. The gradient of the best fitted straight line is - 1.94 Å/°C, indicating that the laser can be stabilized to within 1 Å if the temperature of the dye solution is maintained to within 0.5°C. The possibility of tuning is also illustrated with this graph. If the temperature of the dye solution can be varied in a controlled fashion, the wavelength of the laser can be tuned at a rate of 1.94 Å/°C.

Figure 5.17 Dependence of laser wavelength on temperature



In fact, by studying the wavelength tuning of a distributed feedback dye laser with the variation of solvent temperature, the refractive-index dependence on temperature $\left(\frac{d\eta}{dT}\right)$ of the solvent can be measured [26]. For our achromatic pumping arrangement, the wavelength of the laser is related to the refractive index of the mixture of solvents by

$$\lambda = \eta/N, \tag{5.4}$$

where N is the number of lines per unit length for the grating. Differentiation with respect to temperature yields

$$\frac{d\lambda}{dT} = \frac{1}{N}\frac{d\eta}{dT} . \tag{5.5}$$

For our holographic grating, N equals 2180 lines/mm. The value of $\frac{d\eta}{dT}$ (at 24°C) for this mixture of solvents is therefore equal to $-4.2 \times 10^{-4}/^{\circ}C$. This agrees well with the tabulated value for both methanol and ethanol ($-4.1 \times 10^{-4}/^{\circ}C$) [27].

Various research workers have found that DFDLs have much lower ASE level [25,28] compared with other pulsed dye laser systems. Although no systematic study was conducted of the characteristics of the ASE from our DFDL, there were some general observations worth mentioning. Basically, when an appropriate dye concentration was used and the laser was properly aligned, the ASE level would be low. The choice of dye was also another important consideration. In general, a low level of ASE was a good indication that the laser was working properly.

The polarization of the dye laser beam in the transverse pumping arrangement is determined mainly by the polarization of the exciting laser beam, the relative orientation of the transition moments in the dye molecules from pumping and laser transitions, and the rotational diffusion-relaxation time. The latter is determined by solvent viscosity, temperature and molecular size. For a conventional resonator, the polarization can also be affected by resonator polarizing elements such as Brewster windows.

Among the distributed feedback dye lasers investigated (see Table 5.1), the coumarine dye in methanol/ethanol solutions was the only system which produced depolarized output. In the other systems, the output beam was strongly polarized in the direction perpendicular to

the lines of the holographic grating (i.e. parallel to the plane containing both the excitation UV beam and the dye laser output beam). Virtually no laser signal was detected in the other polarization direction. As for the coumarine system, when a polarizing filter was placed in the laser beam, the signal amplitude, monitored with an oscilloscope, fluctuated by an order of magnitude over fifty consecutive shots. This behaviour was independent of the orientation of the polarizing filter. However, when the filter was removed, the stability of the total output signal became quite good (~ ± 12%).

5.3.6 Comparisons of experimental and theoretical results

The rate equation models described in Chapter 3 and Chapter 4 were used to obtain computer simulations of the output characteristics of the XeCl pumped DFDL. The following parameters for rhodamine B were used in the calculations: $\sigma_p = 5.2 \times 10^{-17} cm^2$, $\sigma_e = 1.2 \times 10^{-16} cm^2$, $\sigma_a = 0.7 \times 10^{-16} cm^2$, $\tau = 3.2$ ns, $\lambda_0 = 616$ nm, $\lambda_p = 308$ nm, $\eta = 1.35$, $V = 1$, $S = 10^4$, $N = 1.2 \times 10^{18} cm^{-3}$ (i.e. 2.0×10^{-3} M), $\ell = 6$ mm, $b = 0.25$ mm. The meanings of the symbols can be found in section 3.2. A Gaussian pump pulse with a duration of 6 ns (FWHM) was assumed.

Figure 5.18 shows the dependence of DFDL pulse energy on the pumping rate calculated with the undercoupled DFDL model. Figure 5.19 shows the pulse duration dependence. Figures 5.20 and 5.21 show the corresponding computer results calculated with the overcoupled DFDL model.

These theoretical results are compared with an experimental result obtained with our XeCl pumped DFDL in Table 5.3. As expected, the single-pulse duration calculated with the undercoupled DFDL model is longer that what it really is since the self Q-switching effect is not included in this approximation. The computer results presented in Chapter 4 indicated that the self Q-switching effect should produce a further pulse-shortening of approximately 40%. The single-pulse duration obtained with this model is 155 ps (with the second pulse at threshold); therefore, a 40% reduction will give an expected value of pulse duration at 93 ps.

Figure 5.18 Dependence of first-pulse energy on pumping rate

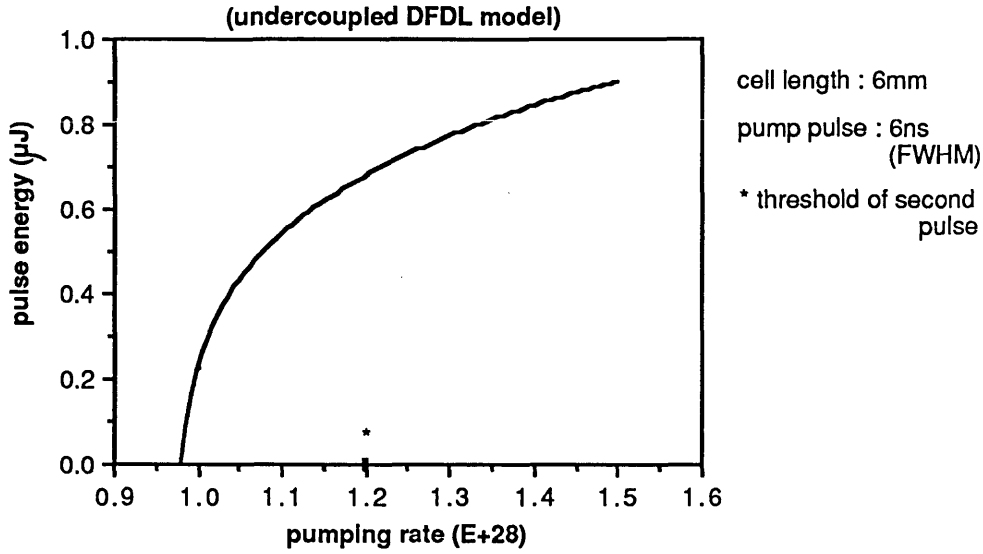


Figure 5.19 Dependence of first-pulse duration on pumping rate

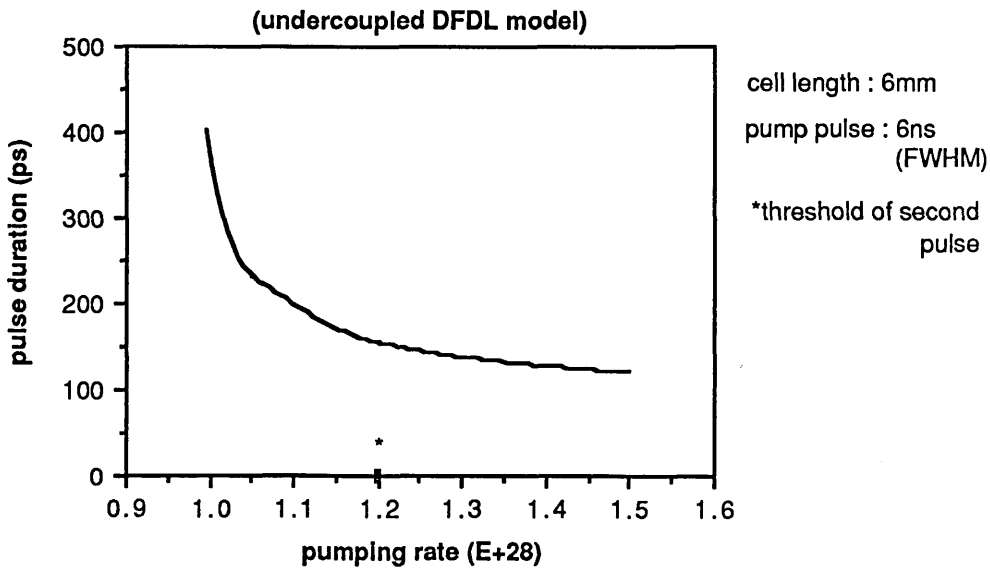


Figure 5.20 Dependence of first-pulse energy on pumping rate

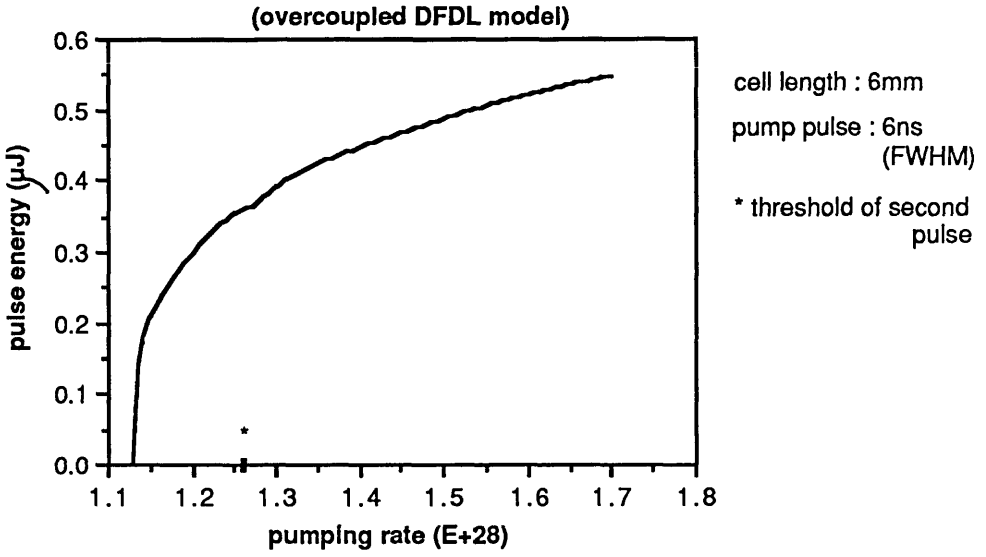


Figure 5.21 Dependence of first-pulse duration on pumping rate

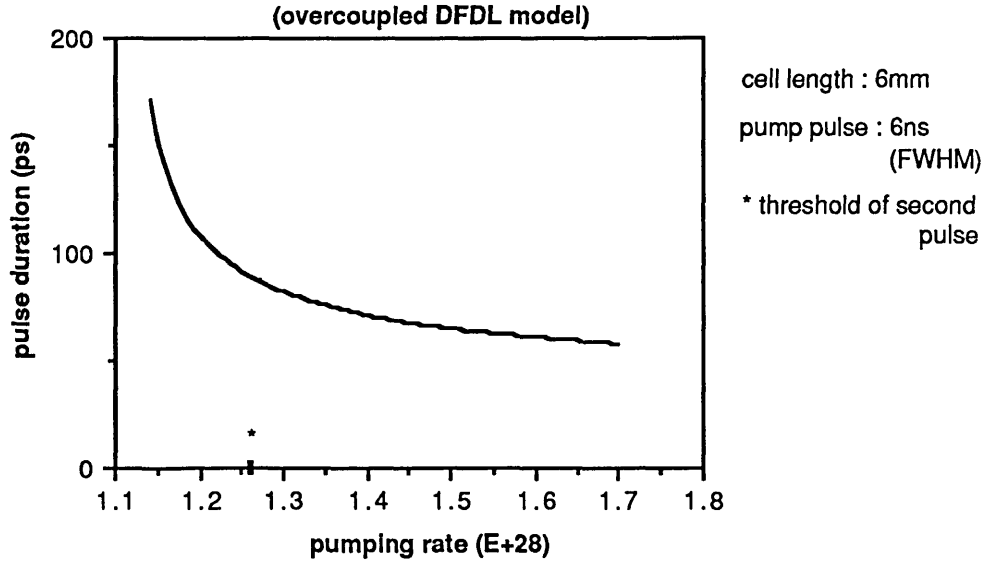


Table 5.3 : Comparison of Experimental and Theoretical Results

	Theoretical Results		Experimental Result
	Undercoupled DFDL Model	Overcoupled DFDL Model	
Threshold Pump Intensity	320 kW cm^{-2}	360 kW cm^{-2}	1200 kW cm^{-2}
Single Pulse Operation Range (Normalized to threshold pump power)	0.22	0.12	0.25
Single Pulse Duration	155 ps	89 ps	88 ps

+ Second pulse at threshold

This is consistent with the calculation from the overcoupled DFDL model and the experimental results.

The experimental threshold pump intensity was about three and a half times larger than the theoretical values. The single-pulse operation range was also larger than the theoretical predictions.

In general, the experimental results show good qualitative agreement with the computer solutions of the rate equation models.

5.4 Conclusion

We have described the basic characteristics of a XeCl pumped distributed feedback dye laser. It was discovered that various properties of the UV pumping beam could influence the DFDL output. It was found that the single pulses generated with this DFDL were effectively transform-limited. The DFDL beam also had excellent transverse beam quality and the propagation of the laser beam was successfully analysed with the theory of the fundamental Gaussian beam. The DFDL beam was shown to be nearly diffraction-limited.

The operation of the laser system with rhodamine B in methanol/ethanol solution was found to produce high quality stable single pulses of approximately 100 ps duration at 616 nm. The laser beam was found to be strongly polarized with a low ASE background level. It was also demonstrated that the laser wavelength could be tuned to within 2 Å of the desired wavelength of 6160 Å by a very simple procedure. The dependence of wavelength on temperature was also investigated. With a proper temperature-controlled system, fine tuning and wavelength stabilization should be possible.

The temporal and energy characteristics observed in experiments were compared with the computer solutions of the rate equation models described in Chapter 3 and Chapter 4. Good qualitative agreement was found.

In the following chapter, we shall describe a system used to amplify the DFDL output at the wavelength of 616 nm to produce reasonably intense coherent pulses with power up to 4 MW. Frequency-doubling of these visible pulses was applied to generate 0.5 MW UV radiation at 308 nm.

CHAPTER 6

PICOSECOND UV PULSE GENERATION

6.1 Introduction

Ultrashort laser pulses allow temporal studies of fundamental physical, chemical and biological processes via the interactions of light with matter. Some of these studies required ultraviolet (UV) radiation. Distributed feedback dye laser (DFDL) systems, which can generate ultrashort light pulses throughout the entire visible spectrum, can provide the basis for the generation of ultrashort UV pulses via the process of second-harmonic generation. In an excimer laser pumped DFDL system, only a small amount of the pump energy is required to drive the oscillator, leaving most of the energy to pump the amplifiers. Amplification of the DFDL oscillator output signal is needed to reach the high level of intensity required for the nonlinear process of frequency-doubling. The oscillator-amplifier system to be described operated at 616 nm. This wavelength was chosen because the second harmonic at 308 nm falls within the gain bandwidth of the XeCl excimer system. This allowed the possibility of amplifying the ultrashort UV pulses, obtained from frequency-doubling, in a XeCl gain module, from which very intense ultrashort UV pulses could be generated. Apart from this, the excimer laser pumped DFDL system to be described should be suitable to generate radiation at any wavelength in a very wide range in the UV region of the spectrum.

The generation of high-energy pulses can be realized with a system with a combination of a master oscillator and multi-stage power amplifiers. In an oscillator-amplifier system, pulse width, beam divergence and spectral linewidth are primarily determined by the oscillator whereas pulse energy and power are determined by the amplifiers. Operating a conventional oscillator at relatively low energy levels generally reduces beam divergence and spectral width. In the case of the picosecond distributed feedback dye laser, the DFDL oscillator must be operated within a certain range of energy levels because the process of generation is based on controlled

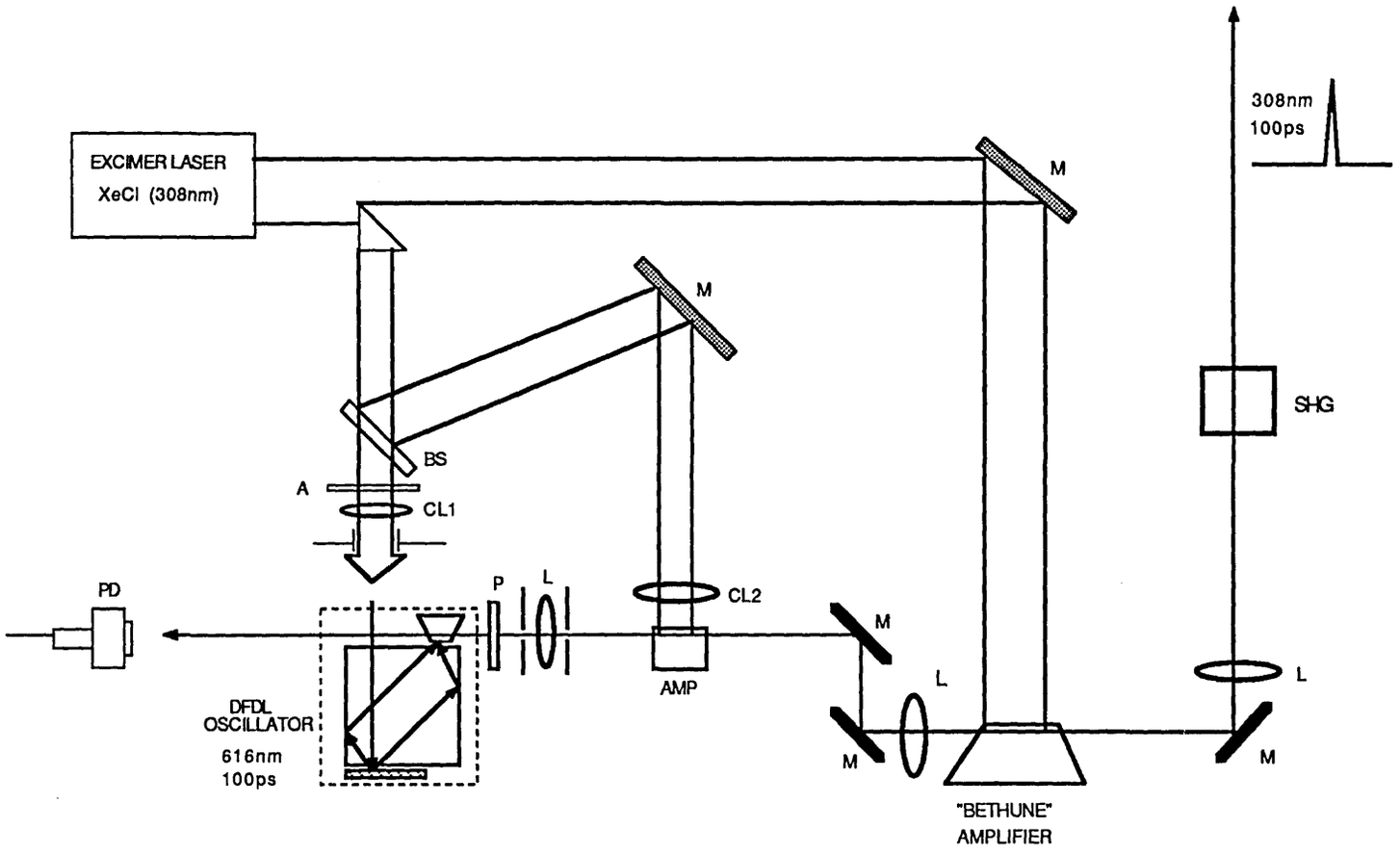


Figure 6.1 Schematic diagram of the laser system for the generation of ultrashort UV pulses

(BS: beam splitter, A: UV attenuator, CL: cylindrical lens, P: polarizaing filter, PD: photodiode, L: spherical lens, M: mirror, AMP: amplifier, SHG: second-harmonic crystal.)

resonator transients. The energy of a single pulse from the oscillator is usually very low indeed and power amplifiers are required to produce high-energy pulses.

In this chapter we shall describe an excimer laser pumped oscillator-amplifier system which produced single pulses of peak power up to 4 MW at 616 nm. The intense visible beam could be frequency-doubled to obtain ultrashort UV pulses at 308 nm. A schematic diagram of the laser system for the generation of ultrashort UV pulses is shown in Figure 6.1.

6.2 Amplification of DFDL Pulses

The amplifier chain for our excimer pumped laser system consisted of only two stages — a conventional transversely pumped pre-amplifier and a "Bethune" prism amplifier [29] which was transversely pumped from four directions.

The conventional pre-amplifier was made up of a rectangular fused silica dye cell (2 cm in length) containing a rhodamine dye solution. A cylindrical lens was used to focus the UV pump beam onto the front inner surface of the cell to form a focal line. This focal region of the dye solution was strongly pumped to generate population inversion. The output beam from the DFDL oscillator experienced gain in passing through this region and its power was amplified.

The timing of the arrival of the DFDL beam at the amplifier was found to have a strong effect on the gain. This is mainly due to the short storage time of the dye system. Since the lifetime of the upper lasing level is only about 3 ns, the population inversion accumulated cannot be stored for much longer than this lifetime. Moreover, due to the high single-pass gain of the amplifier, the spontaneous emitted radiation will be strongly amplified by stimulated emission as it propagates through the amplifying medium; thus the available gain for the laser pulse will be further depleted. Hence the gain of the amplifier varies with time. It was therefore necessary to determine experimentally the exact time of the highest gain. One way of doing this was to monitor the temporal evolution of the ASE signal from the amplifier since the peak of this signal would be close to the peak of the gain of the amplifier. The timing of the DFDL pulse was then accordingly adjusted to coincide with the time of

maximum gain by varying the optical delay of the amplifier pump pulse. This method was found to be very effective in determining the best length of the optical delay-line (~ 2.5 ns) for the amplifier UV pump pulse.

The ASE of the amplifier, though useful in the above consideration, was basically a parasitic effect which competed with the signal to be amplified. Appropriate measures had to be taken to reduce any undesirable effects caused by ASE. Although the level of ASE could be reduced by operating at a low pumping rate, the gain of the system however would be decreased as a result. Nevertheless, it was important that the ASE of the amplifier did not get reflected back into the gain path. This could be ensured by tilting the dye cell so that the side windows were not perpendicular to the focal line of the pump beam.

For two important reasons, the focal line of the pump beam was also set at a slight angle to the optical path of the DFDL beam. Firstly, this could reduce the ASE signal entering the next amplifier stage. Secondly, perhaps more importantly, the ASE signal from the pre-amplifier should not be allowed to interfere with the laser action in the DFDL oscillator. Otherwise the characteristics of the output pulse from the laser would be altered. Another way of reducing this undesirable interaction was by increasing the spatial separation between the oscillator and the pre-amplifier. Since ASE occurred in a relatively large beam angle, a large separation would effectively cut down the ASE signal entering the oscillator. Additionally, the ASE signal from the amplifier would take a longer time to arrive at the oscillator, which might have become "inactive" at this stage.

Several dyes were used in the pre-amplifier for the amplification of the DFDL pulses at 616 nm. These included rhodamine 101, sulfo-rhodamine B and rhodamine B (Lambda Physik dyes). A wide range of concentrations were tried in each case. Rhodamine 101 was found to produce the highest gain. No advantage, however, was found in replacing rhodamine B in the oscillator with the other dyes.

In fact, there was an advantage in using the combination of rhodamine B in the oscillator and rhodamine 101 in the pre-amplifier. Since the output spectrum of the ASE from the oscillator with rhodamine B peaks at 600 nm whereas the main absorption band of rhodamine 101 is located very close to 600 nm (at 580 nm), the

rhodamine 101 dye in the pre-amplifier will in fact absorb the radiation in the short wavelength region of the ASE from the oscillator.

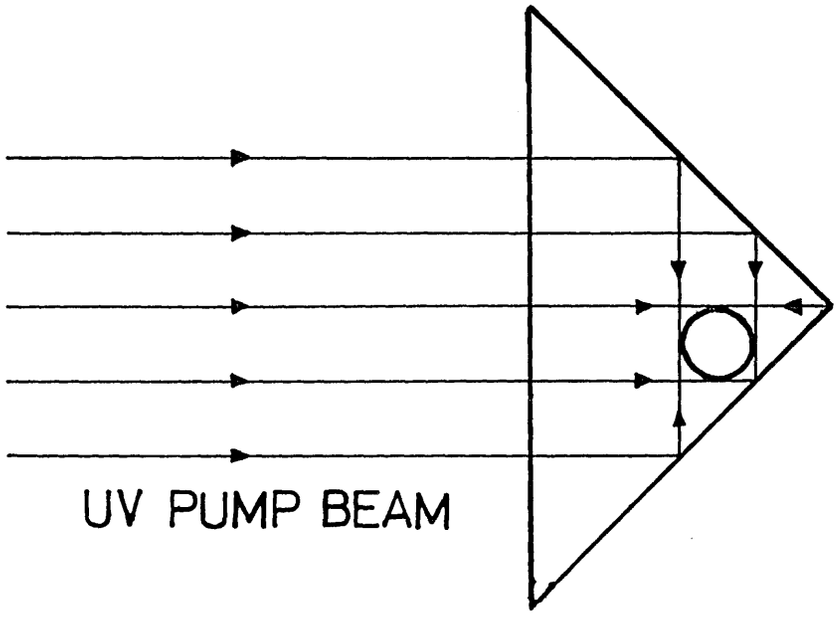
Theoretically, a heavily saturated amplifier is most effective in converting the stored energy, derived from the optical excitation by the pumping beam, into the amplified signal. In the case of ultrashort pulse amplification, the amplifier will be more saturated if the input energy density is higher. Hence, the diverging DFDL beam had to be focused into a small beam to pass through the amplifier dye cell. The UV pump beam was also focused into a focal line with a cylindrical lens (f/ℓ 150 mm) so that the coupling between the pump beam and the DFDL beam could be optimized. The concentration of the dye in solution was chosen so that the penetration depth matched the DFDL beam size at the amplifier dye cell; this was determined experimentally by trying a wide range of dye concentrations.

A 4×10^{-4} M solution of rhodamine 101 in methanol was used in the pre-amplifier. The effective radius of the DFDL beam at the amplifier cell was about 300 μm. The energy of the pump pulse was approximately 5 mJ. The energy of the DFDL pulse after this stage of amplification was measured with a calibrated joulemeter (GEN-TEC ED-100A) in conjunction with an oscilloscope. It was found to be about 35 μJ, corresponding to a gain factor of about 80. The energy density was just a few times above the saturation energy density.

It is well-known that the pulse shape may change in passing through an amplifier. This occurs simply because the leading edge of the pulse stimulates the release of some of the stored energy and reduces the population inversion, thereby causing the trailing edge to see a different inverted population. It was rather difficult to assess the degree of pulse-shape distortion on the DFDL pulse since the pulse shape of the oscillator output could not be determined due to the small amount of energy being not high enough for the streak camera measurement. However, the shape of the DFDL pulse after the pre-amplifier was determined (see Figure 5.10). It was generally still quite symmetric and close to the Gaussian pulse profile, indicating that it might not have been distorted by any significant amount.

A dye cell of the type described by Bethune [29] was used in the second amplifier stage. The cell was based on a standard 45° right-angle, fused-silica prism with a 35 mm long bore of 4 mm diameter,

Figure 6.2. End view of the "Bethune" prism amplifier dye cell.



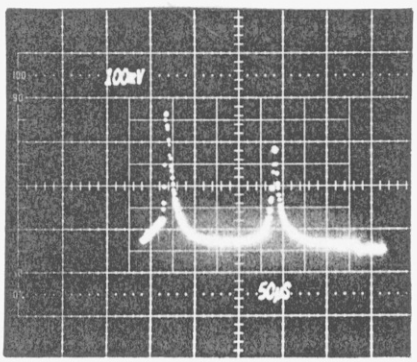
drilled parallel to the rectangular faces of the prism (Figure 6.2). A dye solution flowed through this hole. An unfocused UV pump beam entered the prism from the left in Figure 6.2, with a beam thickness equal to four times the diameter of the hole in the prism. Four different regions of the pump beam would end up pumping the cylinder of the dye solution from four different directions symmetrically. This could provide relatively homogeneous pumping.

Rhodamine 101 in methanol solution was used in the "Bethune" amplifier. In fact, the concentration of the dye solution has a large effect on the pumping homogeneity in the transverse direction since the penetration depth of the pump beam depends on the concentration. Again, the ASE signal from the pumped amplifier could be used to assess the gain distribution of the amplifier across the transverse direction for different dye concentrations.

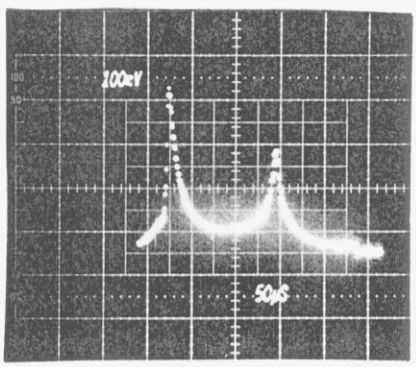
The pumping from the oscillator and the pre-amplifier were blocked so that only the Bethune amplifier was pumped. A diffuse filter was placed against the exit window of the Bethune cell. The homogeneity of the ASE could in fact be seen with the naked eye. A quantitative assessment was conducted by focusing the illumination at the filter with a spherical lens onto a diode array (RETICON CCPD 1024), which was placed along a radial direction of the circular image. Figure 6.3 shows the oscilloscope traces of the transverse distribution of the ASE signal for dye concentrations over the range 0.75×10^{-4} to 1×10^{-3} M. The lopsidedness in the signals is attributed to the measuring equipment. The basic features, however, are clear enough. A ring-shaped ASE pattern was seen from the end view of the dye cell if the concentration of the dye solution was too high. For low concentration, the ASE signal peaked at the centre. However, the magnitude of the signal was lower. From the patterns in Figure 6.3, it can be deduced that the best concentration is about 2×10^{-4} M. Experimentally, this concentration was also found to produce relatively high gain and the amplified DFDL beam had reasonably good beam quality.

With a 2×10^{-4} M solution of rhodamine 101 in methanol in the Bethune amplifier cell, the pre-amplified DFDL beam was directed to pass through this amplifier with a diameter of approximately 2.5 mm. Larger beam diameter would lead to a significant deterioration in the output beam quality. Diffraction effects on the wings of the Gaussian-like transverse beam profile seemed to be the main cause of

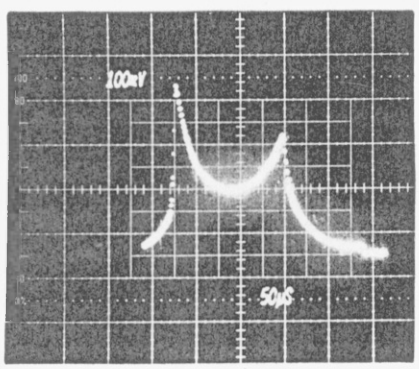
Figure 6.3. Transverse distribution of ASE signal intensity of Bethune amplifier.



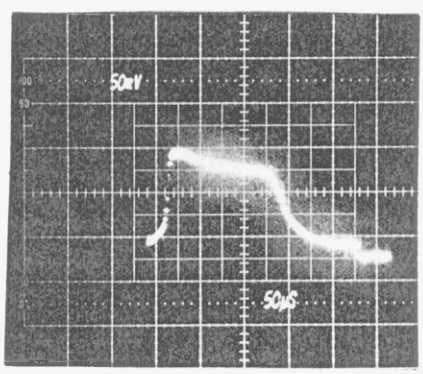
1.0×10^{-3} M



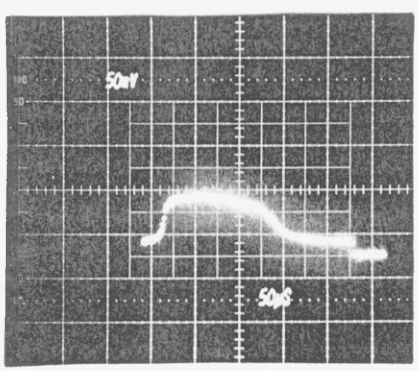
6.0×10^{-4} M



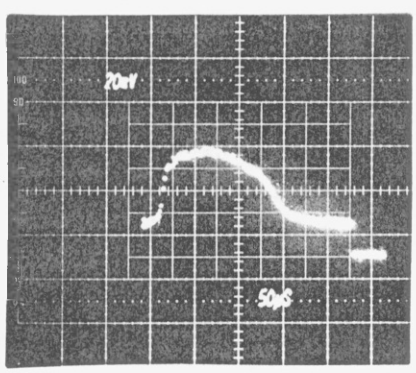
4.0×10^{-4} M



2.0×10^{-4} M



1.0×10^{-4} M



7.5×10^{-5} M

beam deterioration for a large beam. The synchronization of the UV pump pulse and the DFDL pulse at this amplifier was also determined by monitoring the ASE signal of the amplifier. It was found that the UV pump pulse had to arrive quite early at the amplifier cell. This was because the pump power per unit volume for this amplifier was much smaller than for the pre-amplifier so that the build-up of gain and hence ASE was slower.

The energy of the UV pump pulse entered into the Bethune amplifier was about 32 mJ. The corresponding energy of the amplified DFDL pulse, measured with a joulemeter (GEN-TEC ED-100A), was approximately 350 μJ. This is equivalent to a gain factor of 10.

The gain characteristics of a laser amplifier for short pulses have been analysed theoretically by Frantz and Nodvik [30]. Consider that the duration of the pulse to be amplified is short relative to the fluorescence lifetime, and the process of pulse amplification is fast compared with the pumping rate. The amplification process is then based on the energy stored in the upper laser level prior to the arrival of the input signal; the effect of fluorescence and pumping can be ignored. For a four-level laser system, the rate of change of population inversion ($\partial n/\partial t$) can then be described by

$$\frac{\partial n}{\partial t} = - \frac{\sigma_e c}{\eta} nq. \qquad (6.1)$$

The meanings of the symbols are the same as those in section 3.2.

The growth of a radiation pulse traversing a medium with an inverted population is described by

$$\frac{\partial q}{\partial t} = \frac{\sigma_e c}{\eta} nq - \frac{\partial q}{\partial x}, \qquad (6.2)$$

where x is the position in the amplifier along the direction of pulse propagation. The rate at which the photon density changes in a small volume of the material ($\partial q/\partial t$) is equal to the net difference between the generation of photons by the stimulated process (first term on the right) and the flux of photons which flows out from that region ($\partial q/\partial x$). These two nonlinear, time-dependent photon-transport equations therefore account for the effect of the radiation on the active medium and vice versa. These differential equations were solved by Frantz and Nodvik for a square input pulse. They obtained an

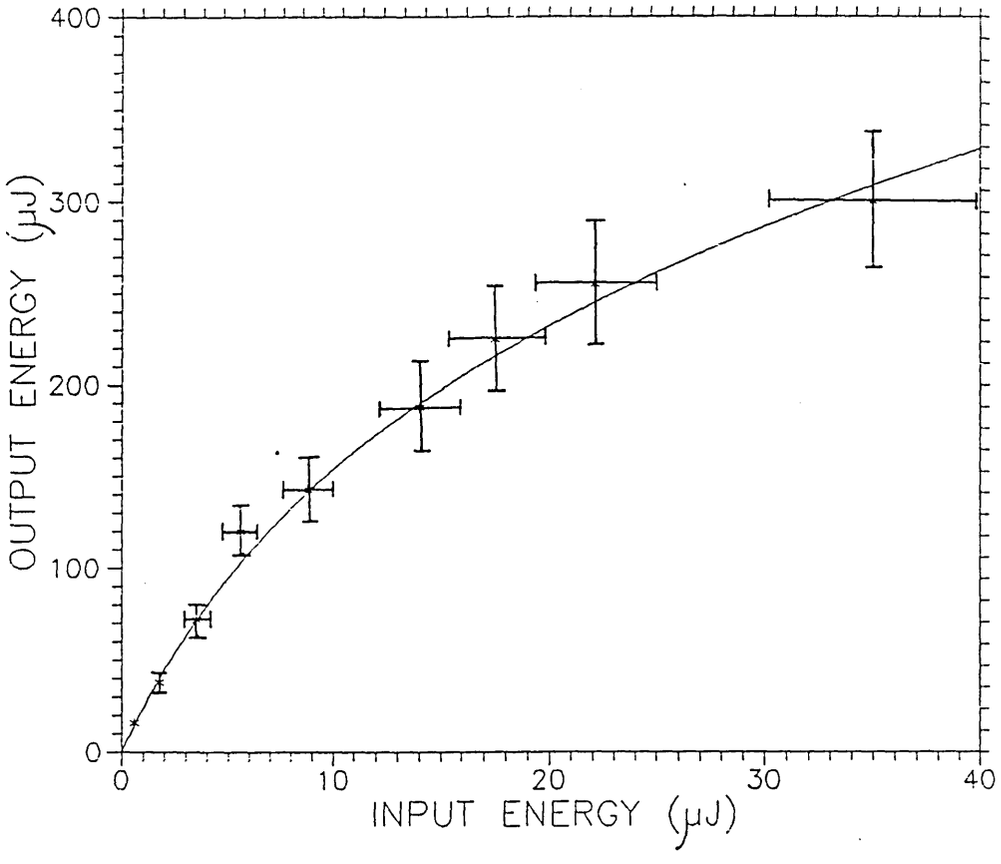


Figure 6.4. Gain saturation characteristics of Bethune amplifier.

expression which relates the output energy density (E_{out}) to the input energy density (E_{in}), the saturation energy density (E_s) and the small-signal single pass-gain (G_0):

$$E_{out} = E_s \ln\left\{1 + G_0\left[\exp\left(\frac{E_{in}}{E_s}\right) - 1\right]\right\}, \qquad (6.3)$$

where E_s is given by

$$E_s = \frac{h\nu}{\sigma_e}, \qquad (6.4)$$

where $h\nu$ is the photon energy and σ_e is the stimulated emission cross-section.

Although the DFDL pulse had a "Gaussian-like" profile, the gain saturation characteristics described by equation (6.3) were found to be a reasonable approximation for the gain characteristics of the Bethune amplifier.

By placing different calibrated neutral density filters in the path of the input DFDL beam before the Bethune amplifier, the corresponding output pulse energies after the amplifier were measured with a joulemeter. The output energy can be plotted against the input energy as shown in Figure 6.4. Equation (6.3) may be used to fit a curve to the data points. The values of the saturation energy and the small-signal gain are varied until a suitable pair of values is found to generate the best fitted curve. The curve in Figure 6.4 implies that the small signal gain was about 26 and the saturation energy was 150 μJ. Given that the diameter of the beam was approximately 2.5 mm, the saturation energy density would be about 3 mJ/cm^2. This is consistent with the theoretical value given by equation (6.4).

6.3 Generation of Ultrashort UV Pulses

6.3.1 The principles of second harmonic generation

Optical second-harmonic generation is an important nonlinear optical process which has found wide applications as a means to generate shorter wavelength radiation from coherent light sources.

With a technique called phase-matching, a coherent laser beam of frequency ω can be efficiently converted into a beam of radiation at the doubled frequency 2ω, using a nonlinear crystal.

The intense DFDL pulses obtained after the two-stage amplification have enough power to generate coherent ultrashort UV pulses via the process of second-harmonic generation. Experimental demonstration of this will be described later. We shall first outline the basic theoretical background of this important nonlinear process. A full treatment of the theory of second-harmonic generation can be found in most textbooks on quantum electronics.

The electromagnetic field of a light wave propagating through a medium exerts forces on the loosely bound, outer or valence electrons, which will consequently be displaced from their normal orbits. This perturbation creates electric dipoles whose macroscopic manifestation is the polarization. If the field strength is small, this polarization will be proportional to the electric field. In the case of a very high field, the amplitudes of the electric dipoles cannot faithfully reproduce the sinusoidal electric field that generates them. The system responds nonlinearly. As a result, the distorted re-radiation wave contains frequencies different from that of the original wave. Second harmonic generation is one of these nonlinear processes.

In this nonlinear process, two "fundamental" waves, which can be derived from a single laser beam, at frequency ω are coupled together in a nonlinear medium to produce a second-harmonic wave at twice the original (fundamental) frequency 2ω. In general, the induced polarization vector $\underline{P}$ can be expressed in terms of a power series expansion of the applied electric field vector $\underline{E}$:

$$\begin{aligned}\underline{P}(\omega_r) &= \underline{\underline{\chi}}'(\omega_r) \cdot \underline{E}(\omega_r) \\ &+ \sum_{s,t} \underline{\underline{\chi}}^{2}(\omega_r = \omega_s + \omega_t) : \underline{E}(\omega_s)\underline{E}(\omega_t) \\ &+ \sum_{s,t} \underline{\underline{\chi}}^{3}(\omega_r = \omega_s + \omega_t + \omega_p) : \underline{E}(\omega_s)\underline{E}(\omega_t)\underline{E}(\omega_p) \\ &+ \ldots . \end{aligned} \tag{6.5}$$

where χ^n are the susceptibility tensors of the n^{th} order. The values of the tensor coefficients are functions of the frequencies of the interacting waves denoted by subscripts r,s,t,p. For small field strength, the polarization is linear and proportional to the electric field $\underline{E}$ and is accounted for by the polarizability tensor $\underline{\underline{\chi}}'$.

The $\underline{\underline{\chi}}^2$ term in equation (6.5) is responsible for second-harmonic generation. It is a third rank tensor having 27 components. However, for the type of crystals used for second-harmonic generation, many of the components of $\underline{\underline{\chi}}^2$ are zero or equal to other components of the tensor, as a result of crystal symmetry. Furthermore, for these crystals there is usually one predominant coefficient associated with a single light propagation direction which yields maximum harmonic power. In component form, the induced nonlinear polarization associated with second-harmonic generation can be written as

$$\left[P_{NL}^{2\omega}\right]_i = \sum_{j,k} \chi_{ijk} E_j^{\omega} E_k^{\omega} , \tag{6.6}$$

where the subscripts i, j and k refer to the Cartesian co-ordinates of the crystal.

The wave propagation in the crystal is governed by the wave equation (derived from Maxwell's equations) taking into account the nonlinear polarization:

$$\nabla^2 \underline{E} = \mu_0 \sigma \frac{\partial \underline{E}}{\partial t} + \mu_0 \varepsilon \frac{\partial^2 \underline{E}}{\partial t^2} + \mu_0 \frac{\partial^2}{\partial t^2} \underline{P}_{NL} . \tag{6.7}$$

It can be solved with some simplifications corresponding to realistic experimental conditions. All three interacting waves (i.e. the two fundamental waves and the second-harmonic wave) are assumed to be plane waves propagating in the z direction so that $\frac{\partial}{\partial y} = \frac{\partial}{\partial z} = 0$. It is also assumed that the variation of the complex field amplitudes with z is small so that

$$k^{2\omega} \frac{dE^{2\omega}}{dz} >> \frac{d^2E^{2\omega}}{dz^2} \tag{6.8}$$

and

$$k^{\omega} \frac{dE^{\omega}}{dz} >> \frac{d^2E^{\omega}}{dz^2} . \qquad (6.9)$$

The medium is usually transparent at 2ω so that there is no absorption at the second-harmonic wavelength.

If the amount of power lost by the input beam (as a result of conversion to 2ω) is negligible so that $dE^{\omega}/dz \simeq 0$ (small-signal approximation), the growth of the second-harmonic field amplitude will be described by

$$\left(\frac{dE^{2\omega}}{dz}\right)_i = - i\omega \sqrt{\frac{\mu_0}{\varepsilon}} \; d'_{ijk} \; E^{\omega}_j \; E^{\omega}_k \exp(i\Delta kz), \qquad (6.10)$$

where

$$\Delta k = k^{2\omega} - 2k^{\omega}, \qquad (6.11)$$

and d'_{ijk} is the effective nonlinear susceptibility tensor. By noting that there is no second-harmonic input, equation (6.10) can be solved for a crystal of length L and the conversion efficiency $\left(\frac{P^{2\omega}}{P^{\omega}}\right)$ can be written as [31]

$$\frac{P^{2\omega}}{P^{\omega}} = 2\left(\frac{\mu_0}{\varepsilon_0}\right)^{3/2} \frac{\omega^2 (d'_{ijk})^2 L^2}{\eta^3} \left(\frac{P^{\omega}}{\text{Area}}\right) \frac{\sin^2\left(\frac{\Delta kL}{2}\right)}{\left(\frac{\Delta kL}{2}\right)^2} , \qquad (6.12)$$

where P^{ω} and $P^{2\omega}$ are the fundamental input power and the second-harmonic output power, respectively.

The conversion efficiency has a factor described by $\frac{\sin^2(\Delta kL/2)}{(\Delta kL/2)^2}$, which has the same mathematical form as the Fraunhofer diffraction pattern of a single slit. In fact, the origin of this factor is also connected with interference effects. Basically, second-harmonic generation may be viewed as a two-step process — the generation of second-harmonic polarization wave and the transfer of polarization energy into second-harmonic electromagnetic wave. The second-harmonic polarization wave of frequency 2ω generated in the nonlinear medium is driven by the fundamental wave. Its phase velocity and wavelength in the medium are therefore determined by the

refractive index for the fundamental wave (η^{ω}). Hence the wavelength of the polarization wave is given by $\lambda_p = c/2\nu_1\eta^{\omega}$, where $\nu_1 = \omega/2\pi$. The energy of this polarization wave is continuously transferred to the electromagnetic wave (at frequency 2ω) which propagates freely inside the medium. The wavelength of this electromagnetic wave is determined by the refractive index of the second-harmonic frequency ($\eta^{2\omega}$) and is given by $\lambda^{2\omega} = c/2\nu_1\eta^{2\omega}$. There will be efficient energy transfer from the fundamental wave to the harmonic wave only if the second-harmonic polarization and electromagnetic waves remain in phase. Otherwise, there will be a certain degree of destructive interference and some energy will flow back to the fundamental from the second harmonic causing a severe limit on the conversion efficiency.

The phase mismatch parameter (Δk) can be expressed as

$$\Delta k = \frac{2\omega}{c}(\eta^{2\omega} - \eta^{\omega}). \tag{6.13}$$

For a non-zero Δk, only a finite length of the medium will be useful in the harmonic generation process. This length, termed the coherence length, is given by

$$\ell_c = \frac{\pi c}{\omega(\eta^{2\omega} - \eta^{\omega})}. \tag{6.14}$$

If Δk is equal to zero, the coherence length will be infinite and the conversion efficiency will then vary quadratically with crystal length (in the small-signal approximation). This is known as the phase-matching condition.

The phase-matching condition for second-harmonic generation can be satisfied by taking advantage of the natural birefringence of anisotropic crystals. In negative uniaxial crystals such as ADP (ammonium dihydrogen phosphate), the refractive index for the extraordinary wave is smaller than that of the ordinary wave for a given wavelength (except along the optic axis where they are equal). For each of these waves, the refractive index increases with wavelength in the normal dispersion region. Hence by arranging the input fundamental to be an ordinary wave, there exists a propagation direction along which the generated second-harmonic extraordinary wave will see the same refractive index and propagate with the same phase velocity as the fundamental, i.e.,

$$\eta_e^{2\omega}(\theta_m) = \eta_o^{\omega}, \tag{6.15}$$

where θ_m, the phase-matching angle, is the angle between the direction of propagation and the optic axis. The subscripts e and o denote extraordinary wave and ordinary wave, respectively.

The nonlinear optical tensor of the crystal must be considered in choosing the azimuthal angle for the propagation direction. For example, in ADP crystals, the nonlinear polarization in component form is given by

$$\begin{aligned} P_x^{2\omega} &= 2d_{14}E_z^{\omega}E_y^{\omega} \\ P_y^{2\omega} &= 2d_{14}E_z^{\omega}E_x^{\omega} \\ P_z^{2\omega} &= 2d_{36}E_x^{\omega}E_y^{\omega}, \end{aligned} \tag{6.16}$$

where d_{14} and d_{36} are optical tensor elements of the crystal and x,y,z are in the co-ordinate system of the crystal with z being the direction of the optic axis. If the fundamental beam is an ordinary wave, then E_z^{ω} will be zero. Hence the only non-zero polarization component given by equation (6.16) is $P_z^{2\omega}$. The component of $P_z^{2\omega}$ normal to the direction of propagation is therefore given by $2d_{36}E_x^{\omega}E_y^{\omega}\sin\theta_m$. For a single input beam, this value will be maximum if the product $E_x^{\omega}E_y^{\omega}$ is maximized. This implies that $\underline{E}^{\omega}$ must be in the direction such that $E_x^{\omega} = E_y^{\omega} = E^{\omega}/\sqrt{2}$. Hence the best azimuthal angle for $\underline{E}^{\omega}$ is 45°.

The discussions above outline the most basic requirements for efficient second-harmonic generation in nonlinear crystals. Phase-matching is the most important consideration. Nevertheless, there are also other practical considerations. If phase-matching is accomplished at an angle θ_m other than 90°, there will be a small angle between the direction of power flow (the Poynting vector) of the fundamental and the second-harmonic waves. This angle (ρ) has the effect of limiting the effective crystal volume over which harmonic generation can take place. For a negative uniaxial crystal and type I phase-matching, this angle is given by

$$\tan \rho = \frac{(\eta_0^{\omega})^2}{2} \left[\frac{1}{(\eta_e^{2\omega})^2} - \frac{1}{(\eta_0^{2\omega})^2} \right] \sin 2\theta_m . \qquad (6.17)$$

The beams separate or walk off in a distance of the order

$$\ell_a \simeq \frac{a}{\rho}, \qquad (6.18)$$

where a is the beam diameter and ℓ_a is called the aperture length. Although this effect can be minimized by using a large beam diameter, the conversion efficiency, which decreases with beam diameter, may be lowered as a result.

Another problem comes from the divergence of the interacting beam. For second-harmonic generation in a negative uniaxial crystal, the phase-matching condition ($\Delta k = 0$) is satisfied only at exactly $\theta = \theta_m$; a small deviation ($\delta\theta$) from this angle would yield a phase mismatch Δk in the order of $\delta\theta \sin 2\theta_m$. Hence a limit is imposed on the allowed divergence of the interacting beam. The angular deviation $\delta\theta$ from the phase-matching direction such that the conversion efficiency drops to half of its peak value is given by

$$\delta\theta = \frac{0.44\ \lambda^{\omega} \eta_0^{\omega} / L}{(\eta_0^{2\omega} - \eta_e^{2\omega}) \sin 2\theta_m} , \qquad (6.19)$$

where η_0^{ω}, $\eta_0^{2\omega}$ and $\eta_e^{2\omega}$ are the refractive indices of the ordinary wave at the fundamental frequency, the ordinary wave at the second-harmonic frequency and the extraordinary wave at the second-harmonic frequency, respectively. The length of the nonlinear crystal is L. This expression gives an estimate of the acceptable divergence angle of the fundamental laser beam.

Since the refractive indices of the crystal are temperature dependent, a variation in the temperature would affect the phase-matching condition. The temperature deviation from the phase-matched temperature such that the conversion efficiency drops to half of its peak value is given by

$$\Delta T = \frac{0.44\ \lambda^{\omega}}{L \frac{d}{dT} (\eta_e^{2\omega} - \eta_0^{\omega})} . \qquad (6.20)$$

Ambient temperature variation or absorption losses in the crystal are possible sources that give rise to temperature change.

Other practical considerations include the optical homogeneity and the damage threshold of the crystal as well as the nonlinear coefficient of the crystal.

6.3.2 Generation of ultrashort UV pulses with ADP crystals

Single DFDL pulses with power of 3 MW were easily obtained with the two-stage dye amplifiers described in Chapter 5. These pulses are powerful enough to produce ultrashort UV pulses through the nonlinear process of second-harmonic generation.

The nonlinear crystal used in the experiment was an ADP (ammonium dihydrogen phosphate) crystal. It is a negative uniaxial crystal belonging to point group $\bar{4}$ 2 m and has a tetragonal symmetry. It is transparent at wavelengths ranging from 0.22 μm to 1.6 μm. It is hygroscopic; the polished faces may be fogged if exposed to a humid atmosphere. Crystals of ADP are available in large sizes and they are of excellent optical quality. They also have large laser damage thresholds.

The importance of phase-matching was discussed earlier on. Efficient second-harmonic generation can be achieved only if the laser beam is launched in a phase-matched direction. There are also restrictions imposed on the azimuthal angle. In practice, all these are pre-arranged by cutting the crystal at an appropriate plane so that the laser beam with the correct polarization is launched normal to that plane. The crystal used in our experiment was originally cut for a wavelength at 600 nm with a phase-matching angle of 61.7° at 25°C. The phase-matching angle for a laser beam at 616 nm is 59.3° at 25°C. The DFDL beam therefore had to be launched at an angle of about 3.6° from the normal of the crystal. The crystal was fixed in a gimbal mount so that it could be finely adjusted to meet the phase-matching requirement. The azimuthal angle had already been cut at 45°. The orientation of the crystal was arranged so that a horizontally polarized DFDL beam entered the crystal as an ordinary wave. The second-harmonic output would accordingly be vertically polarized.

Equation (6.12) indicates that the conversion efficiency is

proportional to the power density of the fundamental. Hence, the amount of second-harmonic power may be greatly enhanced by focusing the fundamental beam into the nonlinear crystal. There are, however, some important factors which may limit the effectiveness of intense focusing. First of all, a tightly focused beam may have a very large divergence angle. However, the divergence angle is limited to a value given by equation (6.19) if the phase-matching condition is not to be seriously violated. If the extent of the focal region is approximately equal to the length of the crystal, undesirable effects due to beam divergence would be minimized if the crystal were placed at the centre of the focal region. For a Gaussian beam, the focal region has a length given by the confocal parameter b, where

$$b = \frac{2\pi w_0^2 \eta}{\lambda} \qquad (6.21)$$

(see section 5.3.2). Within this focal region, the beam has approximately a plane wave-front. An exact analysis [32] shows that optimum focusing occurs at L = 2.84b. The length of our nonlinear crystal is 17 mm. If the above focusing condition is applied, a beam diameter of 39 μm would be obtained in the focal spot. This, however, implies the power density would have been 250 GW/cm^2, which is well above the damage threshold of the crystal.

Another problem would arise with such a small beam diameter. As mentioned earlier, the walk-off effect will limit the effective crystal volume over which harmonic generation can take place. Using equations (6.17) and (6.18), we can calculate the aperture length corresponding to a beam diameter of 39 μm. A value of 1.4 mm is obtained; this is much smaller than the length of the crystal (17 mm).

It was decided that the focusing of the fundamental beam into the nonlinear crystal should not produce an aperture length much shorter than the length of the crystal. This meant that the beam diameter at the crystal should not be much smaller than 480 μm. Experimentally, a beam diameter of about 450 μm (Gaussian beam assumed) was found to produce reasonably high conversion efficiency. The second-harmonic power obtained with other focusing conditions was lower.

A power density of ~ 2 GW/cm^2 ($2w_0$ = 450 μm) did not seem to cause any optical damage to the crystal. No oven was available to

keep the temperature of the crystal constant. However, when a repetition rate of about 1 Hz had been used for more than a few minutes, the system seemed to have reached a stable condition so that the phase-matching angle did not vary from shot to shot. A quartz prism was placed near the exit end of the crystal to separate the second-harmonic beam from the fundamental beam by dispersion. The second-harmonic beam could then be monitored with a UV photodiode. Its energy was measured with a joulemeter (GEN-TEC ED-100A). When the energy of the input fundamental beam was 265 μJ, the energy of the second-harmonic beam was measured to be about 53 μJ. The conversion efficiency was 20%. This value is substantially lower than would have been expected from a crystal with a length of 17 mm under perfect phase-matched conditions. But, as discussed before, the walk-off effect would reduce the effective volume of nonlinear interaction. This seems to be the main cause of the reduction in conversion efficiency.

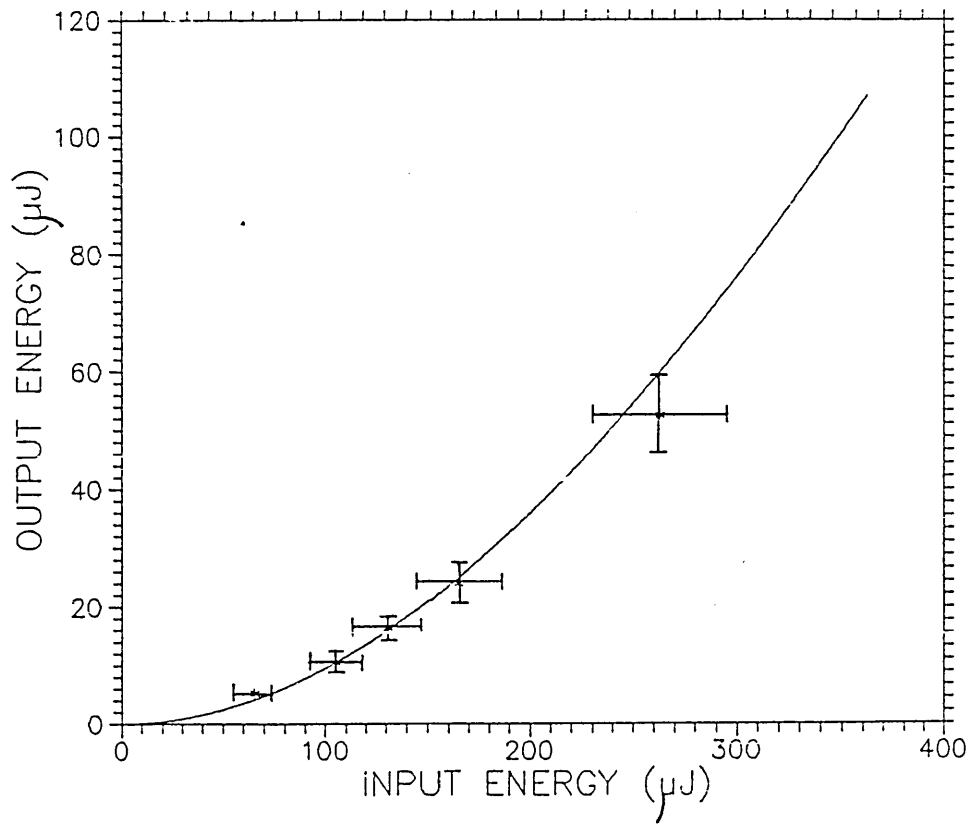
Although the exact pulse duration and pulse shape were not measured since no suitable streak camera was available, the signals recorded on the oscilloscope showed that the second-harmonic pulse duration was lower than the resolution limit of the oscilloscope (i.e. less than 1 ns). The amplified DFDL pulse at the fundamental frequency was monitored with a streak camera and found to have a Gaussian-like profile of duration about 100 ps; the second-harmonic pulse would be expected to have similar temporal characteristics.

The second-harmonic beam had quite good beam quality. It was rectangular in shape with soft edges and the beam intensity was fairly uniform over the whole region; no "hot-spot" was found. The beam quality at the far field was also found to be very good. At a distance of 11 metres from the nonlinear crystal, the intensity over the beam area of 6 mm (vertical) by 15 mm (horizontal) was found to be still fairly uniform.

Equation (6.12) gives the dependence of the second-harmonic power on the power of the fundamental. However, the quadratic dependency will not be satisfied at high conversion efficiency when the power lost by the input fundamental is not negligible. The correct dependency takes the form of

$$P^{2\omega} = P^{\omega} \tanh^2(k\sqrt{P^{\omega}}), \qquad (6.22)$$

Figure 6.5. Dependence of second-harmonic energy on fundamental energy.



where k is a constant, which depends on laser beam and crystal parameters. The dependency of second-harmonic energy on the fundamental energy has exactly the same form. The magnitude and unit of constant k are, of course, different.

The dependency of second-harmonic power on the fundamental power was investigated experimentally. Using different calibrated neutral density filters, the input energy of the fundamental beam could be varied. The corresponding output energy was measured with the joulemeter. Figure 6.5 shows the results of the investigation. A computer program was written to generate a curve described by equation (6.22). The value of k was varied to produce a fitted curve for the experimental data. This curve was found to be a better fit than a simple parabola, confirming that the pump-depletion (i.e. the depletion of the fundamental beam energy) cannot be totally ignored.

6.4 Conclusion

We have described an oscillator-amplifier system for the generation of ultrashort UV pulses. With the DFDL oscillator operating at 616 nm, a two-stage amplifier system was constructed to produce intense ultrashort single pulses with peak power up to 4 MW. Special care was taken to suppress the ASE of the high gain system. A prism amplifier cell (invented by Bethune) was used in the second stage amplifier in order to obtain good beam quality in the final laser beam. The amplifier saturation characteristics were also investigated. Ultrashort UV pulses were generated with an ADP crystal through the nonlinear process of second-harmonic generation. Special attention was paid to the phase-matching requirements so that a high conversion efficiency could be obtained. It was necessary to focus the laser beam into the crystal to yield a high fundamental beam intensity, with which the conversion efficiency varied almost linearly. However, for the crystal used in our experiment, the beam walk-off effect put a limit on the degree of focusing, hence the conversion efficiency.

CHAPTER 7

CONCLUSION

Distributed feedback structures have been used to generate coherent radiation in a wide variety of laser systems. The general theory of both gain-coupled and index-coupled distributed feedback lasers has been described. The major differences between these two types of DFB lasers have also been discussed.

The generation of ultrashort pulses with the gain-coupled distributed feedback dye lasers has been studied experimentally and theoretically. The rate equation model used by Bor to describe the laser output characteristics of the DFDL has been outlined and used to obtain computer simulations. This model is based on the photon-rate equations which describe the interaction between the population inversion and the number of photons inside the laser cavity. The key parameter in this model is the equivalent cavity decay time. However, as we have pointed out, the use of this particular parameter is by no means unquestionable. A modified version of this model has been proposed as another way of analysing the pulse-forming mechanism of the DFDL. In this simplified model, the self Q-switching effect is ignored by using an appropriate constant cavity decay time. The pulse-forming mechanism is viewed in terms of relaxation oscillation. Comparisons between the results of this new model and other existing models consistently indicate that the self Q-switching effect produces a further reduction on the pulse duration of DFDL pulses by approximately 40%. Some simple analytic relationships have also been derived with the new set of rate equations. They have been found to be consistent with the computer-generated results. Moreover, these relationships have been found to apply equally well to the original sets of rate equations used by Bor. This further supports the approach of treating the self Q-switching effect as a second-order effect. Some of the analytic expressions were compared with experimental results; good agreement has been found.

Experimental studies of an excimer laser (XeCl) pumped distributed feedback dye laser have been described in detail. It was discovered that various properties of the UV pump beam could

influence the DFDL output. Simultaneous measurements of the temporal and spectral characteristics of the DFDL pulses showed that the single DFDL pulses were effectively transform-limited. The DFDL beam was also found to have excellent transverse beam quality. The propagation of the laser beam was successfully analysed with the theory of the fundamental Gaussian beam. The DFDL beam was found to be nearly diffraction-limited.

A master oscillator-amplifier system based on the XeCl pumped DFDL has been described. Intense ultrashort single pulses with power up to 4 MW have been produced. Second-harmonic generation in an ADP crystal was used to frequency-double the visible laser pulse to produce ultrashort UV pulses at 308 nm. Single UV pulses with energy more than 50 μJ were recorded. This corresponds to a peak power of around 0.5 MW.

Further development of the laser system described above is currently under way at Imperial College [33]. For example, the UV pulse can be used to injection-lock an XeCl amplifier to generate very intense UV radiation. Simple multi-passes amplification may also be used to produce intense pulses in a XeCl module. Through the process of laser plasma interaction, these intense radiations can be used to generate soft X-rays, which find applications in X-ray lithography.

It has been demonstrated that the XeCl pumped DFDL system is a simple and reliable system for the generation of intense ultrashort pulses.

REFERENCES

1. H. Kogelnik, C.V. Shank
   Journal of App. Phys. 43, 2327 (1972).
2. H. Kogelnik, C.V. Shank
   Appl. Phys. Letts. 18, 152 (1971).
3. C.V. Shank, J.E. Bjorkholm, H. Kogelnik
   Appl. Phys. Letts. 18, 395 (1971).
4. M. Nakamura, A. Yariv, H.W. Yen, S. Somekh
   Appl. Phys. Letts. 22, 515 (1973).
5. A.A. Zlenko, A.M. Prokhorov, V.A. Sychugov
   Sov. J. Quant. Electron. 3, 493 (1974).
6. D.P. Schinke, R.G. Smith, E.G. Spencer, M.F. Galvin
   Appl. Phys. Letts. 21, 494 (1972).
7. C.V. Shank, R.V. Schmidt, B.I. Miller
   Appl. Phys. Letts. 25, 200 (1974).
8. G.C. Bjorkland, L.F. Mollenauer, W.J. Tomlinson
   Appl. Phys. Letts. 29, 116 (1976).
9. E. Affolter, F.K. Kneubühl
   Phys. Letts. A74, 407 (1979).
10. Z. Bor
    IEEE J. Quantum Electronics, QE-16, 517 (1980).
11. Z. Bor, A. Müller, B. Racz, F.P. Schäfer
    Appl. Phys. B27, 9 (1982).
12. C. Lin
    IEEE J. Quantum Electronics QE-11, 602 (1975).
13. S.R. Chinn
    Opt. Commun. 19, 208 (1976).
14. Z. Bor, F.P. Schäfer
    Appl. Phys. B31, 209 (1983).
15. H.A. Haus
    Appl. Opt. 14, 2650 (1975).
16. I.N. Duling III, M.G. Raymer
    IEEE J. Quantum Electronics QE-20, 1202 (1984).
17. Z. Bor
    Opt. Commun. 29, 103 (1979).

18. Z. Bor, B. Racz, G. Szabo
Picosecond Phenomena II - K.B. Eisenthal (editor)
Springer, Heidelberg, Berlin, New York, 1982, pp. 62-65.
19. G. Szabo, Z. Bor
Appl. Phys. B 31, 1 (1983).
20. G. Szabo, B. Racz, A. Müller, B. Nikolaus, Z. Bor
Appl. Phys. B 34, 145 (1984).
21. S. Szatmari, B. Racz
Appl. Phys. B 43, 93 (1987).
22. Z. Bor, B. Racz, G. Szabo
Helvetica Physica Acta 56, 383 (1983).
23. S. Szatmari, F.P. Schäfer
Appl. Phys. B 33, 95 (1984).
24. H. Telle, W. Huffer
Opt. Commun. 38, 402 (1981).
25. Z. Bor
Opt. Commun. 39, 383 (1981).
26. M.E. Lusty, M.H. Dunn
Appl. Phys. B 44, 193 (1987).
27. Timmerman's Physico-Chemical Constants of Pure Organic Compounds.
Elsevier 1950.
28. I.A. McIntyre, M.H. Dunn
Opt. Commun. 50, 169 (1984).
29. D.S. Bethune
Appl. Opt. 20, 1897 (1981).
30. L.M. Frantz, J.S. Nodvik
Journal of Appl. Phys. 34, 2346 (1963).
31. A. Yariv
Quantum Electronics - John Wiley & Sons, Inc. 1975.
32. G.D. Boyd, D.A. Kleinman
Journal of Appl. Phys. 39, 3597 (1968).
33. D. Xenakis
Private communication.